

# Validation of Sequentially Linear Analysis by simulating structural behaviour of masonry components



# Validation of Sequentially Linear Analysis by simulating structural behaviour of masonry components

by

CYNTHIA SIMONE MEIRING

For the degree of Master of Science in Structural Engineering  
at Delft University of Technology

To be defended in public on June 22nd, 2018

Student number: 4090373  
Thesis committee: Dr. Ir. M.A.N. Hendriks, Structural Mechanics  
Prof. Dr. Ir. J.G. Rots, Structural Mechanics  
Ir. M. Pari, Structural Mechanics  
Dr. Ir. G.J.P. Ravenshorst, Timber & Timber Structures

Faculty of Civil Engineering and Geosciences • Delft University of Technology



# Preface

This thesis report is written to conclude the Master Structural Engineering at the Faculty of Civil Engineering and Geosciences at the Delft University of Technology. It involved numerical modelling of masonry using Sequentially Linear Analysis as an alternative for regular Non-linear Finite Element Analysis to improve the numerical robustness of the Finite Element Method.

I am grateful that I got the opportunity to work on this topic and to help testing the SLA implementation in the DIANA software. It was an interesting but complex task and I encountered quite some challenges during this thesis, especially due to the fact that the SLA implementation had to undergo several adjustments this year. I would like to thank Manimaran for all his patience and help regarding the SLA code. His help made it possible to continue my work in a consistent way. Furthermore, I would like to thank the other committee members; Geert, Jan and Max for their guidance to keep me on the right track.

Finally, I would like to address a few words to my family, friends and to Ashwin: thank you for your help, love and the confidence you gave me to finish my thesis. It is great to feel so supported, especially during the last stage of the Master.

Cynthia Meiring  
Delft, June 2018



# Summary

The unreinforced masonry construction of Dutch terraced houses in Groningen is prone to lateral earthquake loading. To analyse the capacity of these houses, the faculty of Civil Engineering at the TU Delft started a test campaign, whereby experiments are performed on complete structures, in-plane loaded shear walls and out-of-plane loaded transversal walls. In this thesis, the experimental results served as benchmarks to validate a relatively new numerical method: Sequentially Linear Analysis (SLA). This method is developed to overcome numerical instability, which is a problem for regular non-linear finite element analyses (NLFEA). The method performs linear analyses with a scaled variable load, after which a damage increment is assigned to one integration point in the computational model. The objective of this thesis is to investigate to what extent SLA is able to predict the behaviour of the two main components of a Dutch house, namely the shear wall and the out-of-plane loaded transversal wall, during a monotonic pushover test.

For both components, two modelling approaches were applied: the smeared crack approach, where the wall is composed of one material only, and the discrete crack approach, where a distinction is made between the mortar joints and brick units. Within each approach, two finite element types were used. The new implementation of the SLA code for shell elements is validated by modelling the shear wall with plane stress elements as well. However, the most important comparison, was the one between NLFEA and SLA in order to see how SLA can improve numerical predictions of brittle behaviour of masonry components. The recently developed SLA code for non-proportional loading is used to be able to model pre-stressed walls. The algorithm for non-proportional loading is more complex than the algorithm for proportional loading, as a distinction has to be made between the initial pre-stress load and the variable load, where only the variable load has to be scaled in every analysis step, according to the SLA procedure. A similar well-known NLFEA procedure (the phased analysis) is used to verify the non-proportional loading algorithm.

Results showed that the non-proportional SLA algorithm still contains certain flaws and after analysing the test models, it is found that in case of tensile failure the code might pick one integration point as the critical one an infinite number of times. This hinders the failure process of the numerical model as no damage increment can be applied to other integration points any more. Another shortcoming occurred when the shear wall was modelled using shell elements: negative displacements were observed even though the wall was loaded in positive direction. Stop criteria were defined to temporarily deal with these problems.

The results also showed remaining shear stresses at the bottom of the shear wall in case of a NLFEA when a  $\beta$ -factor of 1% was applied. These remaining shear stresses caused an over-prediction of the force capacity. This "shear locking" problem didn't occur in case of a SLA. The  $\beta$ -factor of SLA drops at the last moment till approximately zero and for that reason, SLA is able to accurately predict the peak load. Furthermore, we found a significant increase in calculation time in two cases, while performing a SLA. First, as soon as the plane stress elements in the shear wall were replaced by shell element. Shell elements have more integration points in thickness direction and therefore more integration points will be damaged. The calculation time increased by a factor of maximum 19, even though the number of integration points in thickness direction was only increased from 1 (for the plane stress elements) to 3 (for the shell elements). Second, the calculation time significantly increased when the out-of-plane loaded wall was modelled using a smeared crack approach. In contrary to the discrete crack approach where the damage was lumped in the interface elements, the damage was scattered

over the wall, meaning that more analysis steps were required to damage the wall. The calculation time increased by a factor of 3.

The last main observation is that SLA is not able to simulate the rocking behaviour of both components yet, due to the lack of geometrical non-linearity. The analytical calculations showed that the decrease of base shear force capacity is most severe for the out-of-plane loaded transversal wall. For that reason the limitation of not including geometrical non-linearity effected that masonry component the most and the post-peak behaviour couldn't be simulated.

From these results, it can be concluded that SLA is able to predict the behaviour of pre-stressed masonry components using the non-proportional loading algorithm, except for the post-peak behaviour of the out-of-plane loaded transversal wall. SLA outperforms NLFEA in the sense that it is inherently stable and no over-stiff response is observed, while modelling the shear wall with a constant shear retention factor. This way, SLA is able to give a more accurate prediction of the peak load of the shear wall. Besides that, the type of element and the type of modelling approach have a significant influence on the calculation time and therefore on the costs. Furthermore, as SLA is under development, the method still has some difficulties to overcome. The stop criteria were helpful to deal with the identified problems, but further research needs to be done to actually solve the problems.

# Acronyms

CaSi	Calcium Silicate
COMP	Component
DIANA	Displacement Analyser
FR	Force-Release
LU	Load-Unload
NAM	Nederlandse Aardolie Maatschappij
NLFEA	Non-linear Finite Element Analysis
NPR	Nederlandse Praktijk Richtlijn
NR	Newton Raphson
SLA	Sequentially Linear Analysis
TUD	Technische Universiteit Delft
URM	Unreinforced Masonry



# List of symbols

$\beta$	Shear retention factor
$d_k$	Damage parameter
$\varepsilon$	Strain
$\varepsilon_{ult}$	Ultimate strain
E	Young's modulus
F	Force
$f_c$	Compressive strength
$f_t$	Tensile strength
g	Out-of-balance force
$G_{f,c}$	Fracture energy in compression
$G_{f,t}$	Fracture energy in tension
G	Shear modulus
K	Stiffness
$k_n$	Normal stiffness of interface element
$k_t$	Shear stiffness of interface element
$\lambda_{crit}$	Critical load multiplier
$\lambda_{ini}$	Initial load multiplier
$\nu$	Poisson's ratio
$n_c$	Number of sawteeth in compression
$n_t$	Number of sawteeth in tension
$p_{fac}$	Ripple band width parameter
$\rho$	Material density
$\sigma$	Stress
u	Displacement



# Contents

<b>Preface</b>	<b>ii</b>
<b>Summary</b>	<b>iii</b>
<b>Acronyms</b>	<b>vii</b>
<b>List of symbols</b>	<b>ix</b>
<b>1 Introduction</b>	<b>1</b>
1.1 Background and motivation . . . . .	1
1.2 Research question and scope . . . . .	2
1.3 Methodology and outline . . . . .	3
<b>I Literature study and analytical calculations</b>	<b>5</b>
<b>2 Background theory</b>	<b>7</b>
2.1 Masonry behaviour . . . . .	7
2.2 Finite element modelling . . . . .	12
2.3 Non-linear analysis . . . . .	16
2.4 Sequentially Linear Analysis . . . . .	20
<b>3 Experimental results</b>	<b>27</b>
3.1 Experiment TUD_COMP-24 . . . . .	27
3.2 Experiment TUD_COMP-28 . . . . .	30
<b>4 Analytical calculations</b>	<b>33</b>
4.1 In-plane loaded shear wall . . . . .	33
4.2 Out-of-plane wall . . . . .	38
<b>II Numerical modelling</b>	<b>41</b>
<b>5 Shear wall: smeared crack approach</b>	<b>43</b>
5.1 Finite element model . . . . .	43
5.2 Overview numerical models . . . . .	46
5.3 Plane stress elements . . . . .	47
5.4 Shell elements . . . . .	59
5.5 Conclusions . . . . .	62

<b>6 Shear wall: discrete crack approach</b>	<b>63</b>
6.1 Finite element model . . . . .	63
6.2 Plane stress elements . . . . .	66
6.3 Shell elements . . . . .	71
6.4 Conclusions . . . . .	73
<b>7 Out-of-plane wall: smeared crack approach</b>	<b>75</b>
7.1 Finite element model . . . . .	75
7.2 Shell elements . . . . .	78
7.3 Conclusions . . . . .	81
<b>8 Out-of-plane wall: discrete crack approach</b>	<b>83</b>
8.1 Finite element model . . . . .	83
8.2 Shell elements . . . . .	85
8.3 Conclusions . . . . .	87
<b>9 Discussion and conclusions</b>	<b>89</b>
<b>10 Recommendations</b>	<b>93</b>
<b>Bibliography</b>	<b>96</b>
<b>Appendices</b>	<b>97</b>
A Shell elements fixed in out-of-plane direction . . . . .	97



Therefore Rots (2001) proposed a relatively new numerical method to simulate non-linear structural behaviour, which is called Sequentially Linear Analysis (SLA). This method performs, instead of an iterative non-linear analysis, sequentially linear analyses, which are inherently stable. However, this method is still under development and a lot of limitations have to be overcome. One major difficulty is to apply the load non-proportionally, meaning that there is a combination of an initial load, such as self weight, and a lateral load. As SLA is currently getting implemented and tested in the DIANA software, there is a need to validate the current SLA code and to get insight into how SLA can improve numerical predictions of unreinforced masonry structures.

## 1.2 Research question and scope

The objective of this thesis is to investigate if the SLA method works sufficiently to model the two main components of the structure, namely the in-plane loaded shear wall and the out-of-plane loaded transversal wall, individually. This could support future research into modelling the complete structure using SLA. Regular non-linear finite element analyses (NLFEA) will be conducted and will serve, besides the experimental results and analytical calculations, as a validation of the SLA method (see figure 1.2). The research question will be as follows:

*To what extent is the Sequentially Linear Analysis method able to predict the structural behaviour of two unreinforced masonry components of the TUD-2 Building, namely the in-plane loaded shear wall and the out-of-plane loaded transversal wall, during a monotonic pushover test?*

To answer this question, first the following sub-questions will be answered by means of a literature study:

1. What types of non-linearity do exist and what are the limitations of current numerical methods for a non-linear finite element analysis (NLFEA)?
2. What is SLA and how does the procedure work?
3. What are the properties and failure mechanisms of masonry?
4. How can masonry be modelled?

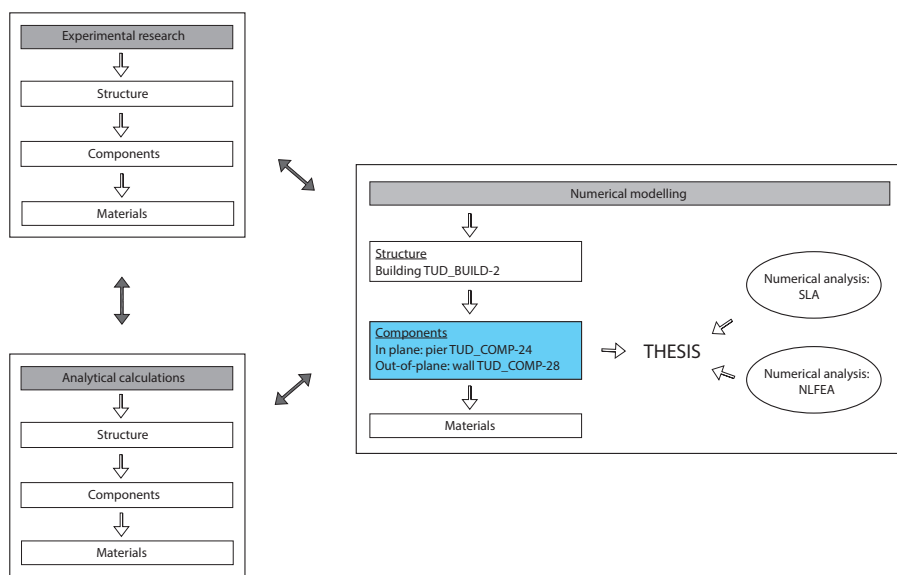


**Figure 1.2:** Scope of research.

Other sub-questions will be answered in the research part of the thesis and are as follows:

5. How do the results of the numerical models differ from the experimental results and the analytical calculations?
6. What are the differences using the smeared crack model and the discrete crack model, with respect to the crack pattern and the capacity curve?
7. How do the results from the NLFEA differ from SLA, with respect to the crack pattern and the capacity curve?
8. Is the outcome from the model with shell elements similar to the model with plane stress elements, with respect to the crack pattern and the capacity curve?

To answer the sub-questions and subsequently the main research question, it is necessary to have a clear scope of the research at forehand. For that reason the following restrictions are defined:

- The thesis will elaborate on the components composed of large CASIEL-elements, as the TUD-2 Building is made of these elements as well.
- The in-plane loaded component with clamped-clamped boundary conditions is taken into account. The corresponding experiment code is: *TUD\_COMP – 24*.
- The out-of-plane loaded component with clamped-clamped boundary conditions is taken into account. The corresponding experiment code is: *TUD\_COMP – 28*.
- The numerical models are exposed to non-proportional loading, meaning that there is an initial load such as self weight and a variable load.
- The variable load is a static/monotonic pushover load, instead of a quasi-static cyclic pushover load, for sake of simplification and because no crack-closure algorithm for SLA is available yet, which could give problems in case of load reversal.
- The type of material model/crack model being used, is limited to the 'total strain based crack model', since SLA is currently only available for this type.

### 1.3 Methodology and outline

This report is mainly divided into two parts. One part elaborates on numerical modelling of the in-plane load case and the other part is about modelling the out-of-plane load case. During the research, three comparisons are made:

- Smeared crack approach versus discrete crack approach
- Plane stress elements versus shell elements
- NLFEA versus SLA

The main task is to compare regular non-linear finite element analysis (NLFEA) with Sequentially Linear Analysis (SLA) in order to get a better understanding of the opportunities and challenges or disadvantages of SLA as an alternative for non-linear analyses. To do so, two modelling approaches are used: the smeared crack approach and the discrete crack approach. These approaches determine how the numerical model is built: the discrete crack approach includes interface elements between the continuum elements, whereas the smeared crack approach only includes continuum elements. Within each approach, a type of finite element has to be chosen. A 3D structure would be modelled using shell elements, which do allow for both in-plane and out-of-plane behaviour. The individual components are therefore modelled with shell elements as well. However, in case of an in-plane loading configuration, plane stress elements would be sufficient. For that reason, these elements are used to verify the (new) implementation of SLA for shell elements. The comparison between plane stress elements and shell

elements only holds for the in-plane loaded shear wall. The out-of-plane loaded transversal wall cannot be modelled with plane stress elements, as these elements don't allow out-of-plane deformations and they assume zero stresses perpendicular to the plane. See figure 1.3 for an overview of the methodology.

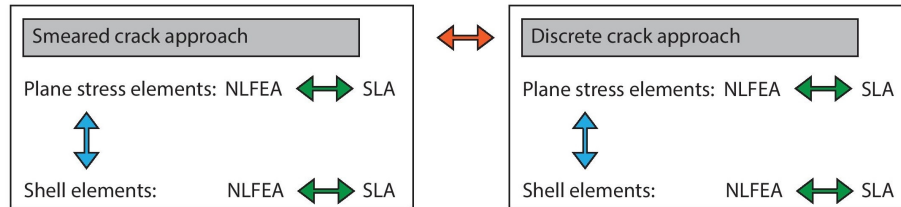


**Figure 1.3:** Overview methodology.

The outline of this thesis is as follows. Chapter 2 provides the reader with background information about finite elements modelling, masonry behaviour and the Sequentially Linear Analysis. Chapter 3 describes the experiments, performed in 2016 and 2017 at the faculty of Civil Engineering, where after the analytical calculations of the components are presented in chapter 4. The numerical predictions are discussed in chapter 5 till chapter 8. The first two elaborate on the in-plane shear wall and the last two on the transversal wall. The report ends with conclusions and recommendations in chapter 9 and 10 respectively.

## Part I

# Literature study and analytical calculations



## 2. Background theory

In order to understand the behaviour of masonry and to get insight into numerical modelling strategies to model masonry structures some background information is required. This chapter consists of four sections. The first one elaborates on the behaviour of masonry, among other things its failure mechanisms and material properties. The second section gives a short explanation of the finite element method, which is a numerical tool to evaluate (parts of) a structure. Furthermore it explains some modelling strategies and highlights the finite elements, used in this report. Besides modelling options also a choice has to be made between different types of analyses. In section three the non-linear analysis and its limitations are discussed. The chapter ends with a section about a relatively new type of analysis as an alternative to the non-linear analysis: the Sequentially Linear Analysis.

### 2.1 Masonry behaviour

#### 2.1.1 Traditional Dutch building method

Building with masonry has a long history in the Netherlands and nowadays this material is still often being used. This is mainly due to its aesthetic appearance, low costs, durability and the simplicity of its stacking technique (Rots and Civieltechnisch Centrum Uitvoering Research en Regelgeving (Netherlands), 1997).

The Dutch masonry houses are built between 1960 and 1980 and possess some important similarities which are typical for these types of buildings. A row of terraced houses consists mainly of 5-10 units built side by side, where every unit is a two-story high masonry building, with an inter-story height of 2.5 - 2.7 meter. The floor plan has typically a width of 5 meters and a depth of 7-9 meters. Another important aspect of these terraced houses is the presence of large daylight openings. The construction is therefore composed of two slender piers in the façades and two long transversal cavity walls. The stiff floors are mainly made of concrete, which could be prefabricated or cast in-situ, and are carried by the transversal walls (Esposito et al., 2017).

The cavity walls consist of an internal and an external leaf, both made out of masonry. Since the 1970's a new way of building load bearing walls came up, namely building with calcium-silicate



Figure 2.1: Typical Dutch terraced houses.

elements (also known as 'CASIELS' or 'CaSi-elements'). Whereas the traditional baked clay bricks are used in the external leaf due to their aesthetic appearance, the calcium silicate walls (internal leaf) have a load bearing function. The need to speed up the construction phase, have led to an increase in the elements size of these CaSi-elements. The elements are now roughly  $900 \times 650 \times 100 \text{ mm}^3$  (Pari et al., 2017). Unlike the traditional baked clay bricks, the calcium silicate elements have to be placed on top of each other using a small crane and the units are connected by a tongue-groove joint. To ensure adhesion and to deal with dimension tolerances a thin-layer mortar of 2-3 mm is applied between the elements (Ng'andu, 2006).

### 2.1.2 Research into masonry

Even though building with masonry is very popular, the development of this material is way behind compared to steel and concrete, due to the lack of insight into its complex behaviour. Masonry is a stone-like material and the properties strongly depend on the mixture. Furthermore, the structural behaviour depends on the stacking technique and the skills of the construction worker. Especially knowledge about the typically Dutch building method, which differs from building practice in surrounding countries by its slender cavity walls, was lacking. That's why a research program 'Structural Masonry I' had started, initiated by the Netherlands unit and calcium-silicate industries. This has led to a basis for practical design rules (Rots and Civieltechnisch Centrum Uitvoering Research en Regelgeving (Netherlands), 1997).



**Figure 2.2:** (a) Load bearing structure of Dutch terraced houses (Esposito et al., 2016) (b) Set-up experiment BUILD\_TUD-2 in Stevin lab 2 at TU Delft (Schippers, 2017).

Another reason to study the behaviour of masonry even more is related to the earthquakes in Groningen. Unreinforced masonry buildings are very well able to resist gravity loads, but during an earthquake they perform weak compared to concrete, wood and steel, because they are not able to carry the loads in lateral direction due to the low tensile strength. During lateral loading the structure has a weak and a strong direction. When the structure is loaded in the strong direction, the piers are loaded out-of-plane and the transversal wall in-plane. For the weak direction is the other way around where the transversal walls are loaded out-of-plane and the piers act as shear walls. The width of the piers is smaller than the width of the walls, thus in case of lateral loading during an earthquake, there is less material to transfer the horizontal forces to the ground and the latter case is therefore called 'the weak direction' of the structure.

The TU Delft started a test campaign in 2016 carried out for the NAM to study the load bearing capacity of this type of houses in the weak direction. In the test campaign also the individual components, namely the wide piers, loaded in shear, and the out-of-plane walls are tested individually to get a better understanding of the whole structure. A lot of research is still going on to be able to assess the risk of building damage and to make reliable numerical predictions of the response of the building under lateral loading.

### 2.1.3 Material properties

As mentioned before, the bricks and mortar are stone-like materials. When loaded in tension, they behave as brittle materials (like concrete) with an exponential softening curve (figure 2.3a). The material follows a linear elastic path until the stress reaches the tensile strength  $f_t$ , then the material starts to crack. Loading the material even further, will result in softening behaviour, meaning a gradual decrease of the mechanical strength under a continuous increase of deformation (Angelillo, 2014).

In case of compression the material shows hardening behaviour after some initial crushing. Loading the material beyond the compressive strength leads to a parabolic softening relation.

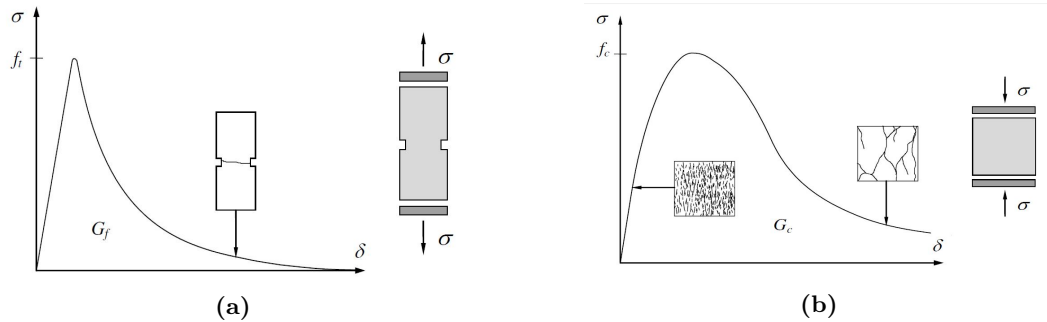


**Figure 2.3:** Mechanical behaviour of masonry: (a) Tensile curve (b) Compression curve (Angelillo, 2014).

### 2.1.4 Failure mechanisms

To understand the structural response of masonry buildings during earthquakes or to be able to interpret results from numerical simulations better, it is useful to get more insight into the possible failure mechanisms. In this section a distinction is made between local and global failure modes. Local failure mechanisms refer to failure at element level, whereas global failure implies failure of the total structure. The type of global failure depends among other things on the loading pattern, geometry, materials and how the structure is built. Bruneau (1994), ElGawady et al. (2007) and Lourenço (1996) elaborate on different failure modes and a short summary of these mechanisms is presented in this subsection.

#### Local failure mechanisms

Masonry has an orthotropic geometry, it namely consist of units (bricks) and joints (mortar), where the horizontal joints are called the bed joints and the vertical joints the head joints. The brick-mortar-interface is typically the weakest link (Van Dam, 2015).

Lourenço (1996) presents different failure mechanisms at element level (figure 2.4). The first two mechanisms involve only the joint: in figure (a) the brick-mortar interface fails in tension, whereas

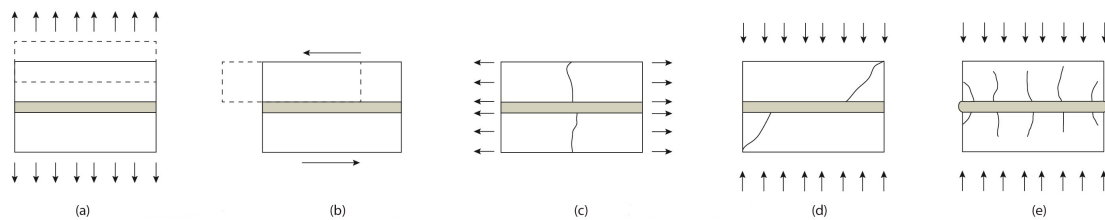


**Figure 2.4:** Local failure mechanisms (a) Joint tension crack (b) Joint slip (c) Unit direction tension crack (d) Unit diagonal tension crack (e) Masonry crushing (Lourenço, 1996).

in figure (b) the material fails due to sliding over the interface. The third mechanism occurs due to failure (cracking) in the bricks only. The last two mechanisms are combined failure modes involving both the joint and the unit.

### Global failure mechanisms: in-plane

In figure 2.5 the failure modes for in-plane behaviour are illustrated. The first picture refers to shear failure, where a diagonal crack develops in the wall. If the bricks have a high stiffness and the mortar is rather weak, the crack pattern will follow the path of the head and bed joints. For relatively weak bricks and strong mortar, the cracks may also go through the bricks.

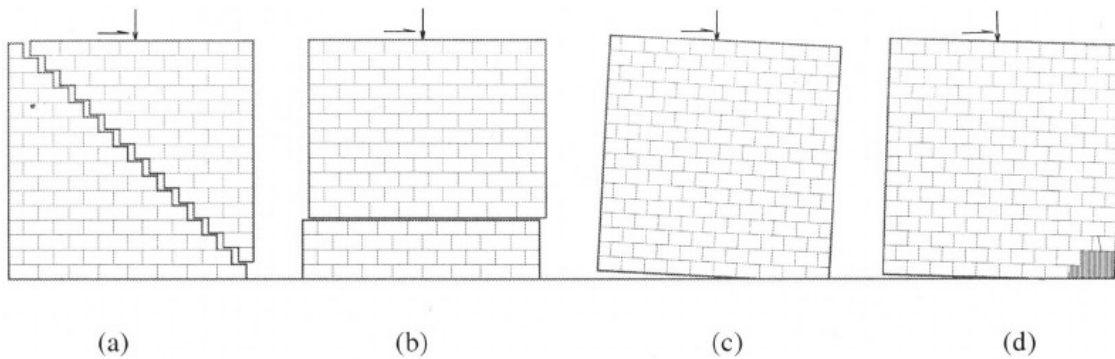


**Figure 2.5:** In-plane failure mechanisms: (a) Shear failure (b) Sliding failure (c) Rocking failure (d) Premature toe crushing (ElGawady et al., 2007).

The second picture illustrates sliding failure. The upper part of the wall slides over the bottom part, which especially occurs when the vertical loads and/or the friction coefficient are low due to poor quality mortar. Flexural failure (rocking failure) and toe-crushing are the last two in-plane failure modes. These modes especially appear when the shear resistance is relatively high. It leads to excessive rotation (rocking) of the complete wall.

### Global failure mechanisms: out-of-plane

#### LACK OF ANCHORAGE

This type of failure is related to the connection of a floor/roof to the unreinforced masonry walls. A floor can be supported by the load bearing walls in different ways. One way is to clamp the floor between the walls, the other way is to fix the floor to the walls with anchors. When anchorage is lacking or is even absent, gravitational forces cannot be transmitted from the floor to the walls any more and this leads to slipping between those structural elements. In figure 2.6a this failure mechanism, where the floor inside collapsed, can be observed.

#### ANCHORAGE FAILURE

There are several types of anchorage failure, depending on the type of anchors being used. One of these failure modes is failure of the material (metal) of the anchor itself. Another way how the anchorage can fail is due to rupture at the connections points. This could happen at floor connection where the anchor could shear loose from the floor frame, or at the wall connection where the anchor could be pulled out of the masonry.

*DIAPHRAGM RELATED FAILURE*

During an earthquake, failure of a diaphragm itself (e.g. concrete floors and walls) is rarely observed. However failure of this type is mostly visible at the sides of a masonry wall where the diaphragm pushes itself through the wall, due to the absence of a good shear transfer between the diaphragm and the masonry wall.

*COMBINED IN-PLANE AND OUT-OF-PLANE FAILURE*

In real life an earthquake doesn't occur in one direction only and the structural elements are excited in both their in-plane and out-of-plane direction. (Bruneau, 1994) gives an example of a combined failure mechanism:

*"As in-plane shear cracking occurs, some triangular cantilever wedges are produced, whose out-of-plane strength is significantly weaker than that of the original uncracked wall panel. While these isolated portion of the wall are more susceptible to out-of-plane failure, the on-site identification of such a failure mode is nearly impossible, and such failures will generally be attributed uniquely and erroneously to the sole effect of out-of-plane forces."*



(a)



(b)



(c)

**Figure 2.6:** Global failure mechanisms: (a) Lack of anchorage failure (b) Shear failure pier (c) Diaphragm related failure (Bruneau, 1994)

## 2.2 Finite element modelling

### 2.2.1 Concept finite element method

The main idea of this method is to transform the governing partial differential equations, that describe the behaviour of a structure, to a system of linear equations which can be solved by a computer. This transformation will be done by subdividing the construction by finite elements, which are connected to each other by their nodes. Each element has its own element stiffness matrix, which depends on the type of element being used and the material properties. Reassembling all these element stiffness matrices results in the global stiffness matrix of the whole system. With this global stiffness matrix is it possible to link external forces with nodal displacements. Thus, instead of linking the displacements and the forces by kinematic relations, a material model and equilibrium equations, the displacement field and the force vector are only linked through a global stiffness matrix (figure 2.7).

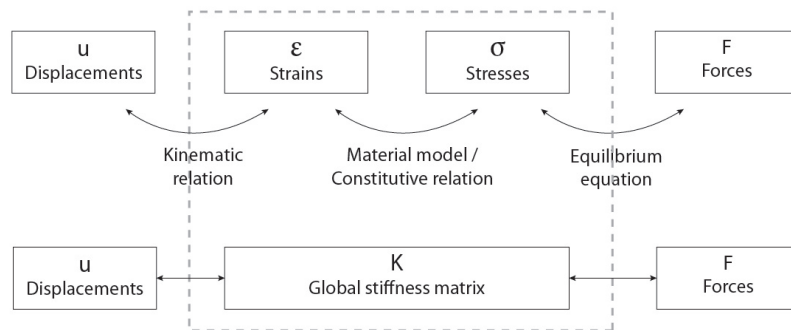


Figure 2.7: Structural analysis scheme

### 2.2.2 Computational modelling of masonry

#### Modelling approaches

Masonry is a composite material and consist of bricks (units) and mortar (joints), where a distinction is made between the head joints and the bed joints (see figure 2.8a). To model masonry different approaches can be adopted. One of these approaches is to model the masonry very detailed and this approach is denoted as micro-modelling (figure 2.8b). This way of modelling includes the units and the mortar by continuum elements as well as the interface between the mortar and the brick by discontinuous elements (interface elements), so this discrete approach models the cracks as discontinuities in the geometry. It leads however to large time requirements and memory, therefore a simplified approach is preferable (Lourenço et al., 1995).

The simplified strategy is called the meso-modelling approach. With this strategy the continuum elements, which represent the brick units, are expanded whereas the mortar and the brick-mortar interface are lumped in a zero-thickness discontinuous interface element (figure 2.8c). These interface elements open up when the tensile strength is exceeded. Like micro-modelling, this approach is very well able to trace crack-paths as this path is predefined by the interface elements. However, also this approach requires quite some memory and there are no fixed guidelines to derive correct values for the stiffness of the interface elements ( $k_n$  and  $k_t$ ).

The last modelling strategy has a totally different approach and is denoted as the macro-modelling approach or smeared crack approach (figure 2.8d). In this case the masonry is modelled as a composite and no distinction is made between the mortar and the bricks. The smeared crack approach regards the crack to be smeared over the whole element (figure 2.9). Even though the previous concepts with the discontinuous elements fit our perception of fraction, in literature it has been stated that

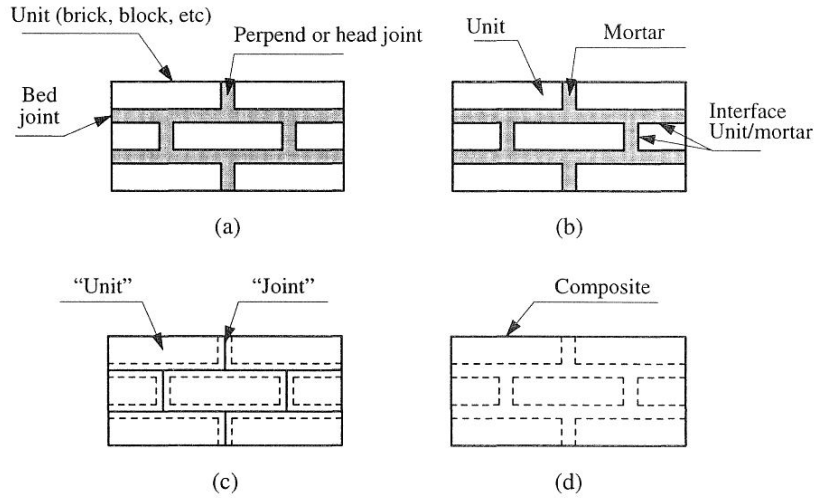


**Figure 2.8:** Modelling strategies for masonry structures: (a) masonry sample; (b) detailed micro-modelling; (c) meso-modelling; (d) macro-modelling (Lourenço, 1996).

the smeared approach might be more realistic in case of a diffuse crack pattern. Since the crack is smeared over the element it could be a good representation of a "band of micro-cracks" (Rots and Blaauwendraad, 1989). In this thesis the meso-modelling approach and the macro-modelling approach are used.

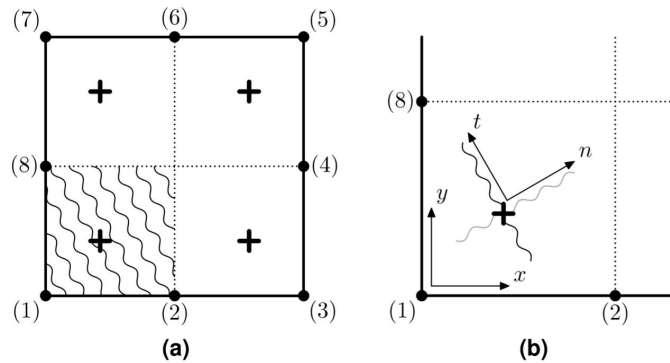


**Figure 2.9:** Smeared crack model: (a) The crack is smeared out over the tributary area of an integration point (b) Upon primary crack initiation the crack axes system is fixed with the n-axis perpendicular to the primary crack. Optionally, a secondary crack, perpendicular to the primary crack, may arise (Van de Graaf, 2017).

### Cracking models

Within each modelling approach a material model/crack model has to be chosen. In this thesis the number of possible crack models for the macro modelling approach is limited to the 'total strain based crack models'. For this type of crack model both tension and compression are described by one stress-strain relation, in contrary to the multi-directional crack model where the strain is divided into an elastic strain and a crack strain. For the total strain based crack model one can choose between the fixed and the rotating crack model. The first one could be a good representation of a real crack as the stresses and strains are evaluated in a fixed coordinate system (figure 2.9b), where the coordinate system is fixed upon cracking. The rotating crack model evaluates the stresses and strains in the principal directions of the strain vector, which keep rotating depending on the stress state in the element.

For an approach with interface elements a crack model for the interface elements has to be chosen. Two commonly used models are the discrete crack model and the Coulomb friction model. With the discrete crack model, mode-I (opening in normal direction) and mode-II (sliding in tangential direction) are uncoupled. The Coulomb friction model however couples these two failure modes (see figure 2.10).

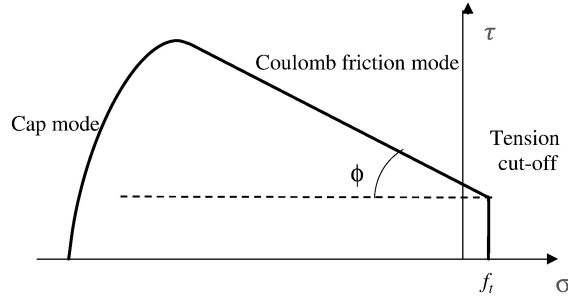


Figure 2.10: Coulomb friction model (Lourenço et al., 1995)

### 2.2.3 Finite elements

The types of finite element that are mainly used in this thesis are the 3D curved shell elements and the line interfaces between shells. The reason to choose for curved shell elements over plate or flat shell elements is that in case of curved shell elements the coordinates of the nodes don't have to be in a flat plane, which is important when one wants to account for out-of-plane behaviour. Besides the shell elements also plane stress elements are used. In this thesis these elements will be applied in order to verify the implementation of shell elements in the SLA code.

#### Plane stress elements

The plane stress elements are useful for situations with a Cauchy stress state, which means that the stress vector normal to the plane is zero ( $\sigma_{zz} = 0$ ). It has three degrees of freedom: two translations in the X- and Y-direction and one rotation around the Z-axis. Furthermore the nodes are located in one flat plane (XY-plane), therefore these elements will be used for 2D in-plane load cases.

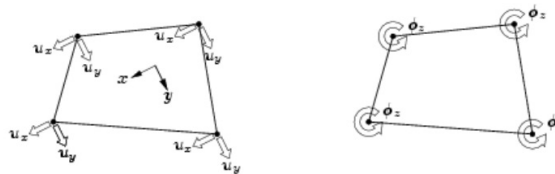


Figure 2.11: CQ16M Plane stress element (DIANA FEA BV, 2010).

#### Curved shell elements

The curved shell elements in Diana also assume a Cauchy stress state, but each node has five degrees of freedom: three translations in the global XYZ-directions and two rotations in the local x- and y-axis (see figure 2.12). The element has a quadratic interpolation scheme as the default (and only) one is 2x2 Gauss integration over the  $\xi\eta$  element area. The integration in  $\zeta$ -direction (thickness direction) may be Gauss or Simpson.

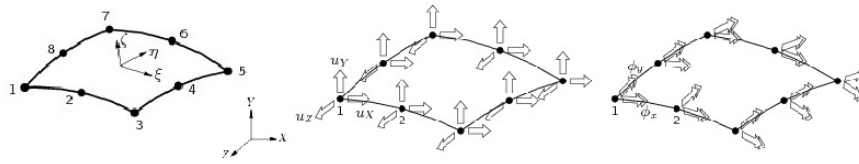


Figure 2.12: CQ40S Curved shell element (DIANA FEA BV, 2010).

### Interface elements in 2D configuration

The type of interface element that is compatible with 2D in-plane elements is element CL12I. The two degrees of freedom are the displacements in the local  $x$ - and  $y$ -direction, which are evaluated in the first node.

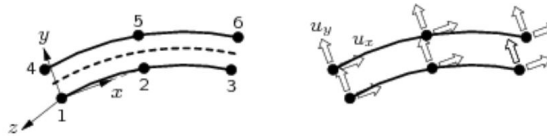


Figure 2.13: CL12I Interface element (DIANA FEA BV, 2010)

### Interface elements in 3D configuration

The type of interface element which is used in combination with shell elements in 3D configurations is CL24I. This type of finite element has four degrees of freedom per node: three translations in the local  $xyz$ -directions and a rotation in the local  $x$ -direction. Also these local directions are evaluated in the first node.

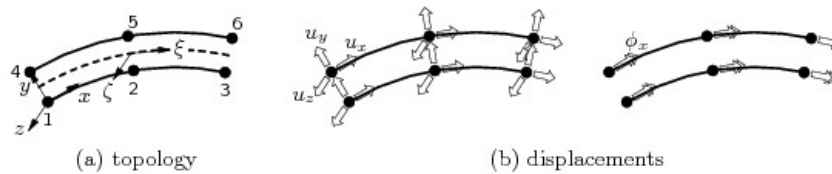


Figure 2.14: CL24I Interface element (DIANA FEA BV, 2010)

## 2.3 Non-linear analysis

Non-linear behaviour of a structure makes it complex to get insight into the response of these structures. Cracking, which is an important phenomenon of masonry, is an example of non-linear behaviour and will be of main interest throughout this thesis. Subsection 2 describes material non-linearities such as cracking. In order to analyse non-linear behaviour, numerical methods are developed, which are discussed in subsection 3. However current methods have limitations and often show divergence problems. These limitations are discussed in subsection 2.3.4.

### 2.3.1 Introduction

A structural analysis is about evaluating the response of a structure under an applied load. In the engineering field a linear analysis is often used to calculate this response and to investigate at which location forces will be highest. The calculations can be performed analytically and the response of different load systems can be obtained, because the principle of superposition holds (summation of the load cases). To perform a linear analysis, two fundamental assumptions have to be made: the structure is made of linear elastic material and the deformations are small. In case of linear static equations the displacements ( $\mathbf{u}$ ) can easily be calculated by finite element software, once the stiffness matrix ( $\mathbf{K}$ ) and the external force vector ( $\mathbf{f}$ ) are known:

$$\mathbf{K}\mathbf{u} = \mathbf{f} \quad (2.1)$$

However a linear analysis has its limitations, since it cannot predict the structural response in the failure range and it is not sufficient when non-linearities become dominant in the analysis, meaning that forces and displacements are not linearly related any more. Then a non-linear analysis is required.

In case of a non-linear problem the stiffness matrix (and in case of geometrical non-linearity the external force vector too) does depend on the unknown displacements, which makes this problem difficult to solve. For that reason numerical methods are developed to trace the non-linear equilibrium path.

### 2.3.2 Material non-linearity

There are three different types of non-linearity: material, geometric and contact non-linearity. In this thesis the focus lays primarily on material non-linearity. This type is related to the material model, which means that the stresses (internal forces) and strains are not linearly dependent any more. The material properties can for example depend on the current stress or strain state, time or temperature (Hendriks, 2015). Three well-known examples of material non-linearity are depicted in figure 2.15.

Figure 2.15a shows non-linear elasticity. During loading and unloading of a structure the stress-strain relation follows the curved equilibrium path. Another type of non-linear material behaviour is elasto-plastic or, as demonstrated in figure 2.15b, elastic-perfectly-plastic behaviour. The first linear branch is the elastic equilibrium path, which means that during unloading the structure goes back to

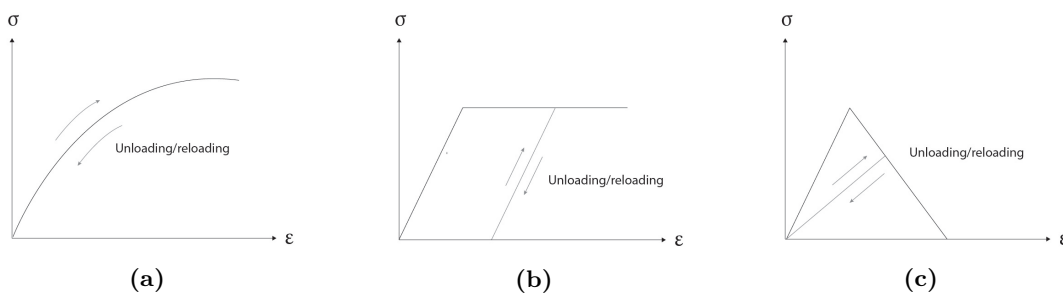


**Figure 2.15:** Material non-linearity: (a) non-linear elasticity (b) elastic-perfectly-plastic (c) cracking

its original state. Once the ultimate stress is reached, the structure deforms plastically. Unloading will follow the elastic path and a permanent deformation state is reached.

Of main interest during this thesis is cracking (figure 2.15c), which is an important phenomenon for brittle materials, such as concrete or masonry. After reaching the ultimate stress, the material starts to crack. Before the crack is fully developed, the material is still able to carry some load, but the more the cracks develop the less this load bearing capacity is. This phenomenon is called 'softening'. After cracking the material is damaged, which leads to a decrease of the material stiffness.

### 2.3.3 Numerical methods

In order to trace the non-linear equilibrium path of a structure, numerical methods are used. This section discusses these numerical methods.

The main idea is to apply the load in very small steps and to find the solution by linear approximations after each step. This could be realized with two different time stepping schemes (the implicit and explicit solver), which will both be discussed. The time stepping algorithms will be explained, based on the application of a force incremental procedure. Other load incremental procedures are described shortly as well.

#### Implicit and explicit solvers

The time stepping schemes can be divided into two groups: the explicit and the implicit schemes.

An explicit scheme is used in numerical software's such as UDEC, LS-Dyna and Abaqus (Rots et al., 2016). In case of an explicit scheme, information of the current time step ( $t$ ) is used to compute the solution of the next time step ( $t + \Delta t$ ) see equation (2.2) (Wells, 2011). After applying a load increment  $\Delta \mathbf{f}$ , the displacement increment is calculated, since  $\Delta \mathbf{u}$  is the only unknown.

$$\mathbf{K}({}^t \mathbf{u}) \Delta \mathbf{u} = \Delta \mathbf{f} \quad (2.2)$$

The new displacement vector will be:

$${}^{t+\Delta t} \mathbf{u} = {}^t \mathbf{u} + \Delta \mathbf{u} \quad (2.3)$$

Explicit algorithms generally require small time steps to ensure stability. In figure (2.16a) an example of instability is shown: the time steps are too big, therefore the obtained results drift away from the true equilibrium path (Kraus, 2014).

The other time stepping algorithm is the implicit scheme. The main difference with the explicit scheme is that this one ensures equilibrium through an iterative procedure, before applying the next load increment. The Regular Newton-Raphson Method (or Full Newton-Raphson) in figure 2.16b is a well-known example of such an iteration procedure. Other procedures are the Modified Newton-Raphson, Quasi-Newton (also known as the Secant Method) and the Linear or Constant Stiffness Method. The procedures work the same, but they use different stiffness matrices to calculate the approximate displacement field. In order to get more insight in the way these procedures work and to understand where these procedures fail, the Regular Newton-Raphson method will be explained, based on DIANA FEA BV (2010).

The first steps of an implicit scheme are the same as for the explicit scheme: a load increment is applied and with the stiffness matrix of the current time step the displacement increment  $\Delta \mathbf{u}_0$  can be calculated (equation 2.2). With the displacement increment the approximated displacement in time step ( $t + \Delta t$ ) can be determined as well:

$${}^{t+\Delta t} \mathbf{u} = {}^t \mathbf{u} + \Delta \mathbf{u}_0 \quad (2.4)$$

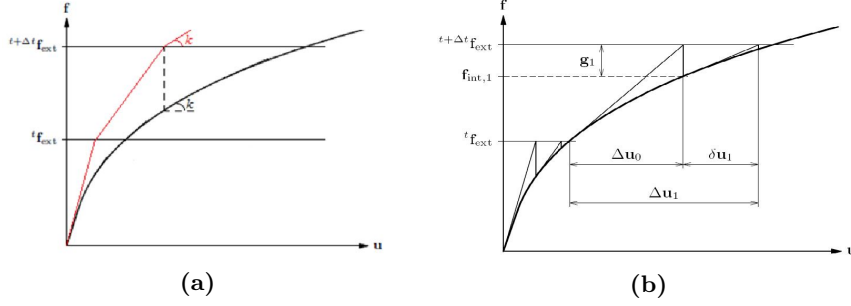


**Figure 2.16:** (a) Purely incremental scheme (Kraus, 2014) (b) Regular Newton-Raphson iteration scheme (DIANA FEA BV, 2010)

As said, the difference with the explicit algorithm is that the implicit algorithm search for equilibrium before moving on to the next load increment. First, the out-of-balance force has to be found:

$$\mathbf{g}_1 = {}^{t+\Delta t}\mathbf{f}_{ext} - \mathbf{f}_{int,1} \quad (2.5)$$

Subsequently the procedure checks whether the out-of-balance forces  $\mathbf{g}_1$  is small enough. In other words, the forces are assumed to be in equilibrium, if  $\mathbf{g}_1$  meets the convergence criteria, which are defined beforehand.

If there is no equilibrium, Newton-Raphson iterations are necessary. This will be done by applying an iteration increment  $\delta \mathbf{u}$ :

$$\delta \mathbf{u}_1 = \mathbf{K}({}^{t+\Delta t}\mathbf{u})\mathbf{g}_1 \quad (2.6)$$

where after the approximate displacement in time step ( $t + \Delta t$ ) will be updated:

$${}^{t+\Delta t}\mathbf{u} = {}^t\mathbf{u} + \Delta \mathbf{u}_0 + \delta \mathbf{u}_1 \quad (2.7)$$

The new out-of-balance force  $\mathbf{g}_2$  has to be checked and new iterations are necessary until the convergence criteria are met.

### Load incremental procedures

With the implicit and explicit solvers, elaborated in the previous subsection, small force increments are applied, meaning that these solvers were force-controlled. A problem with these force-controlled methods occurs once the applied force is bigger than the peak load/failure load of the structure. In that case, no solution can be found: the analysis diverge and this situation is called a 'snap-through' (figure 2.17a). Often a displacement controlled method (if available) is preferred: instead of a force increment, a displacement increment is applied. In that case it is possible to trace the post-peak

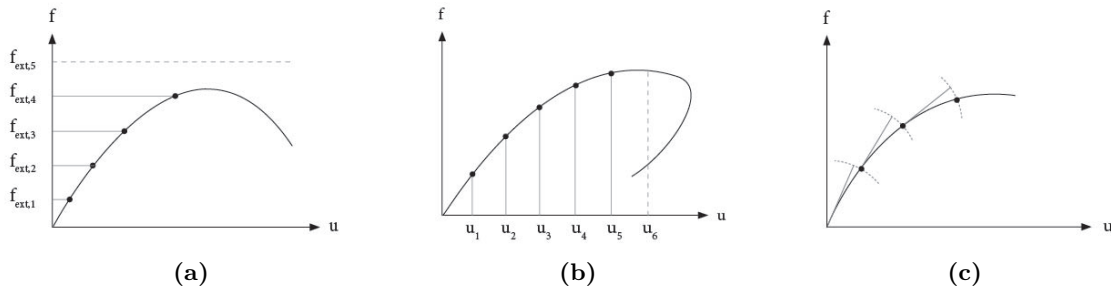


**Figure 2.17:** (a) Force control (b) Displacement control (c) Arc-length control.

behaviour of a structure. However this procedure has problems in case of a snap-back (figure 2.17b). In that situation the computer is not able to find one unique solution and another load incremental procedure has to be used. This could be the arc-length-controlled procedure, but also this procedure deals with non-convergence issues, e.g. in case of sharp snap-back's, where it is hard to define the optimal arc to keep the crack propagating in a stable way.

### 2.3.4 Limitations current numerical methods

In the previous section already some general problems are described concerning the force-controlled methods, used in the non-linear analysis. More difficulties arise in case of brittle fracture, which is an important characteristic of brittle material such as masonry or concrete. In that case a crack can arise very suddenly and propagates quickly. Because the strong variation in the deformations, the numerical software is not always able to find a converged solution.

Other non-convergence issues are often caused by the fact that the numerical software has to determine where a new crack starts and, in case of multiple cracks, which crack will propagate. In these cases of multiple equilibrium states (also called 'bifurcation'), non-convergence issues may arise.

Over the past decade, developers have proposed numerous improvements to increase the stability of numerical procedures. However using a method which is unconditionally stable would overcome all the non-convergence issues. Besides, the numerous options to run a non-linear analysis makes that the NLFEM heavily depends on the experiences and skills of the structural engineer or analyst.

## 2.4 Sequentially Linear Analysis

### 2.4.1 Concept

To address the divergence problems, during the simulation of non-linear behaviour, mentioned in previous section, Rots (2001) proposed an alternative method, called Sequentially Linear Analysis (SLA) which is able to deal with these problems. With this method, not a force, displacement or time increment but a damage increment is applied. The method performs linear analyses with a scaled reference load, after which a damage increment is assigned to one integration point in the computational model. A selection procedure is developed to be able to find this (critical) point, based on the current strength and stress distribution. With the damage increment, the stiffness and strength of the critical point are reduced and a new linear analysis with a new scaled load is performed. After unloading the structure and assigning the damage increment, forces will redistribute and a new critical point will be found. This procedure will continue until global failure of the structure is reached. The main advantage of this method is the fact that a linear analysis is inherently stable. In other words: with SLA it is possible to describe highly non-linear behaviour by performing linear analyses sequentially without the occurrence of convergence problems, since the linear analyses ensures equilibrium after each analysis step. The robustness of SLA makes it an attractive alternative for current NLFEA.

### 2.4.2 Stepwise secant material model

A fundamental assumption of Sequentially Linear Analysis is that the material degrades in a discretized manner. The continuum constitutive relation is transformed into a stepwise secant material law, which is also called a 'sawtooth law'. Figure 2.18a demonstrates a material model of a brittle material, including tension softening. The area under the graph is proportional to the fracture energy  $G_f$ . To implement this material law, it's transformed into a sawtooth law, which is depicted in figure 2.18b. Every branch shows a linear elastic relationship, with its own stiffness and strength. Assigning a damage increment, means a jump from one branch to the next. Van de Graaf (2017) and Rots et al. (2006) explain several concepts of how a sawtooth pattern can be described mathematically. They also come up with an improved concept, which ensures invariance of the fracture energy with respect to the number of sawteeth and ensures that the ultimate strain of the sawtooth law equals the ultimate strain of the fundamental material law. It can be seen from figure 2.18b that, instead of a continuous decrease of the stiffness and strength, the stiffness ( $E_k$ ) and it's corresponding strength ( $f_t$ ) reduce in a stepwise manner. Van de Graaf (2017) describes the secant stiffness as follows:

$$E_k = (1 - d_k)E_0 \quad (2.8)$$

The damage parameter  $d_k$  runs from 0 to 1 with discretized steps, where 0 means that the material is completely intact and 1 means that the material is fully damaged.

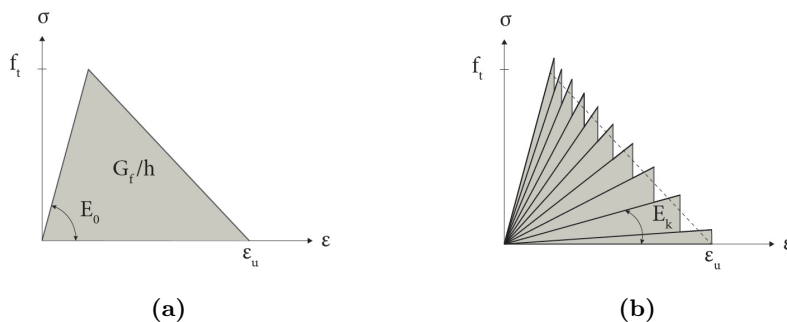


**Figure 2.18:** (a) Base material law (b) Discretized material law.

The sawtooth law is not only able to describe softening behaviour. Also snap-backs (at constitutive level) are possible to trace. Figure 2.19 shows such a sawtooth law. Even for sharp snap-backs, where current numerical methods fails, it is possible to describe that material behaviour.

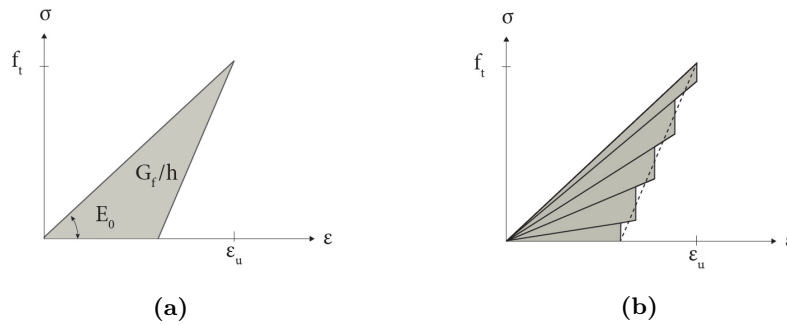


Figure 2.19: (a) Base material law (b) Discretized material law.

### 2.4.3 SLA procedure

After defining the sawtooth law the SLA procedure starts (see figure 2.20). To be able to run the first linear elastic analysis, a load has to be applied. This will be a reference load. Since this reference load will be scaled before running a linear analysis, the magnitude of the reference load doesn't matter. For now we assume that a unit load is applied, as Van de Graaf (2017) also did (step 1). With this reference load a linear elastic analysis is performed. Since this is a linear analysis, the analysis will be numerically stable and at each integration point the stresses and deformations are known for the given load.

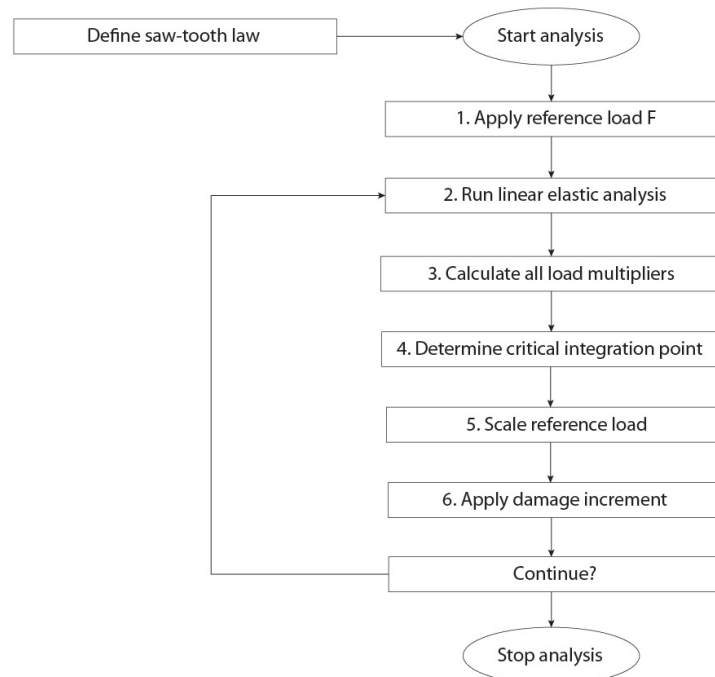


Figure 2.20: Work-flow SLA.

Next, it is case to determine which integration point in the structure will fail first. For now only cracking is considered as a failure mechanism. The selection procedure to find the critical integration point starts with calculating the critical load multiplier for every point (step 3), based on the current stresses and material strength. Van de Graaf (2017) defines the critical load multiplier as:

$$\lambda_{crit,i}^j = \frac{f_i^j}{\sigma_{gov,i}^j} \quad (2.9)$$

Where  $i$  corresponds to the integration point and  $j$  to the current cycle. The smallest load multiplier is for the integration point which stress is closest to the tensile strength and is therefore governing (step 4) for all  $\lambda_{crit,i}^j > 0$  (no negative stress components are taken into account yet). Step 5 scales the reference load, resulting in a critical stress state. The assumption is made this only happens in one integration point and that in other integration points the material strength is not exceeded. In the next step a damage increment is applied (step 6). After the application of the damage increment, the force will redistribute and a new integration point will become governing, where after a new critical load multiplier and a new scaled force can be calculate before running the second linear elastic analysis. This procedure will continue until global failure occurred or until another stop criterion (defined beforehand) is reached.

#### 2.4.4 Non-proportional loading

As explained in the previous section, all loads will be scaled by a load multiplier, where the magnitude of the load multiplier is based on the stress state of the critical integration point. This means that all loads will be multiplied with the same critical load multiplier (in literature referred to as 'proportional loading'). However, when there is a combination of initial/constant loads and live/variable loads, the identification of the critical load multiplier is more complex, since the initial load shouldn't be scaled. It should be present for 100% during the whole analysis and only the variable load has to be scaled by the critical load multiplier.

#### Superposition of loads

DeJong et al. (2008) introduced a strategy to deal with non-proportional load cases. Their method is based on superposition of the constant and the variable load assuming plane stress conditions (stress components perpendicular to the element are zero) and tensile failure only. The load combination is also denoted as:

$$\mathbf{F}_{crit} = \mathbf{F}_{constant} + \lambda_{crit}\mathbf{F}_{variable} \quad (2.10)$$

The steps are as follows:

1. Apply the constant load and determine the stresses ( $\sigma_{xx,con}, \sigma_{yy,con}, \sigma_{xy,con}$ ) by a linear analysis.
2. Apply a reference load and determine the stresses ( $\sigma_{xx,var}, \sigma_{yy,var}, \sigma_{xy,var}$ ) by a linear analysis.
3. To calculate the critical stress, the principle stress equation is used:

$$\sigma_{1,2} = \frac{1}{2}(\sigma_{xx} + \sigma_{yy}) \pm \sqrt{\frac{1}{4}(\sigma_{xx} - \sigma_{yy})^2 + \sigma_{xy}^2} = f_t \quad (2.11)$$

Set the principle stress equal to the tensile strength ( $f_t$ ) and substitute;

$$\begin{aligned} \sigma_{xx} &= \sigma_{xx,con} + \lambda\sigma_{xx,var} \\ \sigma_{yy} &= \sigma_{yy,con} + \lambda\sigma_{yy,var} \\ \sigma_{xy} &= \sigma_{xy,con} + \lambda\sigma_{xy,var} \end{aligned} \quad (2.12)$$

into the principle stress equation. This will result in two critical load multipliers ( $\lambda_{1,2}$ ) one for every principal direction, since the lambda's are the only unknowns in the equation. Also the principle directions (crack orientation) can be calculated using Mohr's circle.

4. Once, all load multipliers are calculated for every integration point, the critical load multiplier should be determined.
5. Scale the variable load by the critical load multiplier and obtain the new stress state by running a linear analysis with the critical load combination:

$$\mathbf{F}_{crit} = \mathbf{F}_{constant} + \lambda_{crit} \mathbf{F}_{variable} \quad (2.13)$$

6. Remove all loads and apply a damage increment, according to the sawtooth law, at the critical integration point
7. Start a new cycle by repeating all steps with the updated material properties until global failure occurs.

### DeJong's selection procedure of critical load multiplier

In case of non-proportional loading, the critical load multiplier is not always equal to the minimum of all load multipliers, but a distinction should be made between tension and compression.

The variable load has a crack opening effect in case of tension. In figure 2.21a the stress is closest to the tensile strength compared to the stress state in figure 2.21b and should be selected ( $\lambda_{min}^t$ ), because this integration point is about to exceed the tensile strength first.

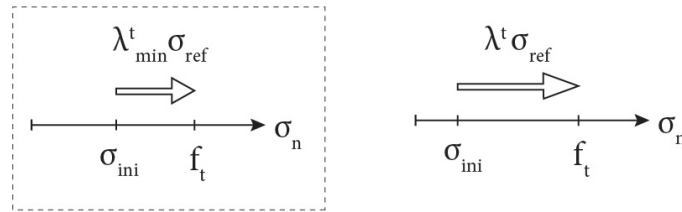


**Figure 2.21:** Crack opening effect of the variable load. The left situation is the governing one.

The variable load has a crack closing effect in case of compression. Comparing all these  $\lambda$ 's, the maximum one (figure 2.22b) should be chosen ( $\lambda_{max}^c$ ), because if the lambda is smaller, the stress of the corresponding integration point will exceed the tensile strength.

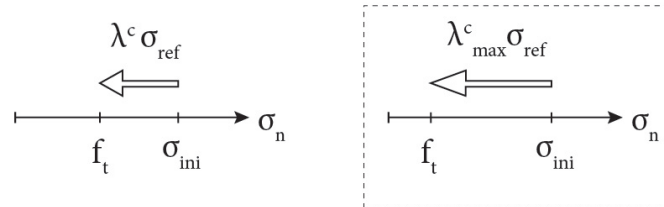


**Figure 2.22:** Crack closing effect of the variable load. The right situation is the governing one.

The last step is to compare  $\lambda_{max}^c$  with  $\lambda_{min}^t$ . In case  $\lambda_{max}^c < \lambda_{min}^t$  no integration point will exceed the tensile stress and  $\lambda_{crit}$  is set to  $\lambda_{min}^t$ . But in case  $\lambda_{max}^c > \lambda_{min}^t$  at least one integration point violates the material law. To be able to continue the DeJong's procedure  $\lambda_{crit}$  is set to  $\lambda_{max}^c$ .

### Discussion of non-proportional loading

Lots of discussions are still going on about the procedure mentioned above. Where this procedure is able to trace the failure process and to simulate the crack patterns of many loading situation relatively well, discrepancies still remain. One of the problems is already mentioned shortly in the previous section and is the problem that situations can occur where no value for  $\lambda_{crit}$  can be found without violation of the material law. Even  $\lambda_{crit} = 0$  is not possible.

This problem was the reasons to look for improvements of the non-proportional loading procedure. Van de Graaf (2017) suggested two procedures, which can be activated as soon as no valid load multiplier can be found. These procedures are based on double load multipliers. He writes the total load as:

$$\mathbf{F}_{crit} = \lambda_{ini}\mathbf{F}_{constant} + \lambda_{ref}\mathbf{F}_{variable} \quad (2.14)$$

Where  $\lambda_{ini}$  equals 1.

His first strategy is to not account for the variable load and to scale down the initial load ( $\lambda_{ini} = \lambda_{crit}$  and  $\lambda_{ref} = 0$ ), however ignoring the variable load and scaling down the initial load could give incorrect results. The second strategy is to scale the previous (successful) step. The total load therefore becomes:

$$\mathbf{F}_{crit}^j = \lambda_{crit}^j \mathbf{F}_{crit}^{j-1} \quad (2.15)$$

The advantage is that there's no violation of the material law and that the variable load is taken into account as well. However, scaling the previous load, means also scaling the initial load, whereby the initial load isn't fully applied any more. This means that the initial stress field is different than it should be and this could result in a different load distribution.

Eliáš et al. (2010) proposed a different approach for the non-proportional loading case. Whereas all previous mentioned procedures are load-unload (L-U) methods, their procedure is a gradual force release (F-R) method and is based on a well known phenomenon for brittle materials called 'avalanches of rupture' and can be defined as follows: "when a structural element breaks, the increased load (force)  $\mathbf{L}$  on the remaining elements may cause further ruptures, and thus induces a burst avalanche of a certain size ..." (Eliáš et al., 2010). Dealing with these avalanches is the main difference between their procedure and the ones mentioned earlier. Each time an element cracks, the strength of that specific element reduces and a redistribution of this released energy to the neighbour elements has to take place immediately, which is a dynamic phenomenon. The current sequentially linear procedure is a static method and cannot simulate this redistribution process properly. The quasi-static technique introduced by Eliáš et al. (2010) tries to deal with these avalanches of rupture. Instead of completely unloading, the load stays active on the structure as soon as the tensile strength is reached, gradually distribution takes place and it is possible for other elements to fail as well during this stage of redistribution of forces. Only when the equilibrium state is reached the analysis will continue and a load increment will be applied. Similar to the previous procedures, the reference load is scaled, but with this *redistribution* procedure the scaling factor is only applied to the stress increment of the variable load. It follows automatically that the total applied load is forced to increase, and the initial load will be fully applied in each analysis step. However the drawback of this procedure is the fact that it cannot deal with snap-backs, which was an important reason to develop the Sequentially Linear Analysis in the first place. Eliáš addressed this problem in his 'General method' (Eliáš, 2015), in which the F-R and the L-U methods are extreme cases, based on the time scales for the redistribution.

In the current development version of the numerical software Diana, the second strategy proposed by Van de Graaf (2017) is implemented. His approach concerns continuum problems, which is of main interest in this thesis.

### 2.4.5 Current state of SLA in DIANA 10.2

#### Plane stress and shell elements

At first SLA was only available for plane stress elements. However DeJong et al. (2009) proposed an extension of SLA to three-dimensional structures by the implementation of shell elements. This makes it possible to also analyse out-of-plane behaviour. For the undamaged case the following isotropic stiffness matrix for shell elements is used:

$$\begin{bmatrix} \sigma_{nn} \\ \sigma_{ss} \\ \sigma_{tt} \\ \sigma_{ns} \\ \sigma_{st} \\ \sigma_{tn} \end{bmatrix} = \begin{bmatrix} \frac{E_0}{1-v_0^2} & \frac{v_0 E_0}{1-v_0^2} & 0 & 0 & 0 & 0 \\ \frac{v_0 E_0}{1-v_0^2} & \frac{E_0}{1-v_0^2} & 0 & 0 & 0 & 0 \\ 0 & 0 & 0 & 0 & 0 & 0 \\ 0 & 0 & 0 & G_0 & 0 & 0 \\ 0 & 0 & 0 & 0 & G_0 & 0 \\ 0 & 0 & 0 & 0 & 0 & G_0 \end{bmatrix} \begin{bmatrix} \varepsilon_{nn} \\ \varepsilon_{ss} \\ \varepsilon_{tt} \\ \gamma_{ns} \\ \gamma_{st} \\ \gamma_{tn} \end{bmatrix} \quad (2.16)$$

Where  $G_0 = \frac{E_0}{2(1+v_0)}$ . They propose a fixed direction orthotropic cracking model. This means that as soon as in an integration point the tensile strength is exceeded, the crack direction will be fixed for that specific integration point and a distinction is made between the Young's modulus in the normal and in the tangential direction,  $E_n$  and  $E_s$  respectively. The values for  $E_n$  and  $E_s$  will decrease according to the predefined sawtooth law, to model the non-linear behaviour. From the point of cracking, the isotropic material law will not be adopted any more but will be replaced by the following stress-strain relationship:

$$\begin{bmatrix} \sigma_{nn} \\ \sigma_{ss} \\ \sigma_{tt} \\ \sigma_{ns} \\ \sigma_{st} \\ \sigma_{tn} \end{bmatrix} = \begin{bmatrix} \frac{E_n}{1-v_0^2} & \frac{v_{sn} E_n}{1-v_0^2} & 0 & 0 & 0 & 0 \\ \frac{v_{ns} E_s}{1-v_0^2} & \frac{E_s}{1-v_0^2} & 0 & 0 & 0 & 0 \\ 0 & 0 & 0 & 0 & 0 & 0 \\ 0 & 0 & 0 & G_{ns} & 0 & 0 \\ 0 & 0 & 0 & 0 & G_{st} & 0 \\ 0 & 0 & 0 & 0 & 0 & G_{tn} \end{bmatrix} \begin{bmatrix} \varepsilon_{nn} \\ \varepsilon_{ss} \\ \varepsilon_{tt} \\ \gamma_{ns} \\ \gamma_{st} \\ \gamma_{tn} \end{bmatrix} \quad (2.17)$$

This stiffness matrix will be updated between each linear elastic analysis.

However, in the SLA code used in this thesis, a simplification is implemented for the damaged shear stiffness. Instead of damaging the shear stiffness in a stepwise manner, like  $E_n$  and  $E_s$ , a constant shear stiffness is assumed which is:  $G_{ns} = G_{ns} = G_{ns} = \beta G_0$ . The initial shear stiffness is used, with a percentage of reduction by assuming a reduction factor, which is called the shear retention factor  $\beta$ . A similar strategy is assumed for the Poisson's ratio: the Poisson's ratio doesn't decrease in a step-wise manner but as soon as an integration point is critical for the first time, the Poisson's ratio drops to zero.

After crack initiation the stress-strain relationship used in this thesis will therefore be:

$$\begin{bmatrix} \sigma_{nn} \\ \sigma_{ss} \\ \sigma_{tt} \\ \sigma_{ns} \\ \sigma_{st} \\ \sigma_{tn} \end{bmatrix} = \begin{bmatrix} \frac{E_n}{1-v_0^2} & 0 & 0 & 0 & 0 & 0 \\ 0 & \frac{E_s}{1-v_0^2} & 0 & 0 & 0 & 0 \\ 0 & 0 & 0 & 0 & 0 & 0 \\ 0 & 0 & 0 & \beta G_0 & 0 & 0 \\ 0 & 0 & 0 & 0 & \beta G_0 & 0 \\ 0 & 0 & 0 & 0 & 0 & \beta G_0 \end{bmatrix} \begin{bmatrix} \varepsilon_{nn} \\ \varepsilon_{ss} \\ \varepsilon_{tt} \\ \gamma_{ns} \\ \gamma_{st} \\ \gamma_{tn} \end{bmatrix} \quad (2.18)$$

### Interface elements

Also for interface elements a distinction is made between the material law before and after cracking. Before cracking (the elastic stage), the tractions are coupled with the relative displacements by the initial stiffness:

$$\begin{bmatrix} t_n \\ t_t \end{bmatrix} = \begin{bmatrix} k_{n,0} & 0 \\ 0 & k_{t,0} \end{bmatrix} \begin{bmatrix} \Delta u_n \\ \Delta u_t \end{bmatrix} \quad (2.19)$$

After cracking the constitutive relation of these interface elements is replaced by a new one:

$$\begin{bmatrix} t_n \\ t_t \end{bmatrix} = \begin{bmatrix} k_n & 0 \\ 0 & k_t \end{bmatrix} \begin{bmatrix} \Delta u_n \\ \Delta u_t \end{bmatrix} \quad (2.20)$$

Where the normal and shear stiffness reduce according to their sawtooth law.

It is important to mention that the Coulomb friction model is not available yet, even though Van de Graaf (2017) proposed a way of implementing this material model. Besides, compressive failure in the interface elements is also not part of the current SLA code yet. For now, adjacent continuum element have to account for this type of failure in order to simulate compression failure.



Where  $F_r$  and  $F_l$  are the applied vertical forces,  $W_t$  is the self weight of the steel beam system and  $P$  is the imposed pre-compression, which was kept constant during the whole experiment. The vertical displacements  $v_r$  and  $v_l$  at the right and left side of the pier respectively were measured between the bottom and the top steel beams. These vertical displacements had to be equal to account for the fixed boundary conditions at the top.

### 3.1.3 Loading scheme

The structure was loaded in four steps. First the pre-compression was applied through the vertical actuators ( $F_r$  and  $F_l$ ) according to the condition mentioned above:  $F_r + F_l + W_t = P$ . The imposed pre-compression  $P$  was constant (0.6 MPa) throughout the whole experiment. Second, a force controlled cycle (C0F) was applied, this force (4 kN) was imposed to reach approximatively 20% of the expected maximum force, which is around 20 kN. The corresponding displacement after the first cycle was  $\pm 0.6$  mm. Third, another three cycles, C1D, C2D and C3D were applied in a displacement controlled manner. The displacement was equal to 1, 2 and 3 times the measured displacement in previous load step. Finally, a displacement controlled horizontal load was applied in 13 cycles (C1 till C13) to be able to trace to post-peak stage of the wall.

### 3.1.4 Stop criteria

The experiment was stopped once one of the following stop criteria was met:

1. A reduction of 20 % or more of the maximum base shear force is measured.
2. One of the vertical actuators (normally loaded in tension to apply pre-compression) is loaded in compression.
3. A displacement of 100 mm is reached in the horizontal actuator.
4. A safety risk is observed due to extensive damage.

### 3.1.5 Results

Esposito and Ravenshorst (2017) observed that the main damage occurred in cycle C13 in a rapid sequence. This sequence is illustrated in figure 3.3. The corresponding force-displacement graphs are plotted as well. The figure points out 6 moments during the experiment, namely one moment during cycle C12 and five moments during cycle C13. Until cycle C12, the wall showed a pure rocking behaviour (see figure 3.3a), then failure of the pier happened as follows: First, sliding over the mortar in the bed joints at the top and bottom of the wall occurred (figure 3.3b). Subsequently, vertical cracks in the brick elements were formed. Esposito and Ravenshorst (2017) state that the 50% reduction

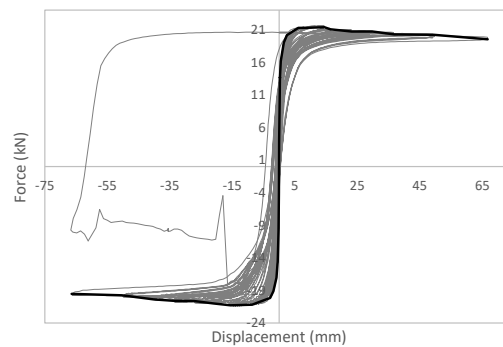


**Figure 3.2:** The backbone curve, obtained from the hysteresis loops.

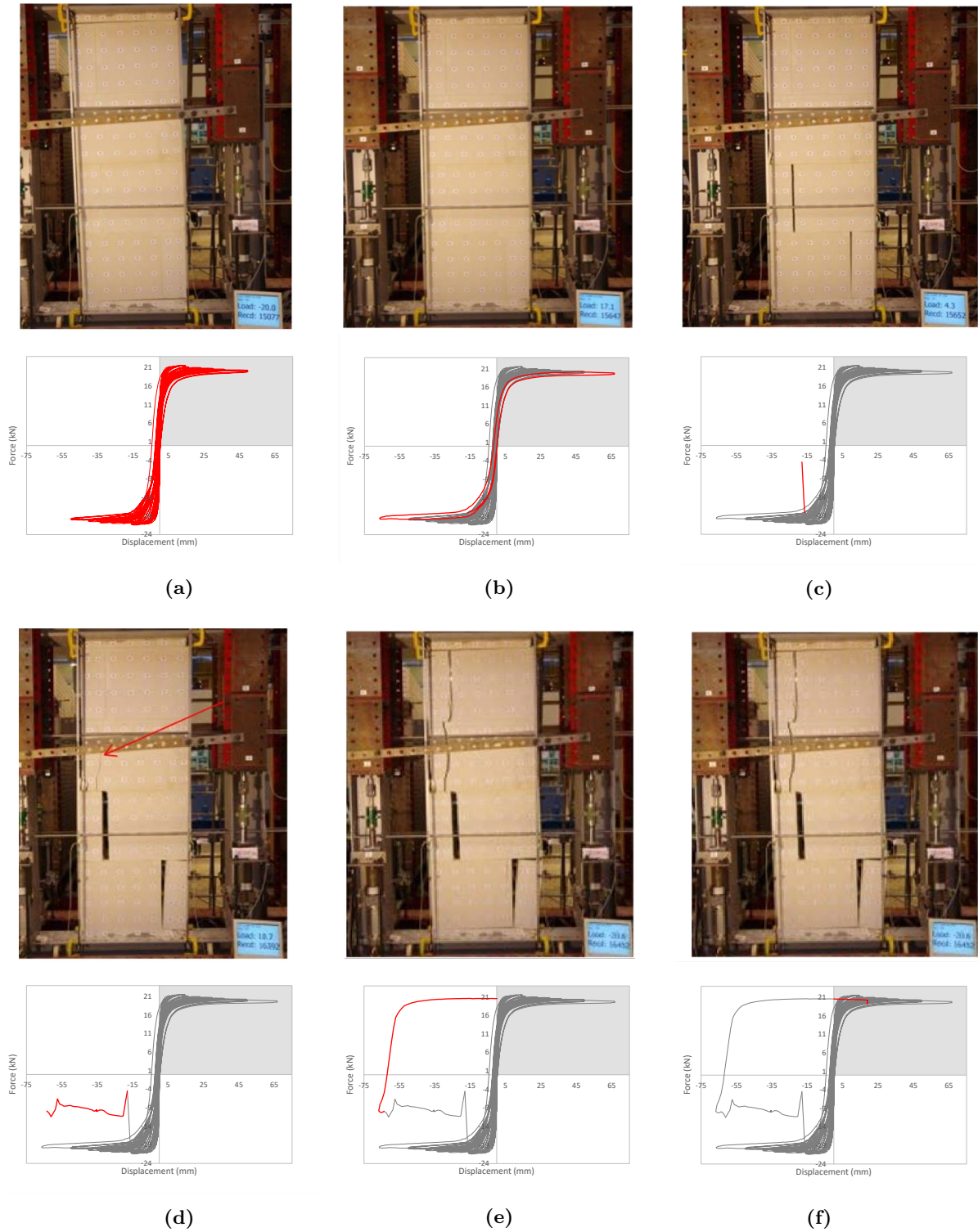


**Figure 3.3:** Crack formation during several loading cycles (a) C12 (b) C13-1 (c) C13-2 (d) C13-3 (e) C13-4 (f) C13-5. Photo's from Esposito et al. (2016)

in base shear force was probably caused by cracking in these elements (see figure 3.3c and 3.3d). Eventually, splitting. Eventually, splitting over the thickness of the small brick elements at the bottom occurred (figure 3.3e and 3.3f).

In the corresponding force-displacement graphs the hysteresis loops become clear. Using these hysteresis loops, a backbone curve (also known as an envelop curve) can be found (see black line in figure 3.2). This backbone curve is useful, as the numerical models in this thesis are exposed to a monotonic pushover load, instead of a quasi-static cyclic loading scheme. During a monotonic pushover no hysteresis loops will be observed in the FU-graph, but the capacity curve consist of one single curve only. The monotonic pushover on the pier will be performed by applying a displacement in the positive direction (see grey area in the FU-graphs in figure 3.3).

## 3.2 Experiment TUD\_COMP-28

### 3.2.1 Description

The out-of-plane loaded wall is composed of the same large CaSi-elements as experiment *TUD\_COMP-24* and it has a height of 2.725 m, a width of 1.448 m and a thickness of 0.12 m. An overburden load of 0.25 MPa is applied, followed by a out-of-plane cyclic load, which is applied using air-inflated airbags on both sides of the wall. The pressure in both airbags varies depending on the required external load.

### 3.2.2 Boundary conditions

Figure 3.4 shows the test set-up for the transversal wall subjected to out-of-plane loading. Only the top and bottom of the wall are constrained to study one-way bending failure. The top and bottom steel beams with rectangular hollow sections are rotationally stiff and are fixed to the bottom and top of the wall to account for clamped-clamped boundary conditions. The top beam is connected to the column via springs. These springs will be pre-tensioned in order to apply the overburden load. In this way, a vertical displacement of the wall is still possible.

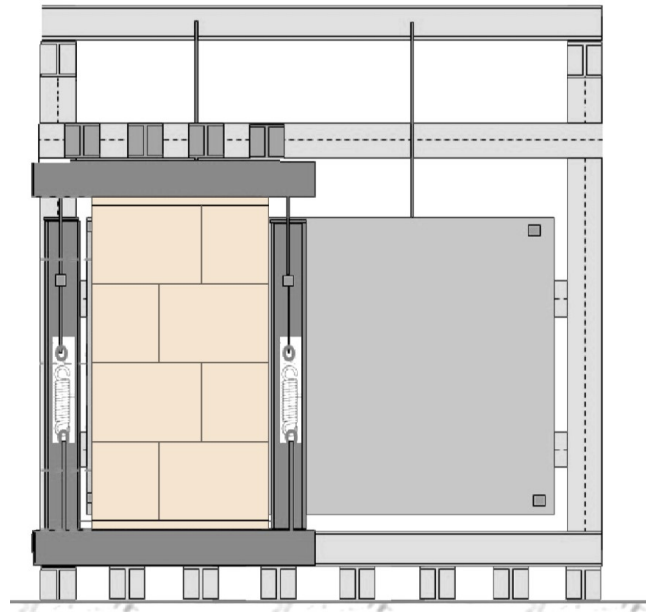


**Figure 3.4:** Test set-up of TUD\_COMP-28 (Damiola et al., 2017).

### 3.2.3 Loading scheme

The load is applied in a displacement controlled manner, by controlling the displacement at the mid-height of the wall. This displacement is varied in every cycle, where every cycle is composed of three identical runs. A run starts and ends with the wall at the initial position, then a displacement is applied in positive direction, where after a negative displacement is applied, by inflating or deflating the airbag at the south side (see figure 3.5). An initial pressure in the airbag at north side is enforced to prevent a negative pressure in the airbag at the south side.

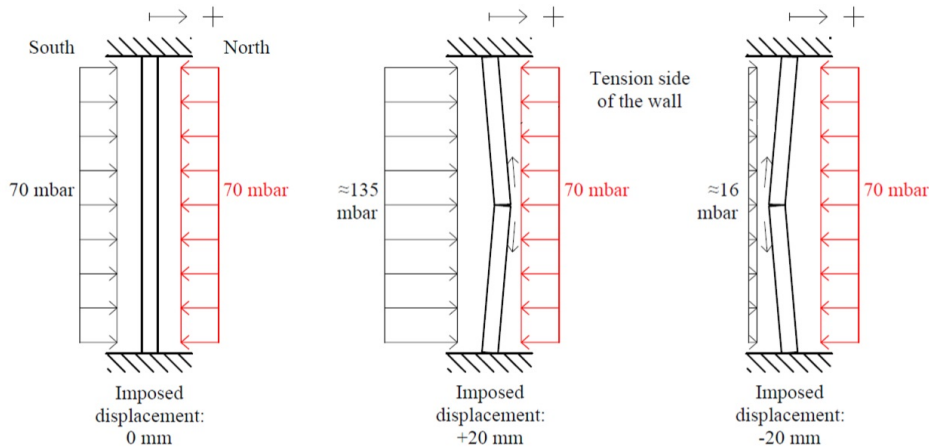


Figure 3.5: Example of airbag pressure during the test on the wall at cycle 10 (Damiola et al., 2017).

### 3.2.4 Stop criteria

No explicit stop criteria are defined at the start of the experiment. By following the loading procedure explained in previous subsection, sudden deformations leading to an unstable wall are prevented and no stop criteria are necessary to account for the safety during the experiment. However, the test set-up can only reach a displacement of  $\pm 100$  mm, since this is the maximum deformation of the airbags. Therefore the experiment will stop as soon as that point is reached.

### 3.2.5 Results

Figure 3.6 shows the results with respect to the capacity curve. A difference is observed between the positive and negative loading direction. Damiola et al. (2017) explain that this difference can possibly be attributed to the difference in airbag pressure. With a positive displacement of  $+20$  mm the airbag on the tension side has a pressure of 70 mbar, whereas the pressure in the airbag on the tension side is 16 mbar when a negative displacement is imposed. This causes a difference in friction, which attributes to the difference in the capacity curve. Damiola et al. (2017) recommend to take the capacity curve for negative displacements as representative for the walls behaviour in case a monotonic pushover test is performed.

The figure also shows the moments at which cracks in the bed joints are registered. Three cracks occur: in the top, middle and bottom of the wall. This crack pattern is illustrated in figure 3.7.

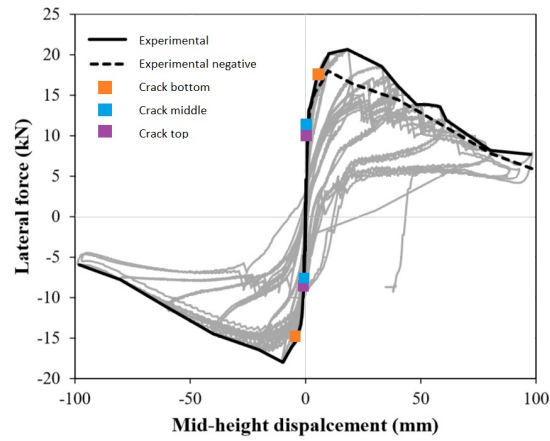


Figure 3.6: Capacity curve (Damiola et al., 2017).

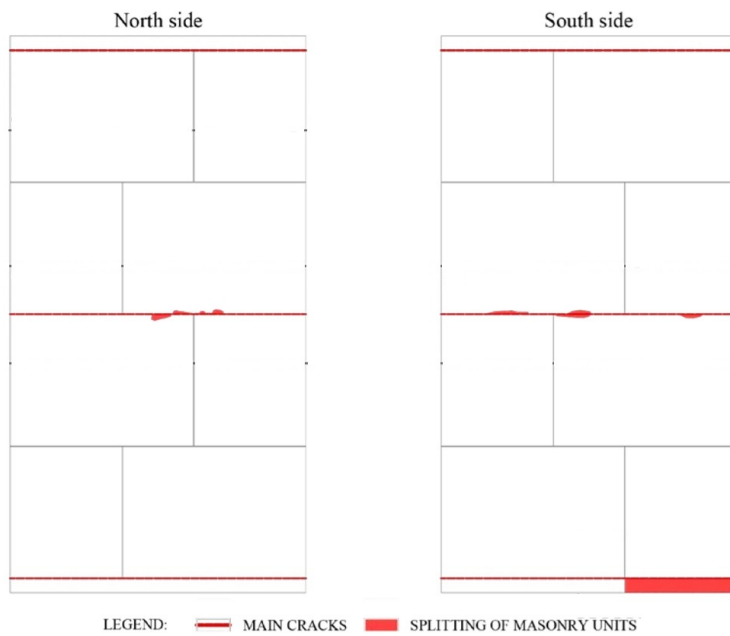


Figure 3.7: Crack pattern (Damiola et al., 2017).

## 4. Analytical calculations

In order to estimate the lateral shear force capacity and to verify the experimental results, analytical calculations are performed. In this chapter the calculations give an estimation of the failure load and deformation capacity. Section 1 starts with the calculations regarding the shear wall, using the same material parameters as in the numerical model. In Esposito and Ravenshorst (2017), also an estimation of the peak load is given. The section ends therefore with a comparison between the analytical outcomes. In section 2, the calculations are presented regarding the out-of-plane wall, considering the one-way bending situation. A reference is made to chapter 3 for the dimensions and parameters of both the shear wall and the out-of-plane wall.

### 4.1 In-plane loaded shear wall

#### 4.1.1 NPR9998 approach

In this section the base shear force capacity is calculated regarding four failure mechanisms, using the formulas in NPR9998 2017 Ontw. (Nederlands Normalisatie Instituut, 2017). The smallest load will be the governing failure load. Figure 4.1 shows these four different in-plane failure modes, which are also discussed in chapter 2: diagonal tensile failure, bed joint sliding, rocking and premature toe crushing.

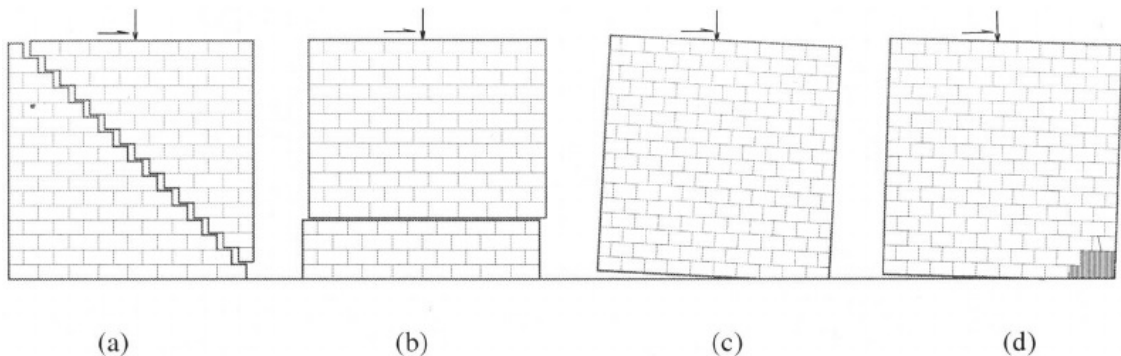


**Figure 4.1:** In-plane failure mechanisms: (a) Shear failure (b) Sliding failure (c) Rocking failure (d) Premature toe crushing (ElGawady et al., 2007).

#### Diagonal tensile capacity

The diagonal tensile failure mode (figure 4.1a) is an undesired failure mechanism as this a brittle failure mode (Nederlands Normalisatie Instituut (2017)) and it mainly occurs in a squatter pier. Even though the wall in experiment TUD\_COMP-24 is a slender wall, it will still be checked for this failure mode to get a complete overview of all failure loads. The maximum diagonal tensile strength of a pier, without flanges can be calculated as:

$$V_{dt} = f_{dt} A_n \beta \sqrt{1 + \frac{f_a}{f_{dt}}} \quad (4.1)$$

$\beta$  is a factor depending on the piers ratio. If  $\frac{h_{pier}}{l} > 1.5$  (in this case it's 2.81),  $\beta$  is equal to 0.67.  $A_n$  is the area of the horizontal cross section of the pier in  $mm^2$  and is equal to:

$$0.977 * 0.1 = 0.0977 m^2 = 97700 mm^2 \quad (4.2)$$

$f_a$  is the axial stress (in MPa) due to gravity loads, namely the overburden load and self-weight, calculated at the mid-height of the pier. The density is  $1824 kg/m^3$ , the overburden load is 0.6 MPa and half of the height is 1.372 m. This gives an axial stress of:

$$f_a = 1824 * 9.81 * 1.372 * 10^{-6} + 0.6 = 0.6245 MPa \quad (4.3)$$

$f_{dt}$  is the masonry diagonal tensile strength (in MPa) and a formula in NPR9998 is provided to find the diagonal tensile strength if no material test is performed:

$$f_{dt} = 0.5c + f_a \mu_f \quad (4.4)$$

With  $c = 0.83 N/mm^2$  (bed-joint cohesion) and  $\mu_f = 1.48$  (friction coefficient). Both values are according to Esposito and Ravenshorst (2017). This leads to a  $f_{dt}$  of  $1.34 N/mm^2$ .

The final diagonal tensile failure load will then be:

$$V_{dt} = 1.34 * 97700 * 0.67 \sqrt{1 + \frac{0.6245}{1.34}} = 106206 N = 106,2 kN \quad (4.5)$$

### Bed joint sliding

Bed joint failure (figure 4.1b) is a stable failure mode as it comes with sufficient deformation capacity: the structure deforms as a warning before total collapse takes place. If bed joint sliding would be the governing failure mode, the load capacity would be:

$$V_s = 0.7(t * L_w * c + \mu_f(P + P_w)) \quad (4.6)$$

$P$  is the overburden load in kN. With a prestress of 0.6 MPa, a thickness of 100 mm and a width of 977 mm, this load is:

$$P = 0.6 * t * L_w = 0.6 * 100 * 977 = 58620 N = 58.62 kN \quad (4.7)$$

$P_w$  is the self-weight in kN and is equal to:

$$P_w = h_{pier} L_w t \rho = 2.744 * 0.977 * 0.1 * 1824 * 9.81 = 4797 N = 4.8 kN \quad (4.8)$$

This results in a bed joint failure load of:

$$V_s = 0.7(100 * 977 * 0.83 * 10^{-3} + 1.48(58.62 + 4.8)) = 122.47 kN \quad (4.9)$$

### Premature toe crushing

Premature toe crushing (figure 4.1d) is followed by rocking and depends amongst others on the compression strength and pre-compression:

$$V_{tc} = (\alpha P + 0.5 P_w) \left( \frac{L_w}{h_{pier}} \right) \left( 1 - \frac{f_a}{0.7 f_m} \right) \quad (4.10)$$

$\alpha$  depends on the boundary conditions. When the top is free then:  $\alpha = 0.5$ ; and when the wall has fixed-fixed boundary conditions then:  $\alpha = 1.0$ . The next subsection will illustrate the cause for this difference between the  $\alpha$ 's. In the considered shear wall, the boundary conditions are fixed-fixed, resulting in a  $\alpha$  of 1.0.

$f_m$  is the masonry compression strength which is 10 MPa, according to Nederlands Normalisatie Instituut (2017). All parameters together give a base shear force capacity of:

$$V_{tc} = (1.0 * 58.62 + 0.5 * 4.8) \left( \frac{0.977}{2.744} \right) \left( 1 - \frac{0.6245}{0.7 * 10} \right) = 19.79 \text{ kN} \quad (4.11)$$

### Rocking

The rocking failure mechanism (figure 4.1c) is common for slender walls and is a stable failure mode as it comes with sufficient deformation capacity after cracking (Nederlands Normalisatie Instituut, 2017). To calculate the base shear force, NPR9998 presents the following formula:

$$V_r = 0.9(\alpha P + 0.5P_w) \left( \frac{L_w}{h_{pier}} \right) \quad (4.12)$$

It is very similar to the formula for premature toe crushing as these failure mechanisms are related to each other. However the last term in the equation for premature toe crushing  $\left( 1 - \frac{f_a}{0.7f_m} \right)$ , which depends on the compression strength and the gravity loads, is replaced by 0.9. Thus it depends on the material compression strength and the gravity loads which of these two failure mechanisms is governing.

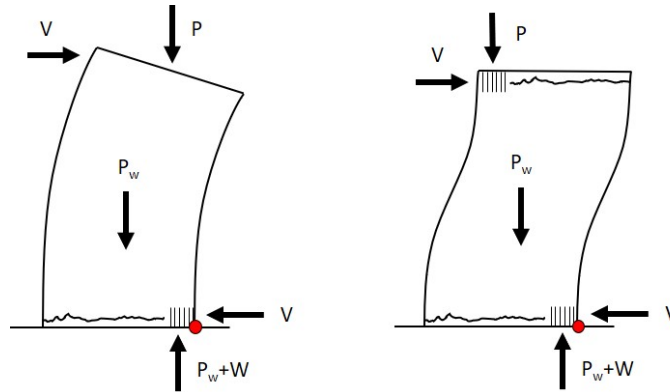


**Figure 4.2:** Influence boundary conditions on rocking failure capacity.

Figure 4.2 illustrates the influence of the boundary conditions on the rocking failure mode. The clamped-free boundary conditions only cause crushing and cracking at the bottom. The equilibrium of moments with respect to the red dot is:

$$Vh_{pier} - P_w 0.5L_w - P 0.5L_w = 0 \quad (4.13)$$

$$V = (0.5P + 0.5P_w) \left( \frac{L_w}{h_{pier}} \right) \quad (4.14)$$

For the situation with fixed-fixed boundary conditions the equilibrium of moments with respect to the red dot is:

$$Vh_{pier} - P_w 0.5L_w - PL_w = 0 \quad (4.15)$$

$$V = (1.0P + 0.5P_w) \left( \frac{L_w}{h_{pier}} \right) \quad (4.16)$$

These formulas are almost identical to the formula in NPR9998 (see formula 4.12), where  $\alpha$  is 0.5 for fixed-free boundary conditions and 1.0 for fixed-fixed boundary conditions. To account for toe crushing after pure rocking, NPR9998 adds a reduction factor of 0.9 (Esposito and Ravenshorst (2017)).

Using the parameters for the shear wall discussed in this thesis, the base shear force capacity will be:

$$V_r = 0.9(1.0 * 58.62 + 0.5 * 4.8) \left( \frac{0.977}{2.744} \right) = 19.55 \text{ kN} \quad (4.17)$$

19.55 kN is the lowest value of all failure modes and rocking is therefore the governing one. In the experiment a peak load of 21.6 kN is found, thus the expected peak load is close to the experimental peak load.

To find the deformation capacity related to this failure mode, NPR9998 uses the following formula for the drift limit:

$$d_{rocking} = 0.01 \left( 1 - 2.2 \frac{f_a}{f_m} \right) \sqrt[3]{\frac{h_{pier}}{L_w}} \quad (4.18)$$

$$d_{rocking} = 0.01 \left( 1 - 2.2 \frac{0.6245}{10} \right) \sqrt[3]{\frac{2.744}{0.977}} = 0.012 \quad (4.19)$$

This means that the maximum horizontal displacement at the top of the wall is 1.2 % of the height, thus the ultimate displacement is equal to:

$$u = d * h_{pier} = 0.012 * 2.744 = 0.0334 \text{ m} = 33.4 \text{ mm} \quad (4.20)$$

In the experiment a deformation of 66.8 mm is found, thus the formula in NPR9998 gives a conservative estimation of the deformation capacity.

### Difference with literature

Esposito and Ravenshorst (2017) presents analytical calculations as well to estimate the shear force capacity regarding the four different failure modes. Table 4.1 lists the differences between their results and the results demonstrated above.

**Table 4.1:** Comparison analytical results

	Analytical (literature)	Analytical (thesis)	Experiment
Diagonal tensile failure (Vdt)	106.10 kN	106.21 kN	-
Bed joint sliding (Vs)	117.49 kN	122.47 kN	-
Premature toe crushing (Vtc)	18.83 kN	19.79 kN	-
Rocking (Vr)	18.23 kN	19.55 kN	21.6 kN

Its becomes clear that the analytical results derived in this chapter are slightly higher than the results from Esposito and Ravenshorst (2017). The main explanation is that Esposito and Ravenshorst (2017) use the set-up and dimensions of the experiment in the analytical calculations, whereas in this thesis the dimensions of the numerical model are used. In the numerical model some small simplifications has been made, which leads to the following differences:

- Esposito and Ravenshorst (2017) use an effective height in the calculation for Vtc and Vr. The kicker layers of the masonry wall are glued to the steel beam, thus rocking only occurs in between these layers. In the calculations in this thesis the whole height is taken into account. If the wall is modelled based on the smeared crack approach, no masonry courses and thus no kicker layers are modelled and rocking occurs with respect to the total height.
- They use a correction factor to account for the fact that the horizontal force is applied at a certain distance from the top of the wall during the experiment. In the calculations above, no correction factor is used, because in the numerical model the horizontal force is applied exactly at the top of the wall.

- They use slightly different values for the walls height and width. The height is 2.743 m and the width is 0.977 m, which are used in the analytical calculations and the numerical model in this thesis. They however, use slightly different dimensions in the calculations, namely 2.715x0.979 m<sup>2</sup>.
- They use a masonry compressive strength of 12.69 MPa, based on destructive laboratory tests as part of the test campaign, whereas 10.0 MPa is used in the calculations above based on NPR9998.

### 4.1.2 Rigid block approach

Another way of finding the maximum external force is to consider the wall as a rigid block. When the sum of moments is calculated, an envelope curve for the rigid block behaviour can be obtained. Assuming small displacements, the equilibrium of moments with respect to the bottom corner is:

$$F * h - P * (w - u) - W * \frac{1}{2} * (w - u) = 0 \quad (4.21)$$

Where

$$P = 0.6 * t * w = 58.62 \text{ kN} \quad (4.22)$$

$$W = h * t * w * \rho * 9.81 = 4.795 \text{ kN} \quad (4.23)$$

Solving this equation, a relation between the displacement (u) and the maximum force (F) that the wall can take, is derived:

$$21.73 - 22.25u = F \quad (4.24)$$

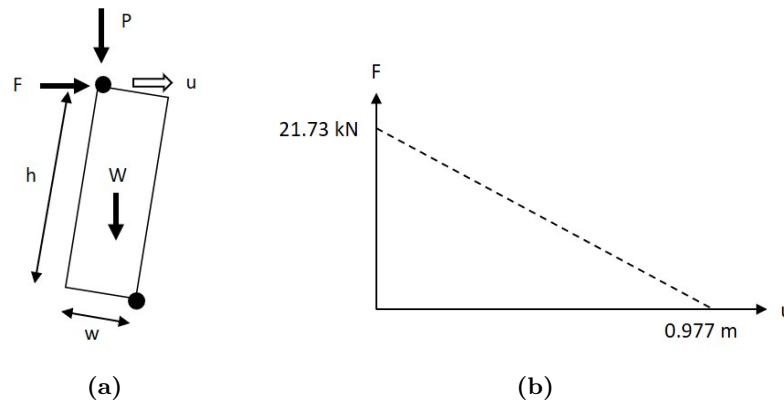


**Figure 4.3:** (a) Equilibrium of moments of pier as a rigid block (b) Expected capacity curve obtained from the rigid block approach.

This relation is also illustrated in figure 4.3b. It turns out that the rigid block approach gives an accurate estimation of the experimental peak load (see table 4.2).

**Table 4.2:** Comparison analytical results

	Analytical (NPR9998)	Analytical (rigid block)	Experiment
Rocking failure	19.55 kN	21.73 kN	21.6 kN

## 4.2 Out-of-plane wall

The other component of the TUD-building is the out-of-plane wall. The one-way out-of-plane failure mechanism is taken into account. Hereby it is assumed that once a mechanism is formed, due to hinges at the bottom, top and middle of the wall, the wall can be treated as a composition of rigid blocks.

### 4.2.1 Rigid block approach - virtual work

In Damiola et al. (2017) the method of virtual work is applied, based on figure 4.4, and it lead to the following equation:

$$\lambda(1-\beta)W\frac{u}{2} + \lambda\beta W\frac{u}{2} - W\frac{t}{2}\frac{u}{H_{eff}} - (1-\beta)W\frac{t}{2}\left(\frac{1}{\beta} + \frac{1}{2(1-\beta)}\right)\frac{2u}{H_{eff}} - P\frac{t}{2}\left(\frac{1}{\beta} + \frac{1}{1-\beta}\right)\frac{2u}{H_{eff}} = 0 \quad (4.25)$$

Where,

$$W_1 = W_2 = 0.5W = 0.5 * H_{eff} * w \quad \text{and} \quad F = \lambda * w \quad (4.26)$$

As the hinges are most likely be formed due to cracks in the mortar bed joints and as the bed joint are placed at equal distance between one another, the rigid blocks will have the same size, meaning that  $\beta = 0.5$ . Substituting  $\beta = 0.5$  and rewriting the equation gives:

$$F - W * t * \frac{4}{H_{eff}} - P * t * \frac{8}{H_{eff}} = 0 \quad (4.27)$$

The total applied external force is a function of the total self weight (W), pre-compression (P), effective height ( $H_{eff}$ ) and thickness (t). Substituting these dimensions gives a total force of 17.7 kN.

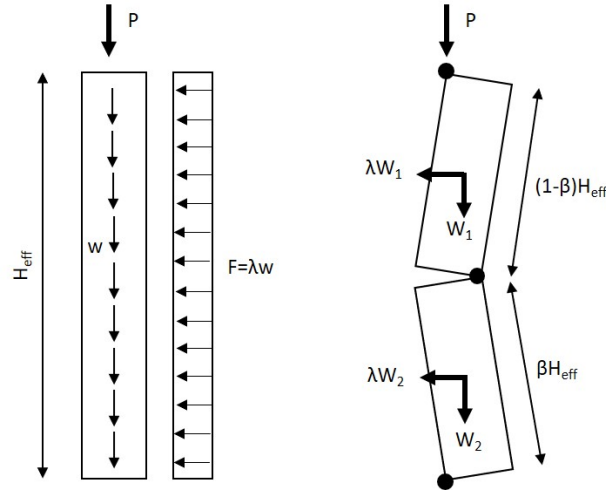


Figure 4.4: Rigid blocks model (Damiola et al., 2017)

### 4.2.2 Rigid block approach - sum of moments

Another way finding the maximum external force is to only look at one block and find equilibrium of moments. For now the bottom block is taken into account (see figure 4.5a) and the equilibrium of moment with respect to the bottom hinge is:

$$(P + S) * (t - u) + W * \frac{1}{2} * (t - u) - \frac{1}{2}F\frac{1}{2}H_{eff} = 0 \quad (4.28)$$

Where

$$S = \frac{1}{2} * h * t * w * \rho * 9.81 = 4.24 \text{ kN} \tag{4.29}$$

$$P = 0.25 * 0.t * w = 43.44 \text{ kN} \tag{4.30}$$

$$W = h_{eff} * t * w * \rho * 9.81 = 4.01 \text{ kN} \tag{4.31}$$

Solving this equation, a relation between the displacement (u) and the force (F) is derived:

$$18.49 - 154.05u = F \tag{4.32}$$

**Table 4.3:** Comparison analytical results

	Analytical (literature)	Analytical (thesis)	Experiment
One-way out-of-plane failure	17.7 kN	18.49 kN	18.0 kN

The total maximum force that can be applied is 18.49 (substitute u=0 in the equation above), which is higher than the force capacity derived from the virtual work method. Both methods require equilibrium of forces when the virtual work is zero and the sum of the moments is zero, therefore these results should be equal. The reason for this difference is that only the bottom block is taken into account. As the self weight is present, the precompression imposed by the self-weight is higher for the bottom rigid block than the top rigid block. When the sum of moment is calculated for the top block, a force of 17.0 kN is found. Taking the average of 17.00 kN and 18.49 kN leads to a force of 17,7 which is equal to the force, found using the virtual work equation. This leads to the capacity curve plotted in figure 4.5b.

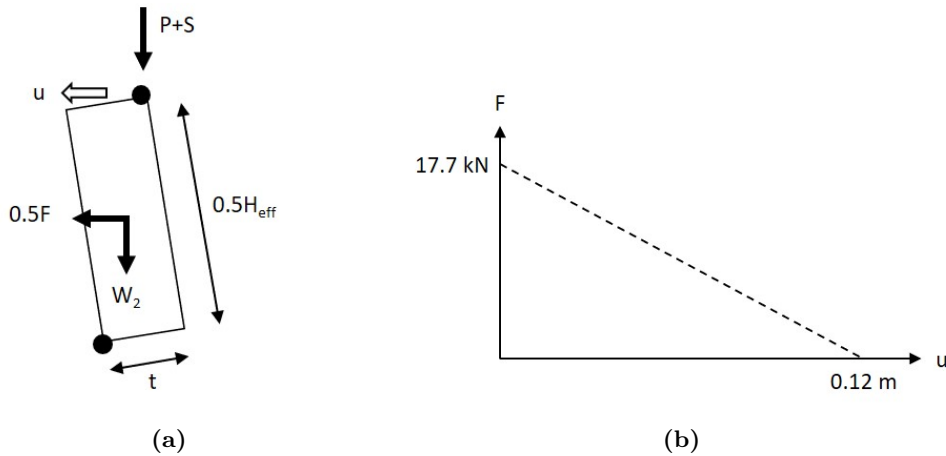


**Figure 4.5:** (a) Equilibrium of moments of one rigid block (b) Expected capacity curve obtained from the rigid block approach.



## Part II

# Numerical modelling



# 5. Shear wall: smeared crack approach

This chapter will elaborate on numerical modelling of the shear wall, using the smeared crack approach. The structure of this chapter is as follows. Section 1 explains how the finite element model is built. The second section gives an overview of all analyses being conducted. These analyses are part of a variation study, which is performed in section 3, where plane stress elements are used. The use of plane stress elements should be sufficient to model in-plane loading situations, as plane stress elements don't have degrees of freedom in out-of-plane direction. In section 4 shell elements are used to validate the (new) SLA implementation for shell elements, by comparing the results using shell elements with the results using plane stress elements. The chapter ends with a conclusion in section 5.

## 5.1 Finite element model

### 5.1.1 FEM model and material properties

A numerical model of the TUD\_COMP-24 experiment is illustrated in figure 5.1. The wall has a width of 0.977 m, a height of 2.744 m and a thickness of 0.1 m with an overburden load of 0.6 MPa. As explained in section 2.4.1., the smeared crack approach makes no distinction between mortar and bricks and the material properties used in the model are smeared over the whole wall. Table 5.1 lists these material properties, which are based on NPR998 (Nederlands Normalisatie Instituut, 2017) and Esposito and Ravenshorst (2017). In the table also the applied crack model is listed, which is the total strain based fixed crack approach as SLA is currently based on this type of crack model.

**Table 5.1:** Properties masonry for smeared crack concept

	Masonry (composite)		
Elasticity	$\rho = 1824 \text{ kg/m}^3$	$E_0 = 8800 \text{ MPa}$	$\nu = 0.21$
Tensile failure	$f_t = 0.4 \text{ MPa}$	$G_{ft} = 20 \text{ J/m}^2$	
Compressive failure	$f_c = 10 \text{ MPa}$	$G_{fc} = 20000 \text{ J/m}^2$	
Sawtooth parameters	$\beta = 0.01$	$p_{fac} = 0.1$	
Crack model	Fixed crack model		

The wall has clamped-clamped boundary conditions. The top is able to move in horizontal and vertical direction but is not able to rotate in the xy-plane. In the numerical model this is incorporated by the use of tyings. The red lines in figure 5.1c indicate the tyings. A tying can be used to "tie" elements of the first type (elements with translational degrees of freedom) to elements of the second type (elements with both translational and rotational degrees of freedom). However in this model a tying is used to copy the degrees of freedom of a "master" node, to the "slave" nodes. In the bottom of the wall, the "master" node (the middle node) is fixed in all three directions. The tyings make sure that all other bottom nodes are fixed in the same way. At the top of the wall, the "master"

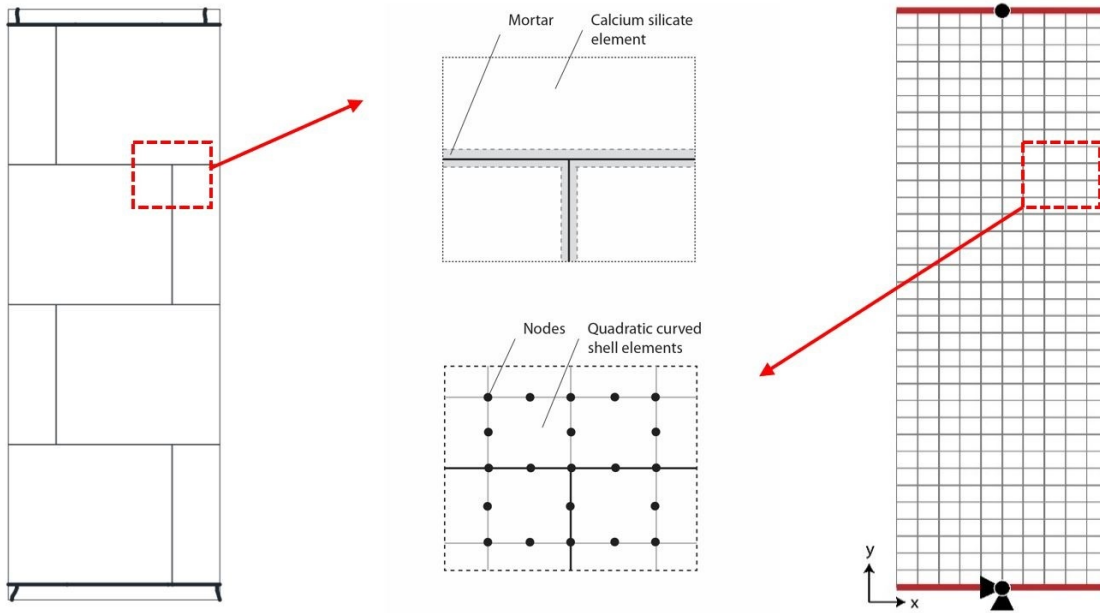


**Figure 5.1:** (a) Pier made of large CaSi-elements. (b) Top: detail of the pier. Bottom: detail of the numerical model. (c) Numerical model with smeared crack approach.

node is also located in the middle and is only fixed in z-direction, to prevent out-of-plane movement of the wall. The tyings at the top make sure that all top nodes will have the same displacement in x- and y-direction as the "master" node, therefore rotation of the top of the wall is constrained. An advantage of using tyings is that the reaction forces are lumped in the master node. This makes it easier to process the output later on. In the model eight-node quadratic elements with a mesh size of approximately  $0.1 \times 0.08 \text{ m}^2$  are applied. In case of plane stress elements the element type is CQ16M and in case of shell elements the element type is CQ40S (see section 2.4.2 for the element descriptions). In Diana the default (and only) integration scheme for CQ40S shell elements is a reduced  $2 \times 2$  Gauss integration scheme. In order to compare the results for different types of elements, the same reduced integration scheme for plane stress elements is used. The integration scheme in thickness direction for shell elements is the (default) 3-point Simpson integration. For plane stress elements there is only 1 integration point in the out-of-plane direction.

It is important to note that, in contrary to the experiment where a cyclic test is performed, the numerical model is exposed to a monotonic pushover load as a simplification. The main argument to do so, is the fact that in SLA there is no crack-closure algorithm yet, meaning that if there is a load reversal, incorrect results could be obtained. Before a horizontal pushover load is applied, the shear wall is exposed to an overburden load at the top of the wall. In the SLA method this is taken into account by modelling the wall in a non-proportional way (see section 2.2.4). The initial load is a combination of self-weight and an overburden load of 0.6 MPa at the top. This initial load has to be present constantly during the whole analysis. The second load is a variable load to account for the horizontal displacement at the top. A unit load of 1 Newton is used and this load will be scaled in every analysis step. In case of a regular non-linear finite element analysis (NLFEA) the loading scheme is incorporated by making use of a phased analysis. In the first phase the initial load is applied, which is again a combination of self-weight and pre-compression and in the second phase the lateral load (a horizontal displacement of 100 mm) is added. It is clear that in case of NLFEA a displacement controlled way of applying the "load" is preferred to be able to trace the post-peak behaviour of the structure.

### 5.1.2 Properties SLA

Besides the material properties some extra input is required, in case of SLA. This input is related to the sawtooth laws (material laws), which are depicted in figure 5.2. Figure 5.2a shows the sawtooth law for compression failure and it indicates three ranges. These colours will be used in strain-plots later on. The first one (light blue) goes up to the strain at which the maximum compressive strength  $f_c$  is reached. The second part is the crushing part, which is coloured in dark blue and the last one is coloured in pink, which represents the state at which the integration point is completely softened. In tension also three ranges are highlighted, namely the linear elastic state, cracking state and complete cracked state coloured in green, yellow and red respectively. The p-factor is taken as 0.1, meaning that compressive and tensile strength are exceeded by 10% in order to make the sawtooth law energy invariant (Van de Graaf, 2017). With this p-factor and the material properties listed in table 5.1, the sawtooth laws results in 22 sawteeth for compression and 18 for tension.

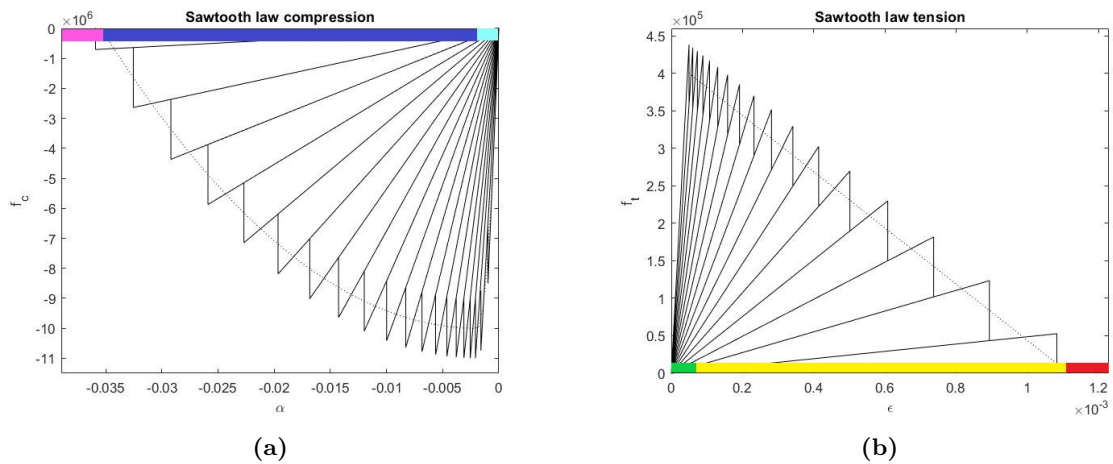


**Figure 5.2:** Sawtooth laws with three ranges highlighted: linear elastic range, cracking/crushing range and ultimate strain range for (a) compression (b) tension.

### 5.1.3 Properties NLFEA

The addition input with respect to NLFEA is related to the convergence criteria. With an imposed horizontal displacement at the top of 100 mm, a step size of 0.001 is assumed, meaning that every step size is 0.1 mm with 1000 steps in total. The convergence tolerance is set to  $10^{-4}$  and if the analysis step doesn't meet the convergence tolerance, the analysis is terminated. The reason for this is to be able to see how far the non-linear analysis is able to converge and this way the advantage of SLA, in terms of obtaining numerically stable results, becomes clear.

During the analyses the Modified Newton-Raphson is used (see section 2.1.3 for non-linear numerical methods) and the maximum number of iteration steps is set to 250.

## 5.2 Overview numerical models

### 5.2.1 Analyses in section 3 - plane stress elements

In section 3 a variation study will be conducted to investigate the influence of the Poisson's ratio, shear retention factor ( $\beta$ ) and crack model on the capacity of the wall. In the tables below, the second model is the base model. By varying different input parameters (marked in blue), the influence of these parameters is analysed. It's important to note that the SLA algorithm is based on the fixed crack approach. The influence of different crack models therefore only applies to the NLFEA. Furthermore only a constant shear retention factor is adopted in the current SLA-code, whereas a damaged based shear retention factor is possible for NLFEA.

**Table 5.2:** Analyses conducted in section 3

	SLA analyses			
SLA-1	$\beta = 0.01$	$\nu = 0.21$	$f_c = 10 \text{ MPa}$	$G_{fc} = 20000 \text{ J/m}^2$
SLA-2	$\beta = 10^{-6}$	$\nu = 0.21$	$f_c = 10 \text{ MPa}$	$G_{fc} = 20000 \text{ J/m}^2$
SLA-3	$\beta = 10^{-6}$	$\nu = 0$	$f_c = 10 \text{ MPa}$	$G_{fc} = 20000 \text{ J/m}^2$
SLA-4	$\beta = 10^{-6}$	$\nu = 0.21$	$f_c = 3 \text{ MPa}$	$G_{fc} = 2000 \text{ J/m}^2$

	NLFEA analyses			
NLFEA-1	$\beta = 0.01$	$\nu = 0.21$	$f_c = 10 \text{ MPa}$	$G_{fc} = 20000 \text{ J/m}^2$
NLFEA-2	$\beta = 10^{-6}$	$\nu = 0.21$	$f_c = 10 \text{ MPa}$	$G_{fc} = 20000 \text{ J/m}^2$
NLFEA-3	$\beta = 10^{-6}$	$\nu = 0$	$f_c = 10 \text{ MPa}$	$G_{fc} = 20000 \text{ J/m}^2$
NLFEA-4	Rotating crack model	$\nu = 0.21$	$f_c = 10 \text{ MPa}$	$G_{fc} = 20000 \text{ J/m}^2$
NLFEA-5	$\beta = \text{damage based}$	$\nu = 0.21$	$f_c = 10 \text{ MPa}$	$G_{fc} = 20000 \text{ J/m}^2$

### 5.2.2 Analyses in section 4 - shell elements

In section 4 the plane stress elements are replaced by shell elements in order to verify the implementation of SLA for shell elements. In the table below the parameters are listed.

**Table 5.3:** Analyses conducted in section 4

	SLA analysis			
SLA-5	$\beta = 10^{-6}$	$\nu = 0.21$	$f_c = 10 \text{ MPa}$	$G_{fc} = 20000 \text{ J/m}^2$

	NLFEA analysis			
NLFEA-6	$\beta = 10^{-6}$	$\nu = 0.21$	$f_c = 10 \text{ MPa}$	$G_{fc} = 20000 \text{ J/m}^2$

## 5.3 Plane stress elements

### 5.3.1 Stop criteria SLA

As SLA is still under development it is important to check the results carefully in order to improve the SLA implementation in DIANA. As it turned out that a couple of test models showed spurious results, the suspicion was raised that there might be some flaws in the implementation of the SLA code. To prove this, the damage history of three models are analysed in detail below, before the variation study is conducted. At the end of this section, three stop criteria are defined, which will be used henceforth. It is important to note that for all three models in this section the number of sawteeth for both compression and tension is equal for the sake of comparison:  $n_t = 18$  and  $n_c = 22$ .

#### Stop criterion 1 | model SLA-1

A first problem that occurs, is that some analyses will continue indefinitely if they aren't stopped manually. Analysis SLA-1 is one of these analyses. To find the reason for this problem, the damage history is analysed and the number of damage increments are counted, leading to an overview in figure 5.3.

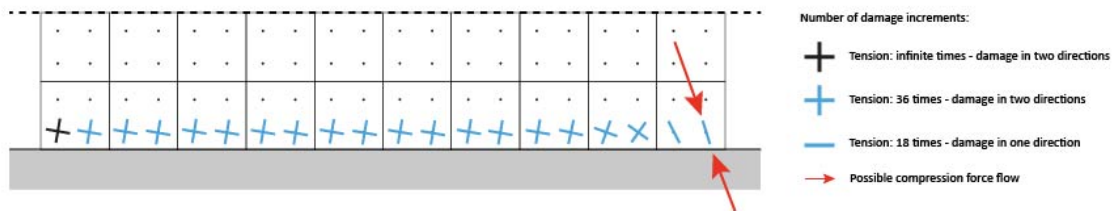


**Figure 5.3:** Damage increments at the bottom of model SLA-1. The angles of the principal directions are not the exact ones, as the output doesn't provide this information, however the angels are an approximation of the reality.

A few observations can be made: first, the reason why the analysis didn't stop is due to the outer left integration point, which is damaged infinite times. Apparently the analysis didn't stick to the number of sawteeth in tension, which is 18 for each of the two principal directions. Second, except for the two outer right integration points, the integration points where damaged up to 36 times, which is exactly two times the number of sawtooth, meaning that the integration points were completely damaged in both principal directions. The two outer right elements are only completely damaged in one direction, so the analysis could still continue, because compression forces could still be transferred in the other principal direction, see figure 5.4 for the compression force flow.

**Table 5.4:** Damage history of model SLA-1 at the bottom right and bottom left integration point

Bottom left: element 5, integration point 2						Bottom right: element 171, integration point 1					
Failure	n	Step	F[kN]	u[mm]	$\lambda[-]$	Failure	n	Step	F[kN]	u[mm]	$\lambda[-]$
Tensile	35	1192	20.59	5.00	1.0	:	:	:	:	:	:
Tensile	36	1249	20.58	5.53	1.0	Compr.	7	1315	20.51	10.59	1.0
Tensile	37	2157	20.44	156.70	1.0	Compr.	8	1321	20.50	12.33	1.0
Tensile	38	2158	20.44	156.70	1.0	Tensile	1	1339	20.40	13.46	1.0
Tensile	39	2159	20.44	156.70	1.0	Tensile	2	1340	20.39	1328	1.0
Tensile	40	2160	20.44	156.70	1.0	:	:	:	:	:	:
:	:	:	:	:	:	Tensile	17	1359	20.40	17.16	1.0
Tensile	inf.	inf.	20.44	156.70	1.0	Tensile	18	1361	20.40	17.61	1.0

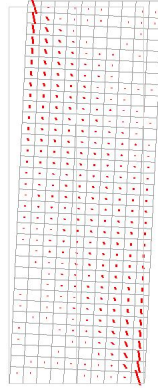


**Figure 5.4:** Compression diagonal

To give more exact information of the damage history, a table of the damage history of the outer right and outer left integration point is provided in table 5.4. For the right integration point first 8 damage increments in compression are applied before the integration point gets completely damaged in tension. As there is still some capacity left in the second principal direction, the analysis should still continue. However the number of damage increments of the left integration point gets infinite. Even though the results (force, displacement and  $\lambda_{ini}$ ) don't change in this case, the analysis still should stop automatically. This leads to the first stop criterion:

1. A step of an analysis is the last one as soon as the number of damage increments exceeds the number of sawteeth in both principal directions for any integration point in the model. This means either:
  - (a)  $18 \times \text{tension} + 18 \times \text{tension} = 36$  damage increments in tension, or
  - (b)  $18 \times \text{tension} + 22 \times \text{compression}$ , or
  - (c)  $22 \times \text{compression} + 22 \times \text{compression} = 44$  damage increments in compression

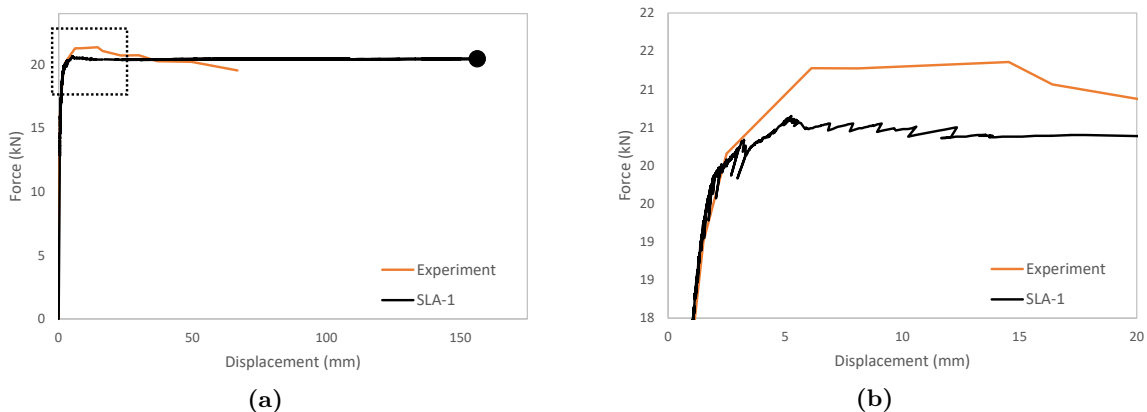


**Figure 5.5:** Results of model SLA-1: (a) Force-displacement graph (b) Zoom-in on force-displacement graph

The force-displacement graph is plotted in figure 5.5a. These force-displacement curves give information about both ductility and peak load of the structure. The final step, according to stop criterion 1, is marked with a dot. The figure shows that the peak load corresponds with the peak load of the experiment. The displacement is however about twice as much. In figure 5.5b a detail of the

FU-graph is plotted. The scaling of the applied external variable force in the SLA algorithm becomes clear in this picture as the FU-graph goes back and forth. Up to the peak load the snap-backs are secant, however, in a later stage, the snap-backs are almost horizontal, leading to a flat line, where the snap-backs are not visible any more. Applying the load in a non-proportional way comes with these non-secant snap-backs.

**Stop criterion 2 | model SLA-2 and SLA-4**

Model SLA-2 is used to show another incorrect event that might happen in case of SLA, using the current code and a second stop criterion is defined, based on this event. In figure 5.6 the damage increments at the bottom integration points of the model are visualized. This time the outer left integration point doesn't get damaged infinite times and the analysis stops automatically. Furthermore, at the right side not only tensile failure is observed, but also toe crushing.

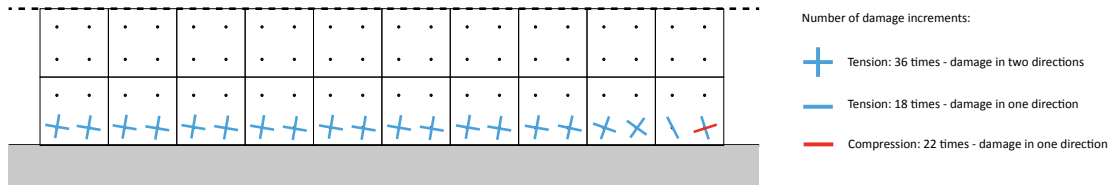


**Figure 5.6:** Damage increments at the bottom of model SLA-2. The angles of the principal directions are not the exact ones, as the output doesn't provide this information, however the angels are close to reality.

The problem becomes clear in table 5.5. Whereas the damage history of the outer left integration point doesn't show odd results, the damage history of the outer right integration point does. At some point of the analysis the initial load multiplier ( $\lambda_{ini}$ ) starts to decrease, which in this model leads to a negative displacement. This is physically not possible if a positive horizontal force is applied. In figure 5.7 the capacity curve and initial load multiplier are presented. If  $\lambda_{ini}$  isn't 1.0, it means that the initial load (pre-compression plus self weight) isn't fully present in the numerical model. It could be possible that  $\lambda_{ini}$  decreases, but that it will recover a few steps later. However if it decreases and it won't recover, it means that failure of the wall is initiated and the wall isn't able to carry the total load any more. Given this, and the fact that in this model a irreversible decrease of  $\lambda_{ini}$  led to a negative horizontal force, a second stop criterion is defined:

2. A step of an analysis is the last one as soon as  $\lambda_{ini}$  is not able to return back to 1.0.

**Table 5.5:** Damage history of model SLA-2 at the bottom right and bottom left integration point

Bottom left: element 5, integration point 2						Bottom right: element 171, integration point 1					
Failure	n	Step	F[kN]	u[mm]	$\lambda[-]$	Failure	n	Step	F[kN]	u[mm]	$\lambda[-]$
:	:	:	:	:	:	:	:	:	:	:	:
Tensile	29	851	19.86	2.25	1.0	Tensile	17	1339	20.42	13.62	1.0
Tensile	30	917	19.96	2.54	1.0	Tensile	18	1340	20.42	14.16	1.0
Tensile	31	971	20.09	2.83	1.0	Compr.	7	1549	20.48	71.32	1.0
Tensile	32	1026	20.17	3.22	1.0	Compr.	8	1550	20.48	72.23	1.0
Tensile	33	1093	20.27	3.84	1.0	:	:	:	:	:	:
Tensile	34	1136	20.39	4.38	1.0	Compr.	20	1661	5.54	-261.30	0.27
Tensile	35	1177	20.59	5.03	1.0	Compr.	21	1662	1.60	-74.32	0.08
Tensile	36	1239	20.54	5.59	1.0	Compr.	22	1663	0.02	0.58	0.0

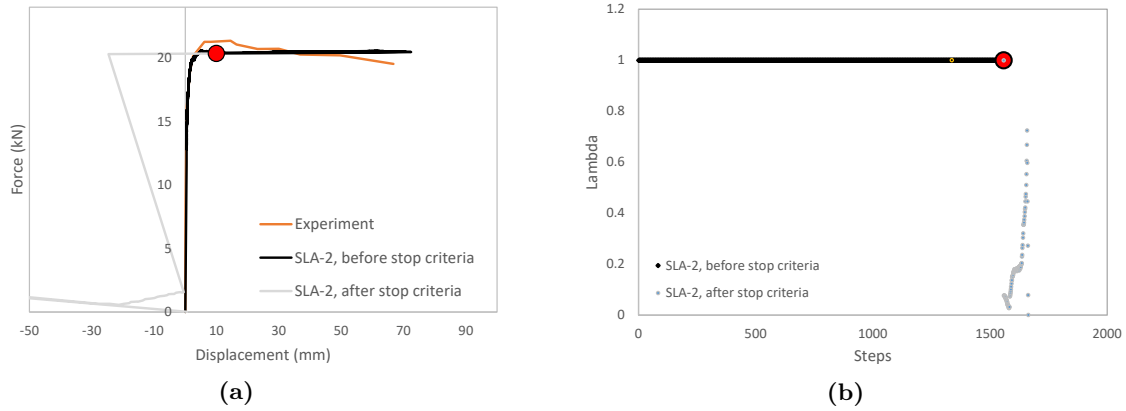


**Figure 5.7:** Results of model SLA-2: (a) Force-displacement graph (b) Initial load multiplier graph ( $\lambda_{ini}$ )

An extra analysis is conducted as a test case for the second stop criterion. In model SLA-4 the compressive strength is reduced to 3.0 MPa and the fracture energy in compression is reduced to 2000  $J/m^2$  in order to force toe crushing in the right bottom corner of the pier.

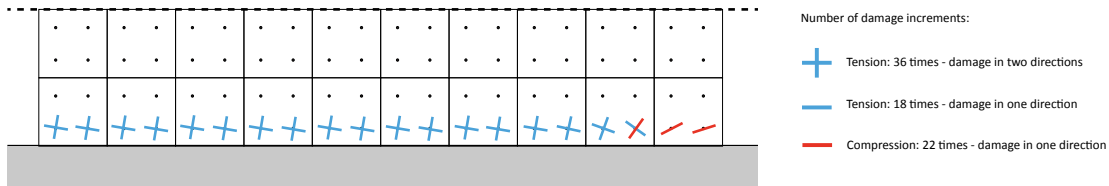


**Figure 5.8:** Damage increments at the bottom of model SLA-4. The angles of the principal directions are not the exact ones, as the output doesn't provide this information, however the angles are close to reality.

As expected, reducing the compressive strength, indeed leads to more toe crushing compared to the previous models (see figure 5.8). The damage history in table 5.6, shows complete tensile failure in both principal directions in the outer left integration point and complete compression failure in only one direction for the outer right integration point. When the FU-graph and  $\lambda_{ini}$  are plotted, the relation between them becomes clear again. In contrary to the previous model, a decrease of  $\lambda_{ini}$  doesn't lead to a negative displacement, but to a severe decrease of the force capacity in the FU-graph. The wall is not able to carry the total load and failure is initiated. This again shows the necessity for the application of the second stop criterion.

**Table 5.6:** Damage history of model SLA-4 at the bottom right and bottom left integration point

Bottom left: element 5, integration point 2						Bottom right: element 171, integration point 1					
Failure	n	Step	F[kN]	u[mm]	$\lambda$ [-]	Failure	n	Step	F[kN]	u[mm]	$\lambda$ [-]
Tensile	1	3	12.23	0.42	1.0	Compr.	1	67	15.74	0.57	1.0
Tensile	2	5	12.49	0.43	1.0	Compr.	2	68	15.71	0.57	1.0
:	:	:	:	:	:	:	:	:	:	:	:
Tensile	35	1337	8.51	10.68	0.49	Compr.	21	1237	11.05	9.14	0.64
Tensile	36	1399	8.42	11.98	0.48	Compr.	22	1272	9.35	9.52	0.54

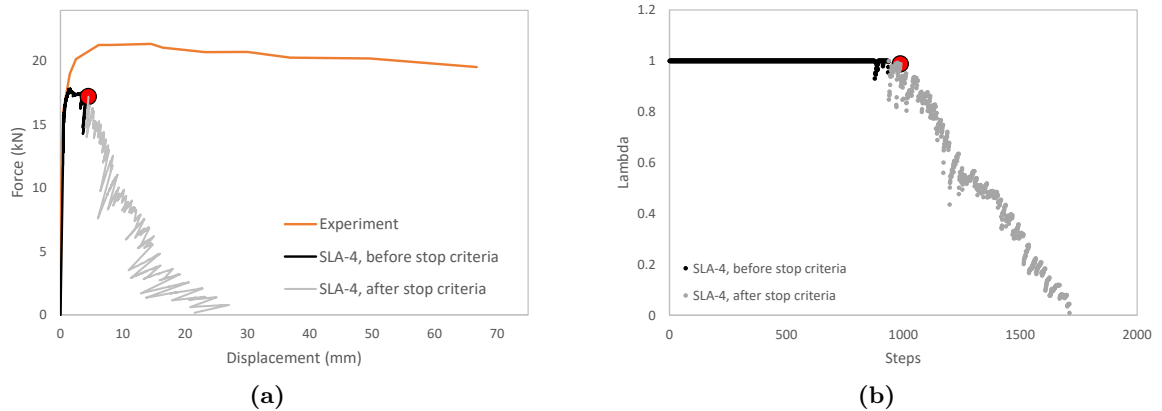


**Figure 5.9:** Results of model SLA-4: (a) Force-displacement graph (b) Initial load multiplier graph ( $\lambda_{ini}$ )

### Stop criterion 3

The third stop criterion regards the maximum displacement of the wall and it is based on the analytical calculations in chapter 4. According to the rigid block approach the wall will tumble if it reaches a displacement equal to the width of the pier (977 mm). This is theoretically the absolute maximum displacement the wall can reach, in case of purely rocking and therefore the third stop criteria is defined:

*3. A step of an analysis is the last one as soon as the displacement at the top of the wall gets larger than 977 mm*

### Summarizing stop criteria

In this section the stop criteria below are defined. They will be used henceforth.

A step of an analysis is the last one as soon as:

1. The number of damage increments exceeds the number of sawteeth for any integration point in the model. This means either:
  - (a) 18 x tension + 18 x tension = 36 damage increments in tension, or
  - (b) 18 x tension + 22 x compression, or
  - (c) 22 x compression + 22 x compression = 44 damage increments in compression
2. A step of an analysis is the last one as soon as  $\lambda_{ini}$  is not able to return back to 1.0.
3. The displacement at the top of the wall gets larger than 977 mm.

### 5.3.2 Shear locking

The smeared crack approach is still under discussion. There are different opinions especially about how to cope with shear stresses after cracking and how to implement this in numerical models. To assume zero normal stresses and shear stresses after cracking is a crude approximation of reality as cracks are often still capable of transmitting normal and shear stresses due to tortuous debonding and interlocking (Rots and Blaauwendraad, 1989). Therefore an option is to re-apply the initial isotropic material stiffness, after cracking, with some percentage of reduction by assuming a reduction factor which is called the shear retention factor  $\beta$ .

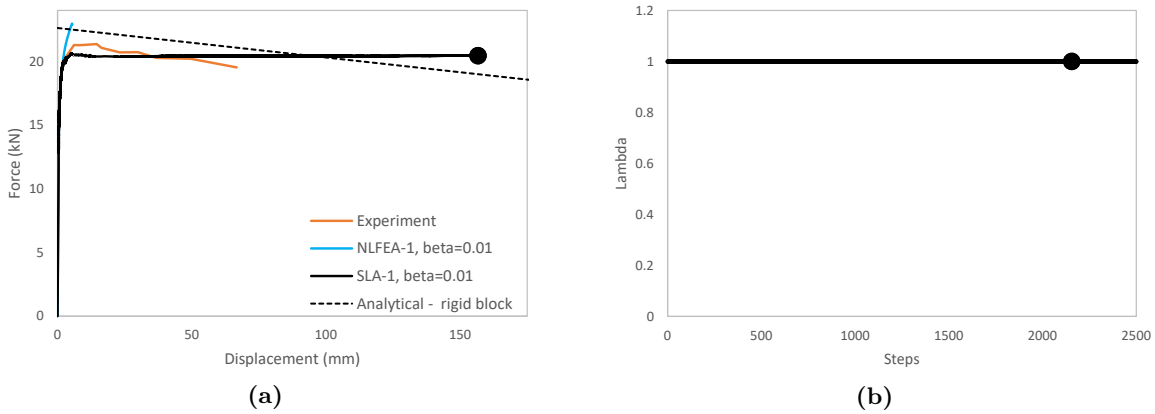


**Figure 5.10:** Results for  $\beta = 0.01$  (a) Force-displacement graph (b) Initial load multiplier  $\lambda_{ini}$

In analyses SLA-1 and NLFEA-1, the shear retention factor is assumed to be 0.01 and the capacity curves, obtained from these analyses are plotted in figure 5.10a, with the displacement on the x-axis and the force on the y-axis. For the SLA-1 analysis the first stop criterion is governing, as discussed in section 5.3.1. The outer left integration point at the bottom was about to exceed the number of sawteeth in step 2157 and therefore step 2156 is assumed to be the last step. Stop criterion 2 isn't governing, as the initial load multiplier doesn't degrade (see figure 5.10b) and criterion 3 isn't governing as well, as the analysis goes up to a displacement of 156.7 mm, where a maximum displacement of 977 mm is allowed.

When the SLA analysis is compared with the analytical rigid block approach and the experimental capacity curve, a difference becomes clear with respect to the shape of the curve. Where the experi-

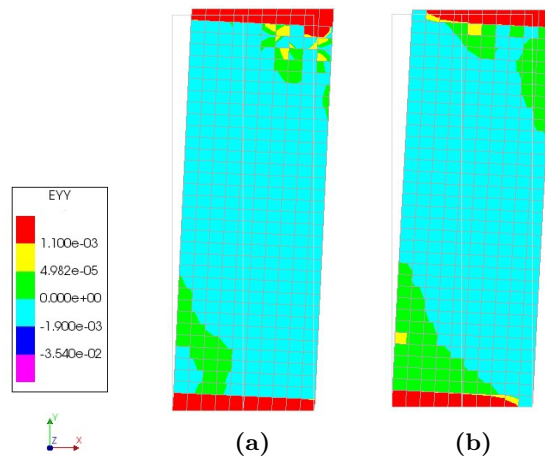


**Figure 5.11:** Eyy at the last step of (a) Model SLA-1 (b) Model NLFEA-1.

mental curve and analytical rigid block calculation show a reduction of the base shear force, the peak load of SLA-1 stays constant. The rocking motion of the pier causes this decrease of the load, as showed in chapter 4, but to model this numerically, geometrical non-linearity should be activated. This is not possible in combination with SLA yet, therefore no declined curve is observed. Furthermore the way the wall in the experiment fails is different than the way the numerical models fail. In the experiment a sudden drop of the base shear force occurs due to vertical cracking in the joints and in the continuum elements. In the numerical models using SLA, the analyses are forced to stop as soon as one of the stop criteria is met and no vertical crack is observed. In the models using NLFEA, the analyses terminate due to non-convergence issues and also here no vertical cracks occur.

Also NLFEA-1 stopped due to non-convergence issues before the wall collapsed. The statement that the wall hasn't failed yet is based on figure 5.11b, where the strains in y-direction are displayed. The colours correspond with the colours in the material laws (figure 5.2), where red indicates a completely cracked state of the material. The bottom right element and the top left elements still have capacity left, as they didn't reached the fully cracked or completely crushed state and therefore the wall is not collapsed yet.

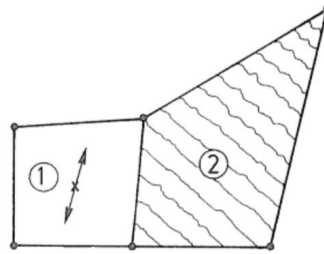


**Figure 5.12:** Consequence of displacement compatibility in smeared cracking concept. Strain of inclined crack at element 2 induces locked-in stress at element 1 (Rots and Blaauwendraad, 1989)

A clear difference can be observed in the FU-curves between NLFEA and SLA: analysis NLFEA-1 shows over-stiff results, whereas SLA-1 corresponds with the experimental and analytical results with respect to the peak load. The over-stiff response is caused by a well-known problem that comes with NLFEA: shear locking. This plays an important role especially when the shear retention factor  $\beta$  is too high. Rots and Blaauwendraad (1989) explain how shear locking does arise and it is illustrated in figure 5.12. Element 2 is subjected to tensile straining and due to displacement continuity, element 1 is strained as well, which leads to additional shear stresses. To overcome this problem, a value of  $\beta = 10^{-6}$  is used and the capacity curves are plotted in figure 5.13. In the left figure the complete

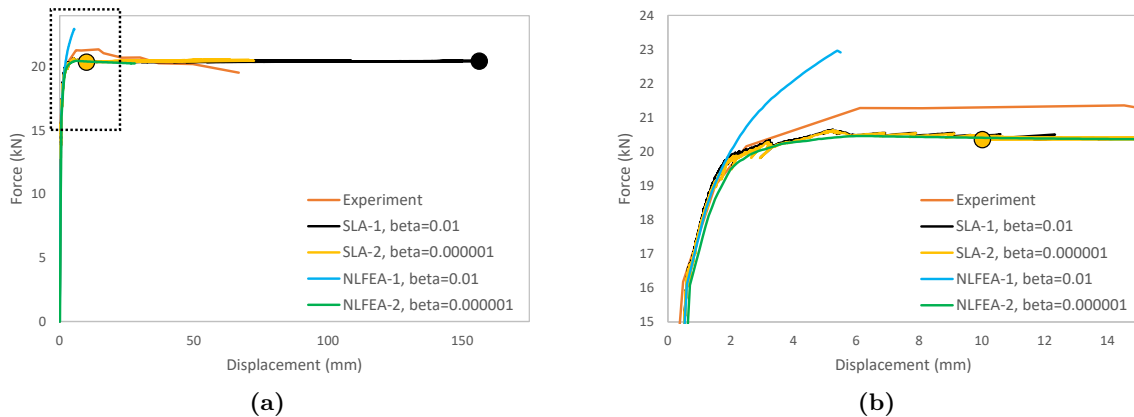


**Figure 5.13:** Force-displacement diagrams for different values of  $\beta$  (a) Complete curve (b) Zoom-in close to the peak load

capacity curve is shown, whereas on the right, a zoom-in is plotted to get a better look at the differences between the analyses. Indeed a  $\beta$  close to zero solves the shear locking problem, as the NLFEA-2 analysis doesn't give over-stiff results. To illustrate why shear locking causes an over-stiff response, the shear stresses at the bottom of the wall are plotted in the figure below at two different moments of the analyses. The first moment is when the top of the wall is displaced 0.6 mm. At that moment most elements of the wall are still in their linear elastic state, only the first two elements at the bottom left are damaged in tension, meaning that a crack is initiated. In figure 5.14c the shear stress at the bottom of the wall are plotted, corresponding to damaged state in figure 5.14a. No shear stresses are visible for the cracked elements, whereas there are shear stresses visible for the uncracked elements. At this deformed state of the wall ( $u=0.6$  mm), the shear stresses are equal for every analysis. In figure 5.14b the damaged state is drawn for the situation where the top of the wall has a horizontal displacement of 4.5 mm. At that moment, the crack is fully developed up to the last bottom right element (which is marked by a dashed line in figure 5.14d). Here the issue of shear locking becomes clear. For the complete damaged elements, a zero shear force is expected as a material is not able to transfer shear forces as soon as the material is fully cracked. However, in case of NLFEA-1 still some shear forces for the fully cracked elements remain, because the shear stiffness is kept constant throughout the whole analyses ( $G_{ns} = \beta G$ ). As the horizontal force is equal to the integral of the shear stresses, these extra shear stresses causes an over-stiff response.

The explanation for the fact that shear locking doesn't happen for the completely cracked elements with Sequentially Linear Analysis, can be found in the code. Applying the last damage increment differs from the regular damage algorithm as the last branch from the sawtooth law has a very small normal stiffness,  $10^{-6}E_0$  and shear stiffness,  $10^{-6}G_0$  (not equal to zero as SLA cannot deal with zero stiffness and strength (Van de Graaf, 2017)), to simulate a complete damaged material. Thus, for the fully cracked situation in figure 5.14b and figure 5.14d the shear stiffness is reduced to  $10^{-6}G_0$ , resulting in almost zero additional shear stresses at the bottom.

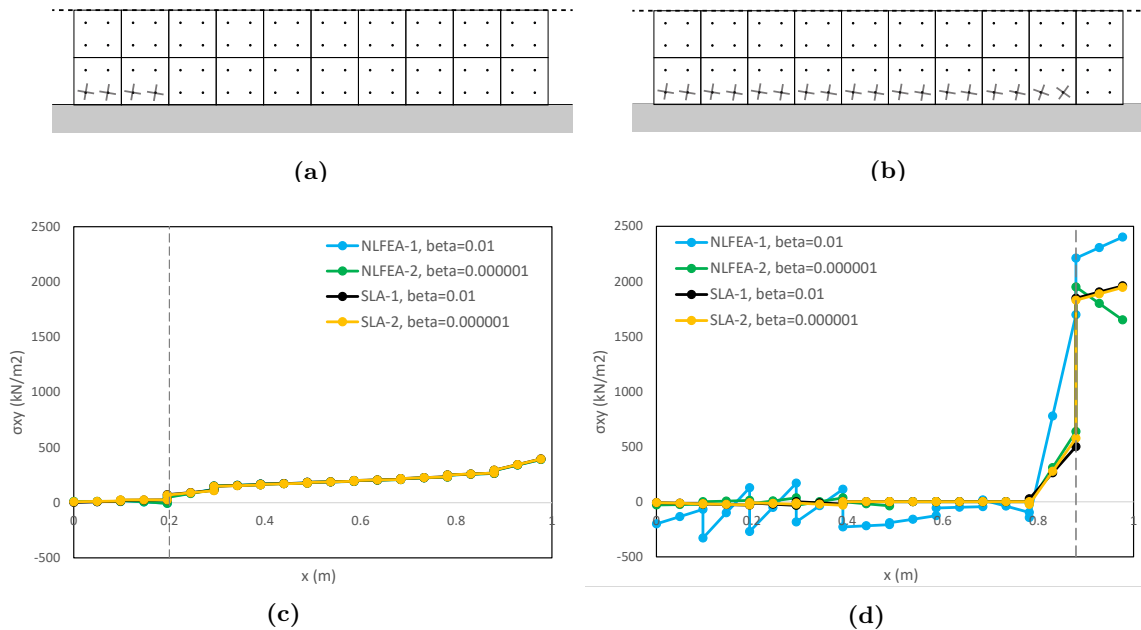


**Figure 5.14:** (a) Damaged state for  $u=0.6$ mm (b) Damaged state for  $u=4.5$ mm (c)  $\sigma_{xy}$  for  $u=0.6$ mm (d)  $\sigma_{xy}$  for  $u=4.5$ mm

### 5.3.3 Poisson's ratio

The second parameter subjected to the variation study is the Poisson's ratio. The analytical calculations in chapter 4, the experimental results and the numerical models in previous subsection showed that failure mainly occurs at the top and bottom of the wall. As the Poisson's ratio influences the direction of the principal stresses, especially at the bottom, it is important to look at the effect of the Poisson's ratio on the failure mode. Figure 5.15 illustrates how the Poisson's ratio effects the direction of the principal stresses.

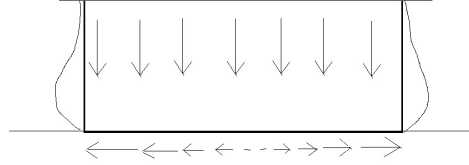


**Figure 5.15:** Influence of Poisson's ratio on principal stresses.

In case of a non-zero Poisson's ratio the wall tends to expand sideways due to the overburden load and self-weight. However, in the numerical model the bottom nodes are fully constrained. This leads to additional shear stresses at the bottom, that cause rotation of the principal directions. These principal directions are important as they determine the direction at which the integration point will fail in the numerical analyses. The Poisson's ratio of the masonry is assumed to be 0.21. Furthermore  $\beta = 10^{-6}$  is applied to avoid the shear locking problems in case of NLFEA.

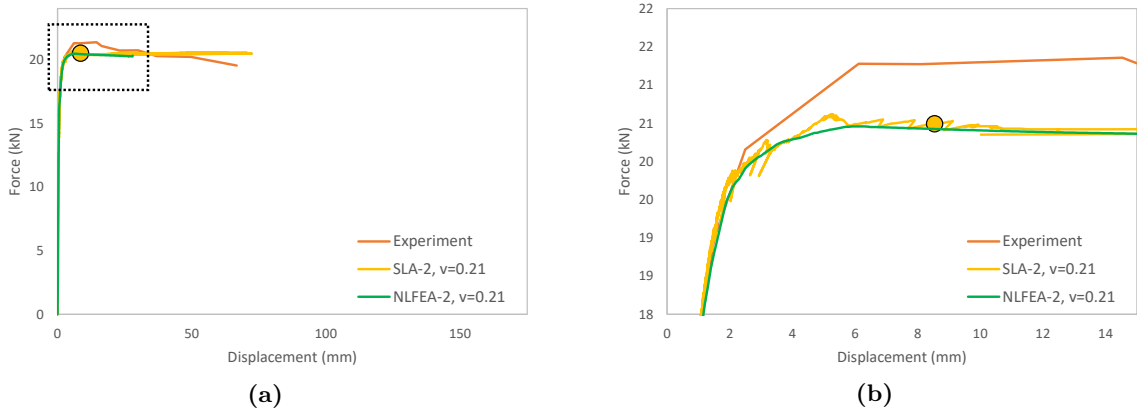


**Figure 5.16:** Force-displacement diagrams for  $\nu = 0.12$  (a) Complete FU-curve (b) Zoom-in close to peak load.

A clear difference can be observed in figure 5.16a between NLFEA and SLA: analysis SLA-2 is way more ductile and simulates the experimental results better compared to NLFEA-2. However, special attention should be given to the way both types of analyses deal with damaged integration points. The material law of undamaged integration points is equal for both NLFEA and SLA and is as follows:

$$\begin{bmatrix} \sigma_{nn} \\ \sigma_{ss} \\ \sigma_{tt} = 0 \\ \sigma_{ns} = \sigma_{sn} \end{bmatrix} = \begin{bmatrix} \frac{E_0}{1 - \nu_0^2} & \frac{\nu_0 E_0}{1 - \nu_0^2} & 0 & 0 \\ \frac{\nu_0 E_0}{1 - \nu_0^2} & \frac{E_0}{1 - \nu_0^2} & 0 & 0 \\ 0 & 0 & 0 & 0 \\ 0 & 0 & 0 & G_0 \end{bmatrix} \begin{bmatrix} \varepsilon_{nn} \\ \varepsilon_{ss} \\ \varepsilon_{tt} \\ \gamma_{ns} \end{bmatrix} \quad (5.1)$$

Where  $G_0 = \frac{E_0}{2(1+\nu_0)}$ .

This material law changes as soon as the integration point exceeds the tensile or compressive strength and differences arise between NLFEA and SLA: for NLFEA the Poisson's ratio is damaged based, in other words, the Poisson's ratio decreases at the same rate as the Young's modulus. The material law becomes:

$$\begin{bmatrix} \sigma_{nn} \\ \sigma_{ss} \\ \sigma_{tt} = 0 \\ \sigma_{ns} = \sigma_{sn} \end{bmatrix} = \begin{bmatrix} \frac{E_{nn}}{1 - \nu_{ns}\nu_{sn}} & \frac{\nu_{sn}E_{nn}}{1 - \nu_{ns}\nu_{sn}} & 0 & 0 \\ \frac{\nu_{ns}E_{ss}}{1 - \nu_{ns}\nu_{sn}} & \frac{E_{ss}}{1 - \nu_{ns}\nu_{sn}} & 0 & 0 \\ 0 & 0 & 0 & 0 \\ 0 & 0 & 0 & \beta G_0 \end{bmatrix} \begin{bmatrix} \varepsilon_{nn} \\ \varepsilon_{ss} \\ \varepsilon_{tt} \\ \gamma_{ns} \end{bmatrix} \quad (5.2)$$

Where  $E_{\_\_\_}$  and  $\nu_{\_\_\_}$  refer to the damaged Young's modulus and Poisson's ratio respectively. However, in the current SLA code the Poisson's ratio abruptly drops to 0 as soon as the integration point is damaged for the first time:

$$\begin{bmatrix} \sigma_{nn} \\ \sigma_{ss} \\ \sigma_{tt} = 0 \\ \sigma_{ns} = \sigma_{sn} \end{bmatrix} = \begin{bmatrix} E_{nn} & 0 & 0 & 0 \\ 0 & E_{ss} & 0 & 0 \\ 0 & 0 & 0 & 0 \\ 0 & 0 & 0 & \beta G_0 \end{bmatrix} \begin{bmatrix} \varepsilon_{nn} \\ \varepsilon_{ss} \\ \varepsilon_{tt} \\ \gamma_{ns} \end{bmatrix} \quad (5.3)$$

Due to this difference in the implementation of the Poisson's ratio, the comparison between NLFEA and SLA is not valid. At the time of writing this thesis the SLA implementation in DIANA is still under development and the use of the damaged-based Poisson's ratio is currently getting tested.

To still be able to compare these different types of analyses the initial Poisson's ratio ( $\nu_0$ ) is set to 0 for both numerical methods to elude the effect of different damage strategies between the methods. Figure 5.17a illustrates the capacity curves of analysis SLA-3 and NLFEA-3 where  $\nu = 0$  and  $\beta = 10^{-6}$  and a few observations can be made. First, it turns out that the Poisson's ratio has a big influence on the ductility of the wall. This becomes clear when the capacity curves, using a non-zero Poisson's ratio, are compared with the capacity curves where a zero Poisson's ratio is used. SLA-3 reaches a displacement which is twice as much compared to the displacement of SLA-2. Second, whereas in model SLA-2 the second stop criterion is governing (decrease of  $\lambda_{ini}$ ), in model SLA-3 the first one is governing (exceedance of number of sawteeth (in tension)). Third, the difference between NLFEA and SLA with respect to the horizontal displacement at the top of the wall is most severe in case of a zero Poisson's ratio: model NLFEA-3 runs into non-convergence problems relatively soon whereas model SLA-3 is able to reach a displacement of 153 mm.

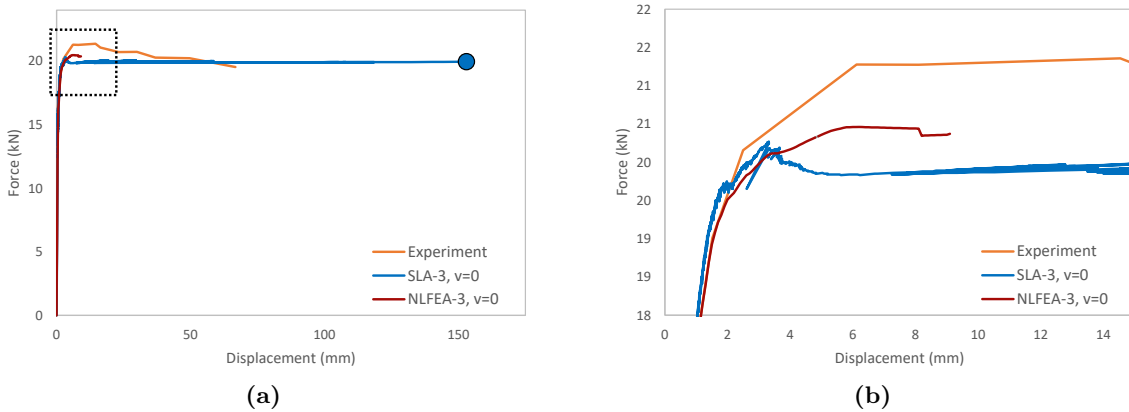


**Figure 5.17:** Force-displacement diagrams for  $\nu = 0$  (a) Complete FU-curve (b) Zoom-in close to peak load.

Besides the base shear stresses and thus the base shear force, also normal stresses are analysed at the bottom of the wall, which gives information about the tensile and compressive stress. Figure 5.18a demonstrates the normal stresses at the bottom of the wall when  $u = 4.5$  mm. Again, the fully cracked elements (up to the dashed line) can be identified as the normal stresses are close to zero. The uncracked elements (at the right of the dashed line) are loaded in compression. The input compressive strength was 10 MPa and indeed this strength isn't exceeding, according to figure 5.18a. Figure 5.18b shows the strain in normal direction and no remarkable differences are observed, meaning that the crack widths for all analyses are almost equal.

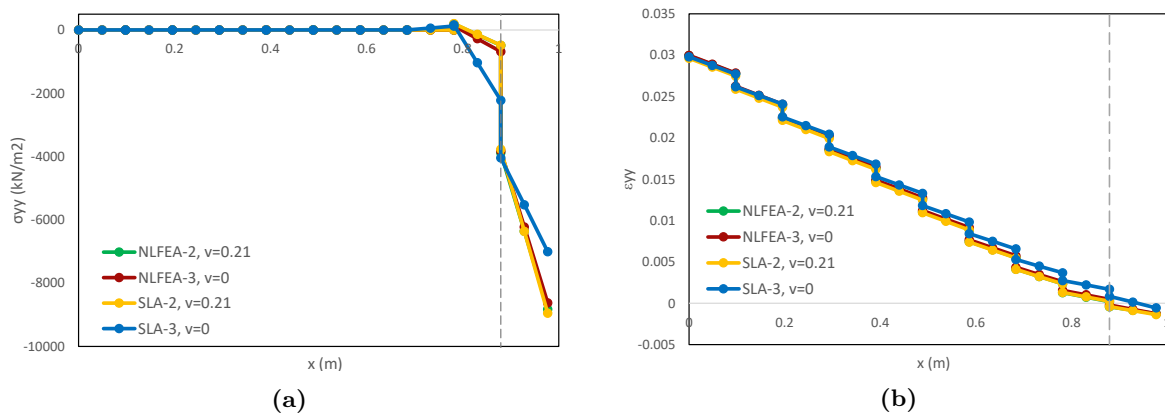


Figure 5.18: (a)  $\sigma_{yy}$  for  $u=4.5$  mm (b)  $\epsilon_{yy}$  for  $u=4.5$  mm

### 5.3.4 Crack model

Up to now the 'fixed smeared crack model' is applied for the Sequentially Linear Analysis and the Non-linear Finite Element Analysis. With this approach, the crack direction in the integration point is fixed as soon as the stress in the integration point exceeds the tensile or compressive strength. This approach fits nature as in real life a crack also has a fixed crack plane. However, there is a constant shear retention  $\beta$  that, after cracking, is responsible for rotation of the principal stresses, which means a misalignment between the principal stresses and the principal strains (Rots and Blaauwendraad, 1989). Another approach is the 'rotating smeared crack concept'. This approach has a unique shear term that enforces co-axiality between the principal strains and principal stresses. Another difference with the fixed smeared crack model is that it doesn't need to keep permanent track of the damage orientation. This implies that inactive defects from previous stage of loading cannot be re-activated, which could have consequences in case non-proportional loading (Rots and Blaauwendraad, 1989).

To investigate the effect of the type of crack model on the capacity of the shear wall, two variations are imposed, the first one (model NLFEA-4) involves the rotating smeared crack concept. The second one (model NLFEA-5) is based on the fixed smeared crack approach but has a damaged based shear retention factor ( $\beta$ ) instead of a constant based shear retention factor. In other words,  $\beta$  decreases with the same rate as the Young's modulus. As SLA is based on the fixed crack approach and the damage based shear retention factor is not available in SLA yet, the variation study in the subsection only applies to NLFEA.

In figure 5.19 it becomes clear that the analysis NLFEA-5 ( $\beta =$  damage based) already terminates when a displacement of  $u=2.8$ mm is reached. It is assumed that non-convergence plays a role in this model. The rotating crack model, NLFEA-4, however does lead to sufficient deformation capacity as a displacement of 40.30 mm is reached. In figure 5.20 the shear stress at the bottom of the wall are analysed. At that moment the top of the wall is displaced only  $u=2.8$  mm, because analysis NLFEA-5 doesn't go any further. Again, it can be observed that the crack is not fully developed yet as the crack goes up to  $x=0.8$  mm (see dashed line). The cracked element can again be identified as the shear

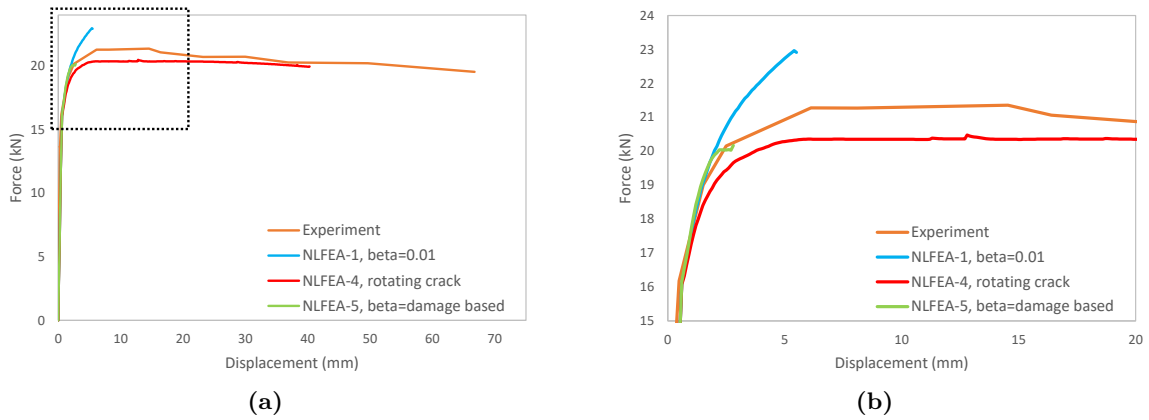


**Figure 5.19:** Force-displacement diagrams for different crack models (a) Complete FU-curve (b) Zoom-in close to peak load.

stresses are (close to) zero. As a reference, results from model SLA-1 with a constant shear retention factor ( $\beta = 0.01$ ) are plotted as well. Whereas NLFEA-1 shows shear locking, models NLFEA-4 and NLFEA-5 with a rotating crack model and a fixed crack model with a damaged based shear retention factor respectively, don't suffer from these shear locking problems. Model SLA-1, which does have the same (constant) retention factor as NLFEA-1, corresponds very well with NLFEA-4 and NLFEA-5 with respect to the shear stresses. The reason why SLA doesn't come with shear locking is explained in the previous subsection: the last sawtooth law has a stiffness close to zero, which prevents having remaining shear stresses.

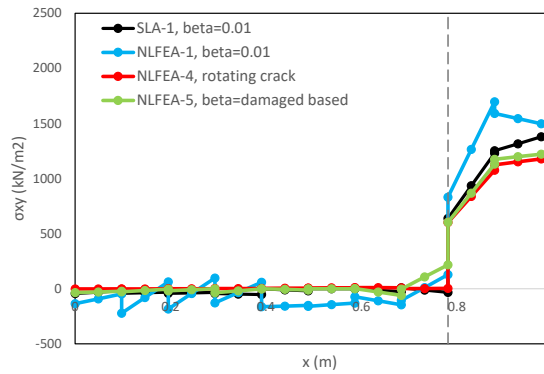


**Figure 5.20:**  $\sigma_{xy}$  for  $u=2.8\text{mm}$

## 5.4 Shell elements

In this subsection, the plane stress elements are replaced by shell elements. The difference with plane stress elements is the fact that shell elements do allow out-of-plane deformations. There are 40 degrees of freedom instead of 16, because the nodes also have out-of-plane rotational and translational degrees of freedom. Furthermore, there are at least 3 integration points over the thickness instead of 1. The thickness integration scheme used, is the (default) 3-point Simpson integration scheme. As the variation studies in previous subsection showed shear locking for NLFEA if the shear retention factor is equal to 0.01, in this section a shear retention factor  $\beta = 10^{-6}$  is applied for both SLA and NLFEA.

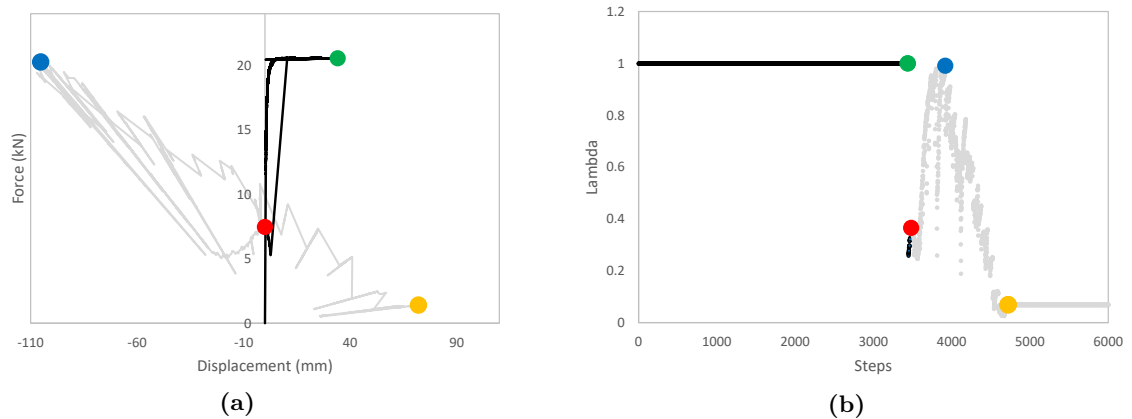


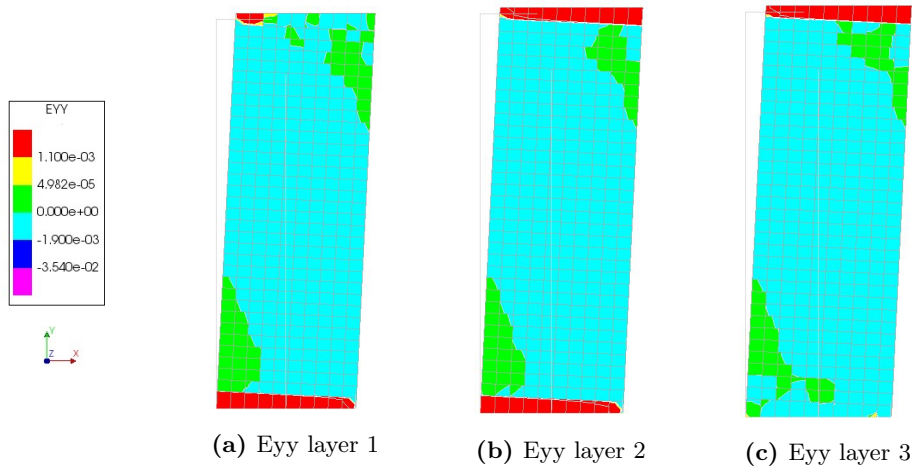
Figure 5.21: (a) Force-displacement graph (b) Initial load multiplier graph ( $\lambda_{ini}$ ).

Table 5.7: Events per load step.

	Load step	Event
●	3439	Maximum displacement is reached
●	3482	Displacement is about to become negative
●	3918	$\lambda_{ini}$ is not able to return back to 1
●	4721	Number of damage increments exceeds number of sawteeth in tension

The capacity curve of the Sequentially Linear Analysis is plotted in figure 5.21a. To decide on the last step of the analysis, the results are analysed based on the stop criteria defined in section 5.3.1. The first stop criterion states that a step is assumed to be the last one as soon as the number of damage increments exceeds the number of sawteeth. This happens at step 4721. However, the displacement of the pier becomes negative before that step already. Applying a positive force and obtaining a negative displacement is physically not possible and therefore this stop criterion is disregarded. The second stop criterion states that a step is assumed to be the last one as soon as the initial load multiplier ( $\lambda_{ini}$ ) corresponding to this step is not able to return back to 1. In this model, this happens at step 3918, however, also this step comes with a negative displacement. Therefore, also this stop criterion is disregarded. The third one is governing as soon as the displacement is more than 977, which is not the case, thus also the last stop criterion is not governing.

Apparently, the predefined stop criteria are not sufficient for this model and for now step 3482 (red dot) is assumed to be the last step, because that step is the last one before negative displacements occur. The possible reason why none of these stop criteria are sufficient, becomes clear in figure 5.22. Here the strains in y-direction are plotted for every thickness layer. In figure 5.22c no damage at the bottom is observed, whereas the bottom in the other two layers is damaged. This means, the wall



**Figure 5.22:**  $\varepsilon_{yy}$  at step 3400: (a) Layer 1 (b) Layer 2 (c) Layer 3

behaves in an asymmetric manner with respect to the thickness, which leads to out-of-plane behaviour of the pier. To apply a damage increment, the algorithm has to pick one integration point, even though the 3 integration points over the thickness should fail at the same time in case of in-plane loading. At some point, one of the outer integration points is the critical one and the stiffness of that integration point is reduced, resulting in an asymmetric wall. In other words, one layer has a different stiffness and strength than the other layers. Even though the maximum displacement in z-direction is only 4.9 mm at step 3331, this is still 14.4 % of the total horizontal displacement at the top of the pier, which is 34.0 mm.

In figure 5.24 the comparison between plane stress elements and shell elements is made, where in figure 5.24a the comparison is related to SLA and in 5.24b related to NLFEA. For SLA the difference between the capacity curve for plane stress elements and shell elements is significant. The model with plane stress elements simulates the experimental curve well with respect to peak load and total displacement, but the model with shell elements only reaches half of that displacement. This can be attributed to the out-of-plane behaviour of the wall. To verify this statement again a model is built with shell elements, however all nodes are fixed in out-of-plane direction (see appendix). These

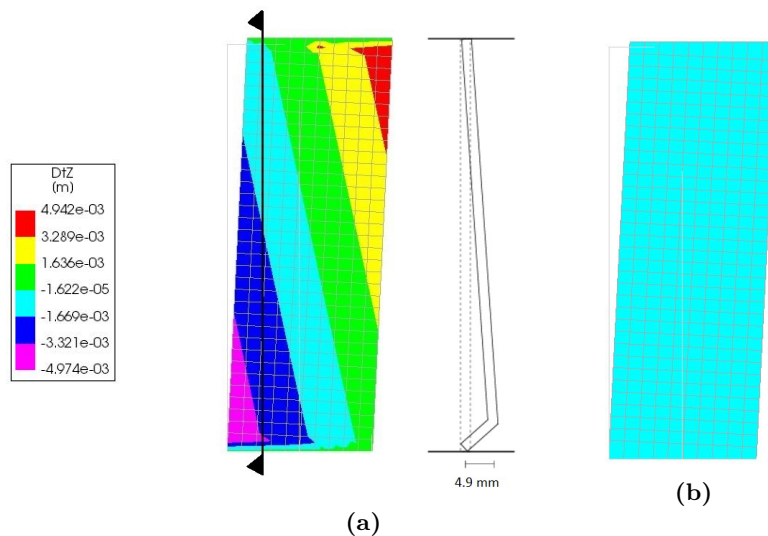


**Figure 5.23:** Out-of-plane displacement (a) SLA at step 3331 (b) NLFEA at every step

results showed no out-of-plane behaviour and the capacity curve corresponds with the capacity curve of the model with plane stress elements. Besides, the stop criteria were sufficient and the second stop criterion was governing.

Another difference between the use of plane stress elements and shell elements is related to the calculation time. In case of shell elements the calculation time was about 14 times longer compared to the model with plane stress elements. Using shell elements means extra integration points over the thickness. Each step within the analysis takes more time, because the  $\lambda_{ini}$  has to be calculated for more integration points and the total required steps is more, since more integration points gets damaged.

With respect to NLFEA the results of the model with plane stress elements and shell elements are identical as the capacity curves overlap. This observation can also be supported by figure 5.23b: there's no out-of-plane displacement, meaning that the shell elements behaved similar as plane stress elements, where no out-of-plane behaviour is possible.

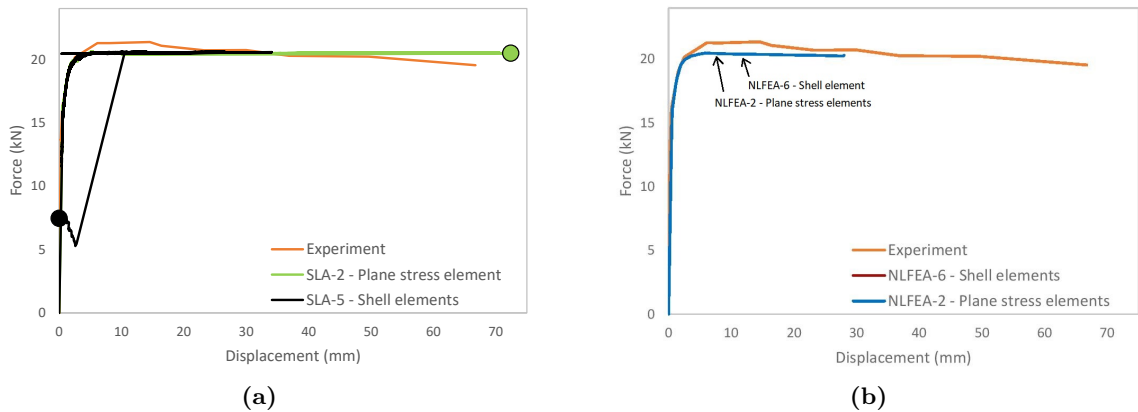


**Figure 5.24:** Comparison between type of elements (a) using SLA (b) using NLFEA.

## 5.5 Conclusions

In this chapter the shear wall was modelled using the smeared crack approach. First, stop criteria were defined, where after the influence of different parameters was investigated. The following conclusions can be drawn from this chapter:

### General

- When the current SLA implementation in Diana 10.2 is used, adequate stop criteria are required, until the errors in the code are found and corrected. Without the stop criteria, analyses could pick an integration point as the critical one infinite times, whereby the analyses runs indefinitely. The stop criteria also prevented negative displacements in case of a positive applied force on top of the shear wall, which is physically impossible.
- The initial value for the Poisson's ratio influenced the ductility of the pier, but a damage-based Poisson's ratio should be implemented in the SLA code in order to correctly compare the influence of the Poisson's ratio on the capacity of the wall, between SLA and NLFEA as the damage strategies for the Poisson's ratio differ.

### Numerical models versus experiment

- The numerical models are able to reproduce the crack pattern in the experiment until total collapse. In the experiment a vertical crack did arise suddenly, which resulted in a drop of the base shear force capacity. In the numerical models this phenomenon is not observed and the analyses don't stop due to a sudden drop of the base shear force, but due to non-convergence issues in case of NLFEA and due to the defined stop criteria in case of SLA.

### NLFEA versus SLA

- Shear locking occurred for NLFEA when  $\beta$  is too high ( $\beta = 0.01$ ). A solution would be to use a  $\beta$  close to zero ( $\beta = 10^{-6}$ ) or to use the rotating crack approach instead of the fixed crack approach.
- SLA doesn't encounter shear locking issues (even though the code is currently based on the fixed crack approach), due to last branch in the sawtooth law, which has a  $\beta$  of  $10^{-6}$ . It is a good alternative for NLFEA when it comes to obtaining numerically stable results. Whereas NLFEA mainly found converged solutions using the rotating crack approach or using the fixed crack approach with a  $\beta$  close to zero, SLA found stable solutions regardless of the  $\beta$ -factor being used.

### Plane stress elements versus shell elements

- The stop criteria are not sufficient for the model with shell elements. This can most likely be attributed to the out-of-plane behaviour, which occurred even though the wall was loaded in-plane.
- The use of shell elements significantly increases the calculation time. Shell elements have multiple integration points with respect to the thickness and as only one integration point per analysis step gets damaged, the total analysis takes more time.
- The use of shell elements reduces the deformation capacity as the maximum displacement decreased by 50% when the plane stress elements were replaced by shell elements.

# 6. Shear wall: discrete crack approach

This chapter will elaborate on the discrete crack approach, also known as the meso-modelling approach and the chapter is divided into three sections. The first section explains how the numerical model is built. The model differs from the model with the macro-modelling approach, because interface elements are used to account for the mortar between the CaSi-elements. Plane stress elements in combination with interface elements are applied in section 2. As explained in previous chapters, plane stress elements are sufficient to model in-plane behaviour. However, if this in-plane component is part of a 3D configuration, mostly shell elements are used. Section 3 focusses on the application of shell elements in combination with interface elements. The chapter ends with a conclusion in section 4.

## 6.1 Finite element model

### 6.1.1 FEM model and material properties

The numerical model of the *TUD\_COMP* – 24 experiment using the meso-modelling approach is illustrated in figure 6.1a. The dimensions are equal to the model in previous section: the width is 0.977 m, the height is 2.744 m, the thickness is 0.1 m and the overburden load is 0.6 MPa. With the meso-modelling approach a distinction is made between mortar and bricks. The parameters used for these materials are listed in table 6.1 and table 6.2. These values are based on Nederlands Normalisatie Instituut (2017), Esposito and Ravenshorst (2017) and Ng'andu (2006).

**Table 6.1:** Properties CaSi-bricks for meso-modelling approach

	CaSi-bricks (unit)		
Elasticity	$\rho = 1824 \text{ kg/m}^3$	$E_0 = 8800 \text{ MPa}$	$\nu = 0.21$
Tensile failure	$f_t = 4.0 \text{ MPa}$	$G_{ft} = 4000 \text{ J/m}^2$	
Compressive failure	$f_c = 10 \text{ MPa}$	$G_{fc} = 20000 \text{ J/m}^2$	
Sawtooth parameters	$\beta = 0.01$	$p_{fac} = 0.1$	

**Table 6.2:** Properties interface elements for meso-modelling approach

	Mortar (interface element)	
Elasticity	$k_n = 867 \text{ N/mm}^3$	$k_t = 361 \text{ N/mm}^3$
Tensile failure	$f_t = 0.4 \text{ MPa}$	$\varepsilon_{ult} = 0.00010692$
Compressive failure	Linear elastic	
Sawtooth parameters	$\beta = 0.01$	$p_{fac} = 0.1$

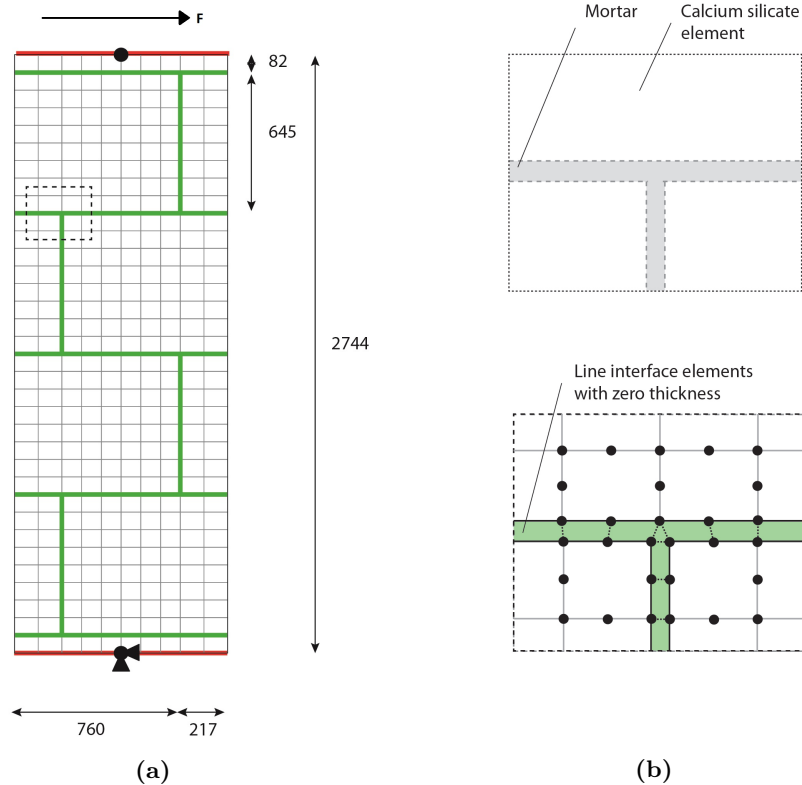


**Figure 6.1:** (a) Model with meso-modelling approach (b) Top: detail of pier. Bottom: detail of the numerical model.

An important remark about the material properties has to be made: the current SLA code for interface elements doesn't contain a Coulomb Friction model yet. Furthermore, the discrete crack model for the interfaces only contains tensile failure. Compressive failure in the interface elements would require a corresponding constitutive model which is not a feature in SLA yet. Compressive non-linearity is therefore only provided in the continuum elements. Thus, this model contains both discrete cracking (in the interface elements) and smeared cracking and crushing (in the continuum elements).

In the model again eight-node quadratic elements with a mesh size of approximately  $0.1 \times 0.08 \text{ m}^2$  are applied. In case of the plane stress elements the elements type is again CQ16M and in case of shell elements the element type is CQ40S (see section 2.4.2 for the element descriptions). Similar

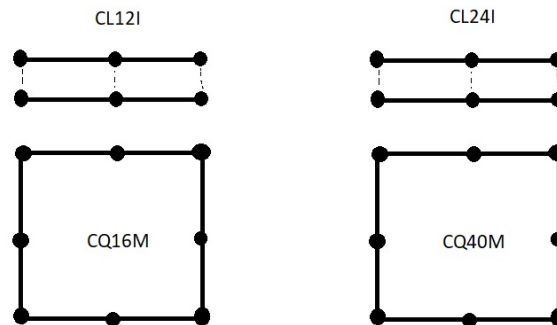


**Figure 6.2:** Left: compatible elements in a 2D configuration. Right: compatible elements in a 3D configuration

to the macro-modelling approach, the integration scheme is the 2x2 Gauss integration scheme for both plane stress elements and shell elements. The type of interface elements being used depends on the adjacent continuum elements. The interface element which is combined with quadrilateral plane stress elements is the CL12I element (see figure 6.2). All 6 nodes of this element have a translational degree of freedom in x- and y-direction. The interface elements which is connected to a curved shell element, is the CL24I interface elements. Each node has three translational degrees of freedom and 1 rotational degree of freedom. Similar to the curved shell element, this interface element also has integration points over the thickness and a 3-point Simpson integration scheme is used as well.

### 6.1.2 Properties and stop criteria SLA

With the distinction between mortar and bricks, new sawtooth laws have to be defined, based on the material properties. With a p-factor of 0.1, the fracture energy, compressive strength and tensile strength given in table 6.1 and table 6.2, the sawtooth laws for the continuum elements contain 20 sawteeth in compression and in tension. The sawtooth law for the interface element contains 28 sawteeth in tension and has linear elastic properties in case of compression. The new stop criteria are similar to the ones defined in chapter 5.

A step of an analysis is the last one as soon as:

1. The number of damage increments exceeds the number of sawteeth for any integration point in the model. For the interface elements this means an exceedance of 28 damage increments in tension. For the continuum elements this means either:
  - (a) 20 x tension + 20 x tension = 40 damage increments in tension, or
  - (b) 20 x tension + 22 x compression, or
  - (c) 22 x compression + 22 x compression = 44 damage increments in compression
2. A step of an analysis is the last one as soon as  $\lambda_{imi}$  is not able to return back to 1.0.
3. The displacement gets bigger than 977 mm.

### 6.1.3 Properties NLFEA

The additional input with respect to the NLFEA is again related to the convergence criteria and the iteration scheme. This input is similar to the one in chapter 5: the convergence tolerance is set to  $10^{-4}$ , the Modified NR iteration scheme is used (see section 2.1.3 for non-linear numerical methods) and the maximum number of iteration steps is set to 250.

## 6.2 Plane stress elements

As the numerical model is asymmetric, the results are expected to be different as soon as the horizontal load is applied in the opposite direction. Therefore in the first subsection the model will be loaded with the original load and in the second subsection the model is loaded with a horizontal load in opposite direction.

### 6.2.1 Original load

With the material properties and sawtooth laws defined in previous subsection, the analysis is completed and the results of the entire SLA analysis is depicted in figure 6.3a. Again the results are analysed to find the last step according to the defined stop criteria. In figure 6.4 the damaged integration points in the upper left corner and in the bottom right corner are shown for three analysis steps. At step 1440 the damage is located in the interface elements only. We can see the crack developing as the red dots indicate a fully cracked integration point and the pink dots indicate partially cracked integration points. At step 1650 some integration points in the continuum elements are damaged as well. As stated before, the current SLA code is not provided with compressive failure in the interface elements, therefore the compressive non-linearity is assigned to the continuum elements. At this step toe crushing is initiated, but the integration points still have some capacity left. However, in this step the initial load multiplier ( $\lambda_{ini}$ ) starts decreasing and thus stop criterion 2 is met. The results are analysed even further to observe the damage state if the analysis would continue. In step 1670 at the top left corner almost all integration points in the interface element are damaged in tension except for two. As the interface element cannot fail in compression, the continuum elements account this type of failure, which can be observed from the picture as one continuum element is completely damaged in compression. Even though this damaged state looks correct, at this step the initial load multiplier is almost zero, meaning that no pre-compression and self-weight is present in the model, which could lead to an incorrect stress redistribution. Therefore, step 1650 is assumed to be the last step in the analysis and it's marked with a dot in figure 6.3a and 6.3b.

The deformed shape and the interface tractions are depicted in figure 6.5a. The interface element opens up after the tensile strength is exceeded, which simulate a real crack as a discontinuity in the model. In figure 6.5b the capacity curve of the SLA analysis is shown together with the capacity curve of the NLFEA and the one from the experiment and a few observations can be made. First, the results of both numerical analyses are very similar to the experimental results, contrary to the smeared crack model in section 5.3. Second, even though a shear retention factor ( $\beta$ ) of 0.01 is used, no shear locking occurred for the NLFEA as we observe no over-stiff response in the force-displacement graph. This

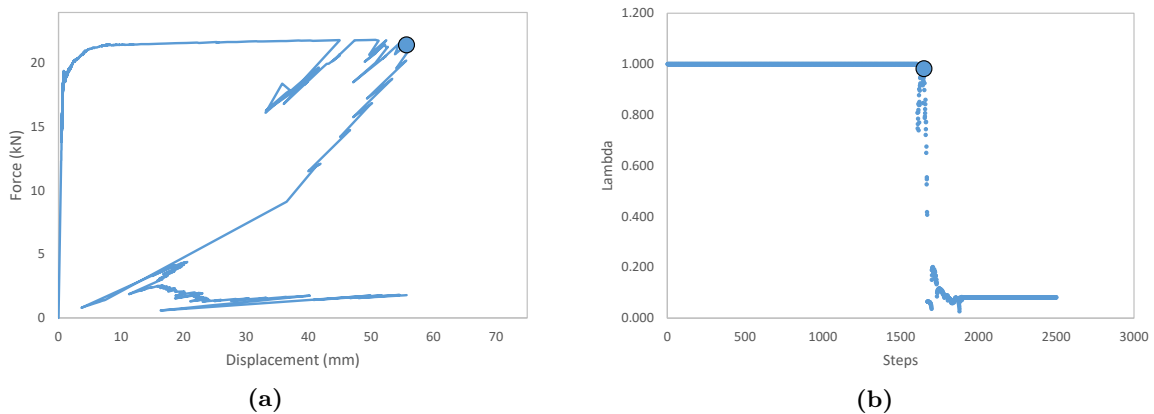


**Figure 6.3:** (a) Capacity curve of the complete SLA. The final step is marked with a dot (b)  $\lambda_{ini}$  The final step is marked with a dot.

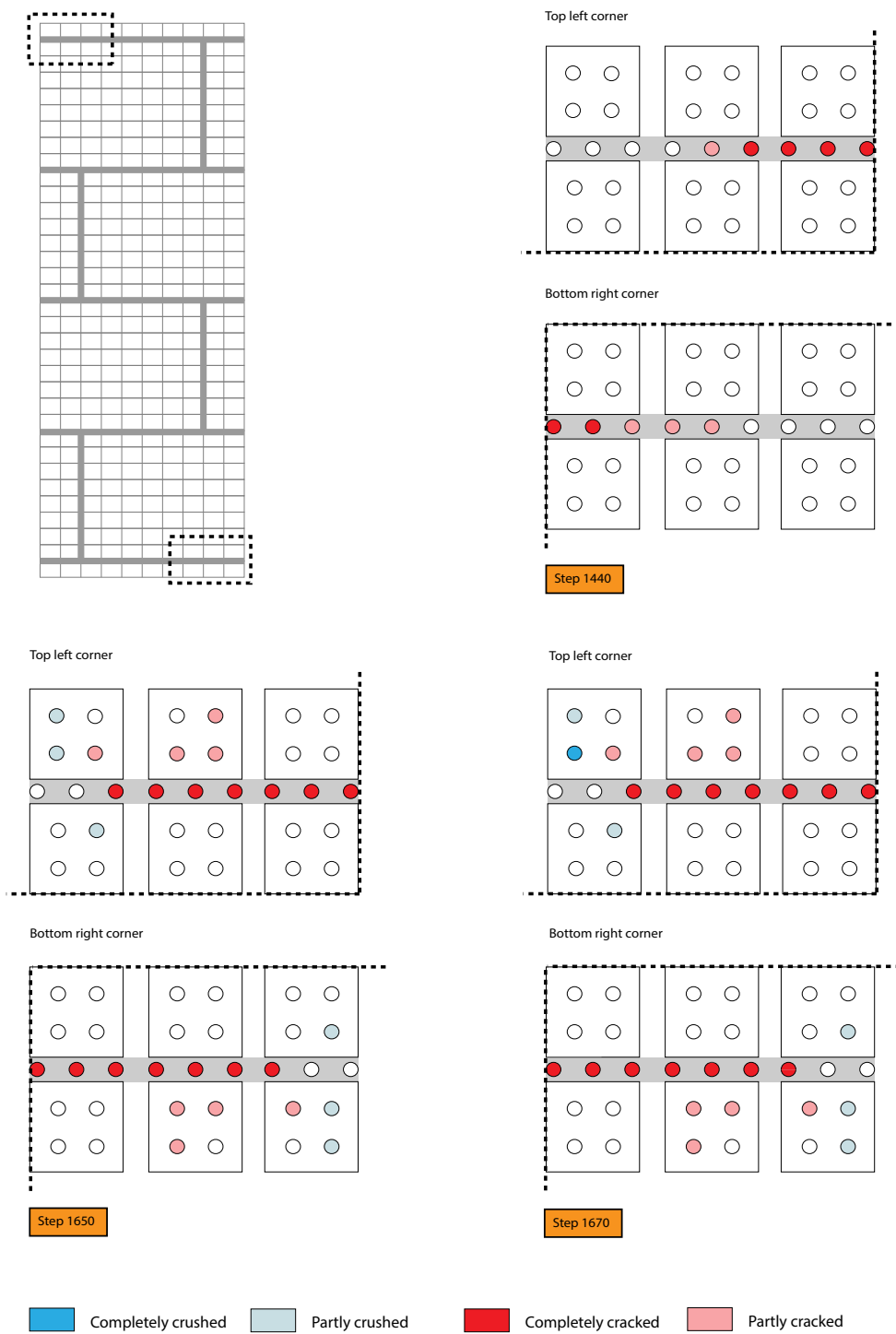
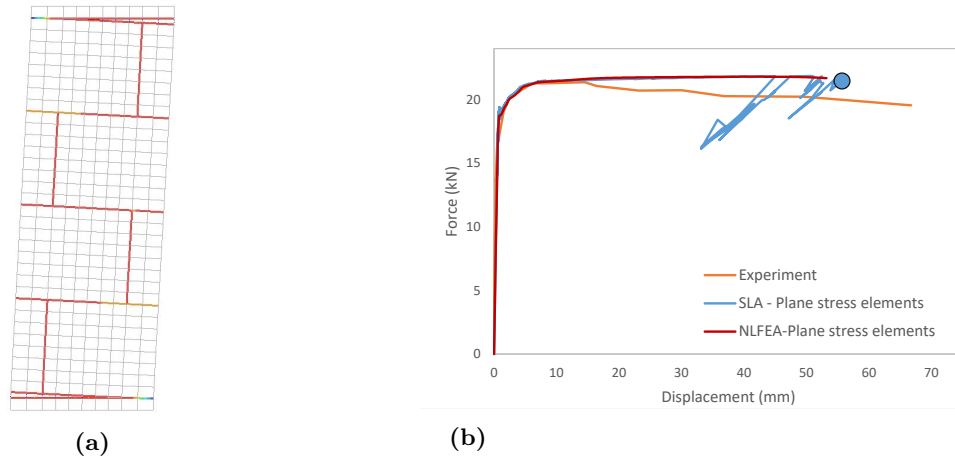


Figure 6.4: Damage increments at bottom right and top left corner of the wall at step 1440, 1650 and 1670.



**Figure 6.5:** (a) Deformed shape (b) Capacity curve of SLA, NLFEA and experiment

can be explained by the fact that the interface elements cause a discontinuity in the model. Figure 5.12 in chapter 5 showed that one element got extra shear stresses, due to displacement continuity when the adjacent element was subjected to tensile straining. The use of interface elements makes it possible to separate continuum elements. The shear stresses at both sides of the interface/crack are therefore reduced to zero, which prevents the adjacent elements from stress locking.

In figure 6.6 crushing and crack opening of the elements are compared with those in the experiment. On the left, the crack opening at the bottom is plotted on the y-axis and the horizontal displacement at the top of the wall on the x-axis. It becomes clear that the crack opening of the numerical model corresponds well with the experimental results: the crack opens up as the horizontal top displacement increases. Crushing of the numerical model, however, differs from the experiment. Whereas the numerical model shows the expected result, namely more crushing (negative displacement) as the top displacement increases, the experiment shows a positive displacement at the final two measured points. This could possibly be explained by the fact that out-of-plane rotation occurred in the experiment, which caused a misalignment between the wall and the kicker course.

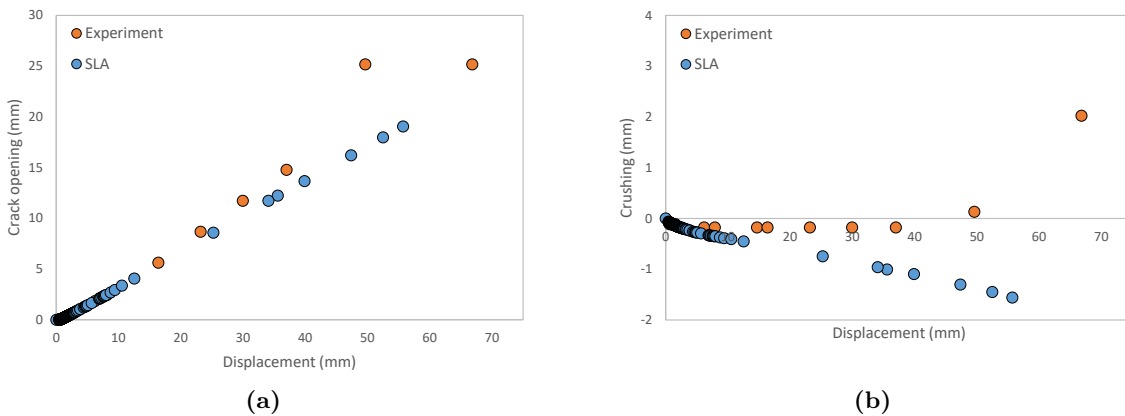


**Figure 6.6:** (a) Crack opening at the bottom (b) Crushing at the bottom.

### 6.2.2 Reversed load

As a variation of the previous model, the same model is used but a reversed horizontal load is applied. As the numerical model is asymmetric, differences in the results are expected.

Again the second stop criterion is governing and the FU-curve is plotted in figure 6.7a together with the results of the previous model. The main difference is the fact that the model with a reversed load fails at an earlier stage compared to the original model. The probable cause becomes clear in figure 6.8 where again the damage is illustrated at three different steps of the analysis.

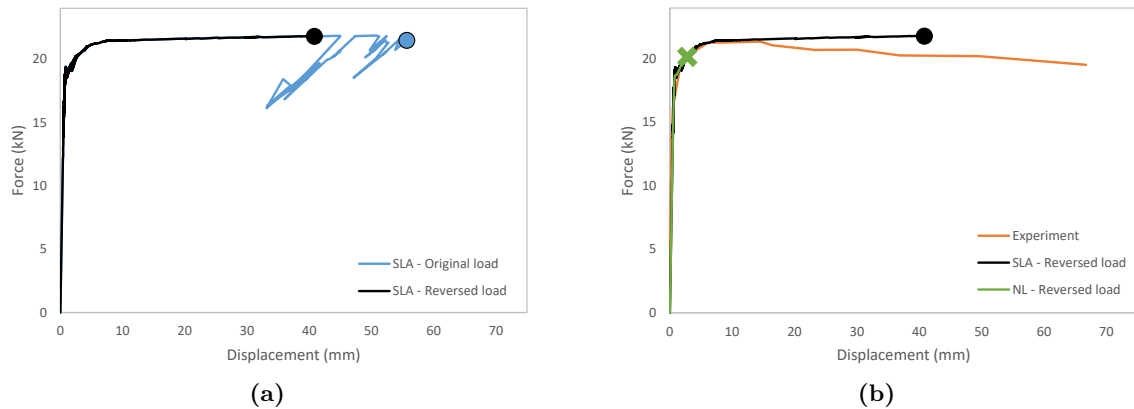


**Figure 6.7:** (a) Comparison of capacity curves of the model with a reversed load and the original load (b) Comparison of capacity curves of the model with a reversed load using SLA and NLFEA.

The first step is again step 1440. Where the original model only showed damage increments in the horizontal interfaces, this model is slightly damaged in the vertical interface elements in both top right and bottom left corner. The second step is step 1636 where stop criterion 2 is met:  $\lambda_{ini}$  starts degrading and toe crushing of some integration points in the continuum elements has started (marked in light blue). The third step which is highlighted in figure 6.8 is step 1679: the bottom is completely damaged as one integration point in the continuum is fully crushed in compression and the adjacent integration points in the interface elements are fully damaged in tension. However, as stop criterion 2 is met already, steps after 1636 will be disregarded.

Also a non-linear analysis is performed (see figure 6.7b). This analysis doesn't converge at an early stage already. As the model doesn't show physical instability yet, the non-convergence occurs due to numerical problems. At the last converged step, a displacement of 2.8 mm is reached and at that stage the first damage increments in the *vertical* interface element are applied. This could be a possible explanation for the non-convergence of the non-linear analysis: cracking in the vertical interface elements gives extra potential crack locations which makes it for the numerical software more difficult to determine the right equilibrium path.

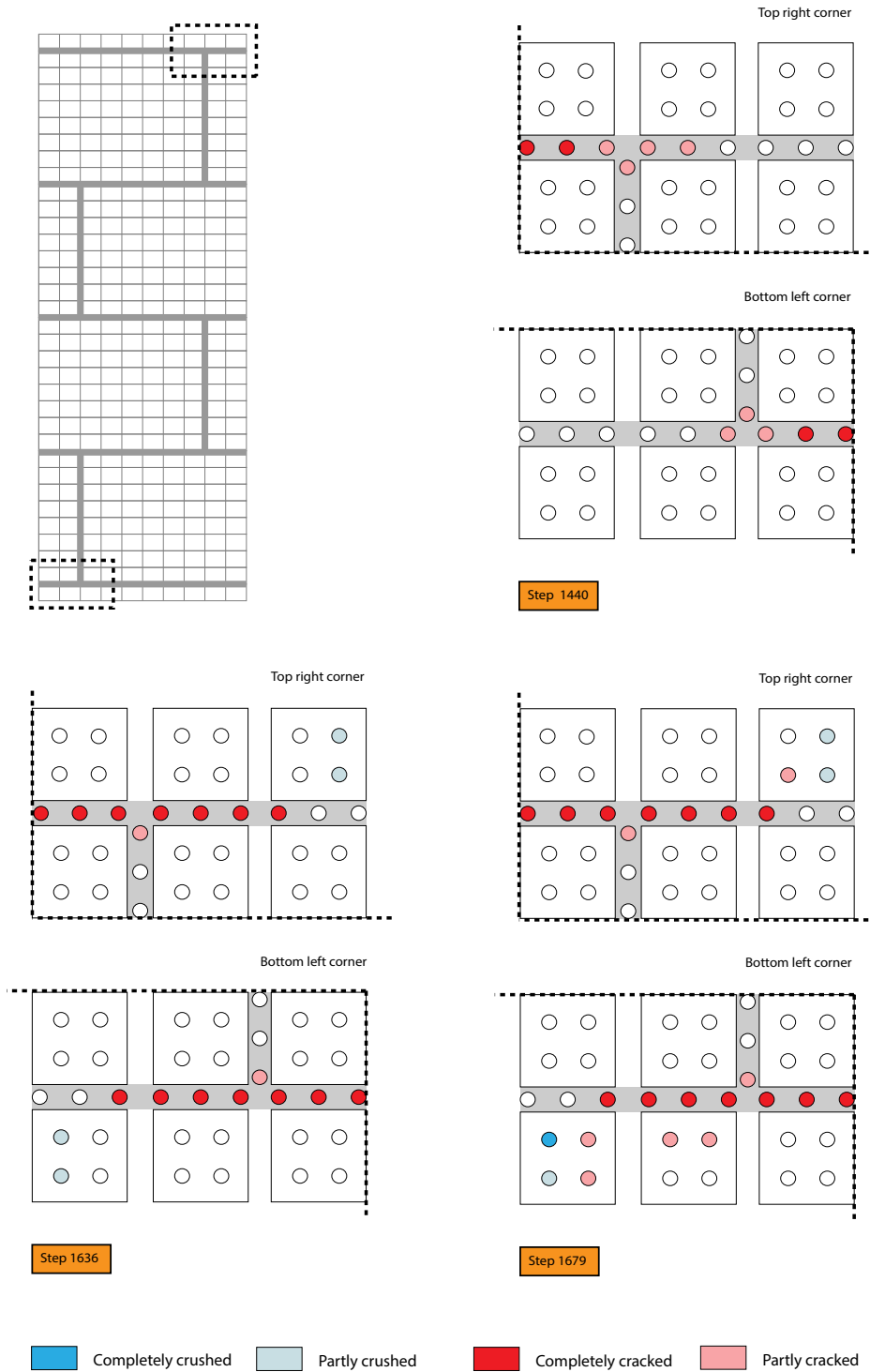
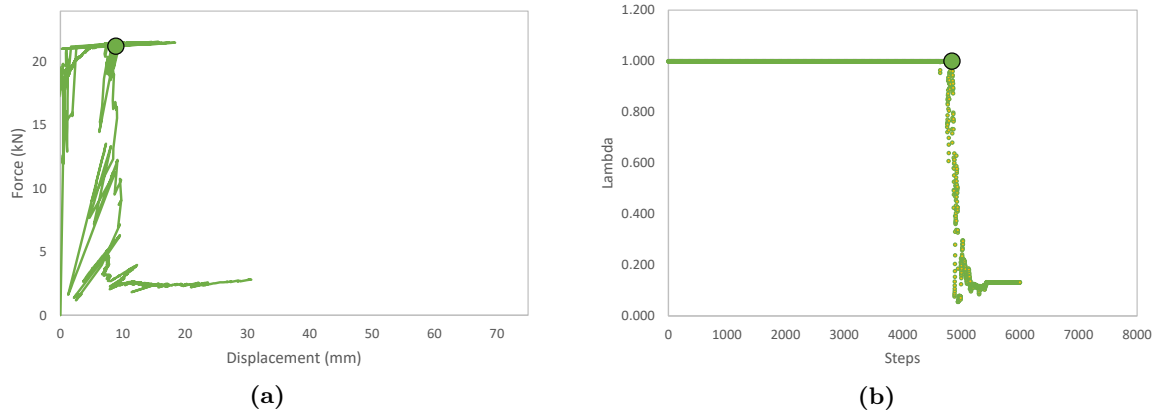


Figure 6.8: Damage increments at bottom left and top right corner of the wall at step 1440, 1636 and 1679.

### 6.3 Shell elements

In order to verify the SLA code for shell elements and to study the influence of the type of element used, the plane stress elements are replaced by shell elements. Figure 6.9a shows the complete capacity curve using SLA and figure 6.9b shows the initial load multiplier graph. The second stop criterion is the governing one, because at step 4844,  $\lambda_{ini}$  drops from 1 to 0.1.



**Figure 6.9:** (a) Capacity curve of the complete SLA analysis. The final step is marked with a dot (b)  $\lambda_{ini}$  with final step marked with a dot.

When the capacity curve of SLA is compared with the curve of NLFEA and a difference can be observed with respect to the ductility of the shear wall (figure 6.10a). In all previous cases, the models with a SLA analysis were always able to displace further than the models with a NLFEA analysis. However in this model the displacement in case of SLA is only 30% of the displacement performing a NLFEA analysis.

When the results above, using shell elements, are compared with the results from previous chapter, using plane stress elements, also a difference can be observed with respect to the ductility. In the previous chapter a reduction of the ductility of 50% was observed when shell elements were used. This also happens here, but the reduction is approximately 70% (see figure 6.10b). In previous chapter the cause was found in the fact that SLA has to pick 1 critical integration point at the time, which causes an asymmetric wall with respect to the thickness. In figure 6.11a the same is observed, however the maximum out-of-plane behaviour is only 0.06 mm, which is significantly less compared to the maximum

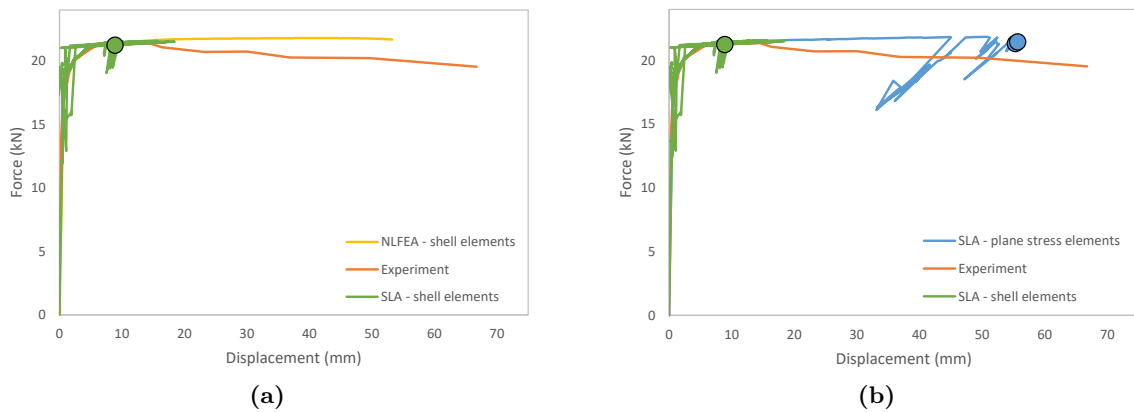


**Figure 6.10:** Comparison capacity curve between (a) Type of analysis (b) Type of elements.

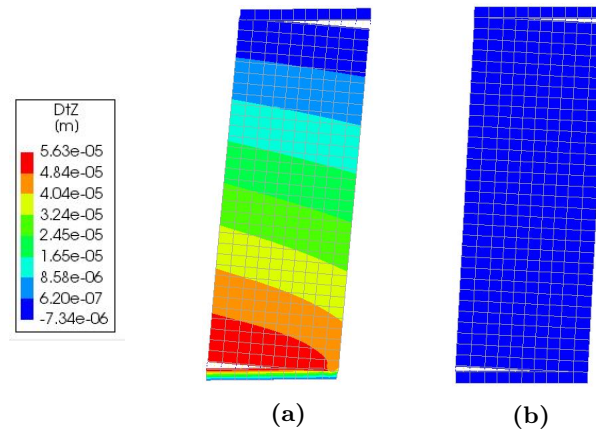


**Figure 6.11:** Out-of-plane displacement of SLA at the last step (step 4844) (a) NLFEA at the last step

out-of-plane displacement found in previous chapter for the smeared crack model, which was 5.0 mm. The out-of-plane displacement for the discrete crack model is zero as soon as all 3 integration points in thickness direction in the interface elements are damaged. The main out-of-plane behaviour occurs when damage increments are applied in the continuum element in upper left and bottom right corner. In contrary to the smeared crack model in previous chapter, the damage of the individual thickness layers in this model doesn't vary a lot. The damage in the shell elements in the bottom right corner only differ slightly (see figure 6.12). For the NLFEA the out-of-plane deformation is again zero for all analysis steps (see figure 6.11b).

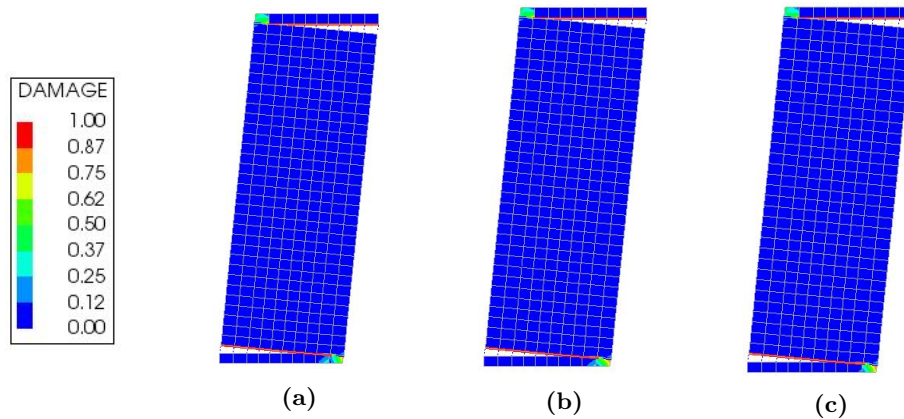


**Figure 6.12:** Damage at step 4844: (a) Layer 1 (b) Layer 2 (c) Layer 3

## 6.4 Conclusions

In this chapter the wall was modelled using the discrete crack approach. First, the model was exposed to the original load (applied in positive direction). The capacity curve of both NLFEA and SLA corresponded with the experimental curve. Second, the model was exposed to a load in opposite direction. Again SLA was able to obtain a capacity curve similar to the experimental one. However NLFEA didn't converge in an early state of the analysis. The application of shell elements in this model, resulted again in a reduction of deformation capacity, similar to the smeared crack model. However, the out-of-plane deformations were only little. The following conclusions can be drawn from this chapter:

### Numerical models versus experiment

- The parameters used, give accurate results with the respect to the peak load and ductility of the wall.
- Similar to the model in chapter 5, this model is able to simulate the crack pattern obtained in the experiment, until global failure of the wall occurred. Even though the vertical interfaces at the top and bottom of the wall are partly damaged, no full vertical crack is observed.

### NLFEA versus SLA

- SLA can cope with bifurcation problems (the occurrence of multiple cracks simultaneously). Whereas NLFEA didn't converge when horizontal as well as vertical cracks occurred, SLA was able to proceed with the analyses.

### Plane stress elements versus shell elements

- The use of shell elements reduces the deformation capacity as the maximum displacement decreased by 70% when the plane stress elements were replaced by shell elements.

### Discrete crack approach versus smeared crack approach

- Modelling the wall using the discrete crack approach is an effective way to prevent shear locking problems in a shear wall, due to the use of interface elements that separate the continuum elements.
- With the parameters used, the numerical model with plane stress elements predicted the deformation capacity more precisely compared to the smeared crack approach with plane stress elements from previous chapter.
- The out-of-plane deformations are reduced from a maximum of 5.0 mm for the smeared crack approach with shell elements till a maximum of 0.06 mm for the discrete crack approach. However, even though the out-of-plane deformations are significantly reduced, the maximum horizontal displacement is still not close to the horizontal displacement, obtained using plane stress elements. It can be concluded that the reduction of horizontal displacement at the top of the wall is not proportional to the out-of-plane deformations.



# 7. Out-of-plane wall: smeared crack approach

In chapter 3, the experimental results of the out-of-plane component are presented. This chapter will elaborate on numerical modelling of the wall, using the smeared crack approach, whereas in chapter 8 the discrete crack approach will be applied. The structure of this chapter is as follows. Section 1 addresses the numerical model briefly, because it has similarities with the in-plane shear wall in chapter 5. As the component described in this chapter is loaded out-of-plane, using plane stress elements is not possible, because plane stress elements assume a Cauchy stress state and they don't allow out-of-plane deformations. Therefore, section 2 will present results of the model with shell elements only. The chapter ends with a short conclusion.

## 7.1 Finite element model

### 7.1.1 FEM model and material properties

The numerical model of the *TUD\_COMP* – 28 experiment is illustrated in figure 7.2. The wall has a width of 1.448 m, a height of 2.725 m, a thickness of 0.12 m and it is pre-loaded with an overburden load of 0.25 MPa. The material properties used in this model are listed in table 7.1. The table shows that a shear retention factor of 0.01 is applied. In previous chapters shear locking problems occurred for models with a smeared crack approach in case of NLFEA. To overcome this problem a shear retention factor of  $10^{-6}$  was applied. However, as this is an out-of-plane load case, the in-plane principal direction will not rotate due to the out-of-plane load. Hence, shear locking is not expected during the NLFEA analysis. Besides that, a 5-point Simpson integration scheme is used in thickness direction.

The material properties lead to the sawtooth laws in figure 7.1, where again three stages are highlighted for both compression and tension. The linear elastic stages are coloured in light blue and green for compression and tension respectively, the crushing and cracking state are coloured in dark blue and yellow respectively and the fully crushed and fully cracked state are coloured in pink and red respectively. These colours will be used later on in the strain-plots of the wall as well, to see how the material at certain locations of the wall is damaged.

**Table 7.1:** Properties masonry for smeared crack concept

	<b>Masonry (composite)</b>		
Elasticity	$\rho = 1824 \text{ kg/m}^3$	$E_0 = 8800 \text{ MPa}$	$\nu = 0.21$
Tensile failure	$f_t = 0.4 \text{ MPa}$	$G_{ft} = 50 \text{ J/m}^2$	
Compressive failure	$f_c = 10 \text{ MPa}$	$G_{fc} = 20000 \text{ J/m}^2$	
Sawtooth parameters	$\beta = 0.01$	$p_{fac} = 0.1$	
Crack model	Fixed crack model		

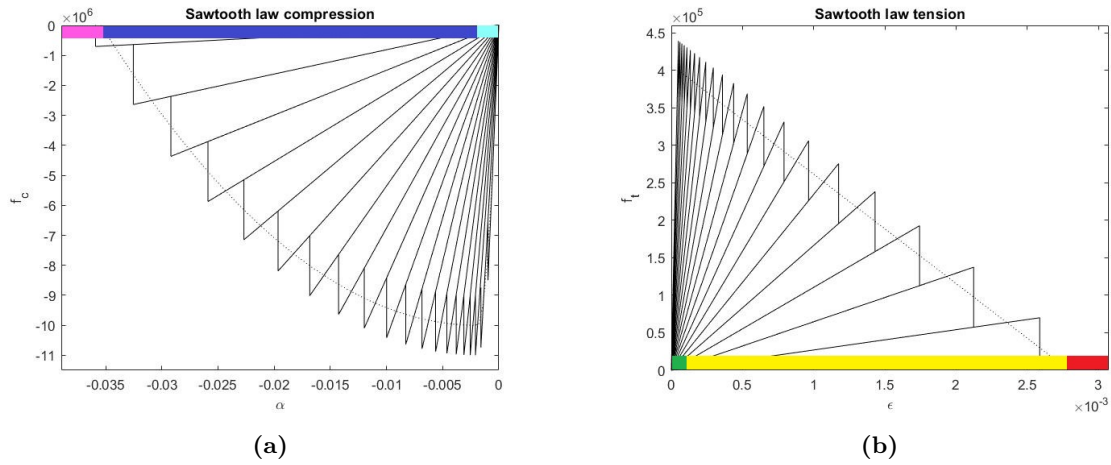


**Figure 7.1:** Sawtooth laws (a) Compressive curve (b) Tensile curve.

During the experiment, the intention was to apply clamped-clamped boundary conditions, but the test set-up wasn't sufficient to actually realise these boundary conditions as the top was able to rotate in the out-of-plane direction. For that reason, a hinged boundary condition is applied at the top in the numerical model. Figure 7.3 shows that the boundary conditions at least have influence on the initial stiffness of the wall. Using the basic structural mechanics formulas, the Young's modulus, moment of inertia and the height of the wall, the initial stiffness can be calculated. It becomes clear that using a hinged boundary condition results in a stiffness which is twice as less compared to the clamped-clamped configuration. In the experiment an initial stiffness of 12.3 kN/mm was found, which gives confidence to apply hinged-clamped boundary conditions.

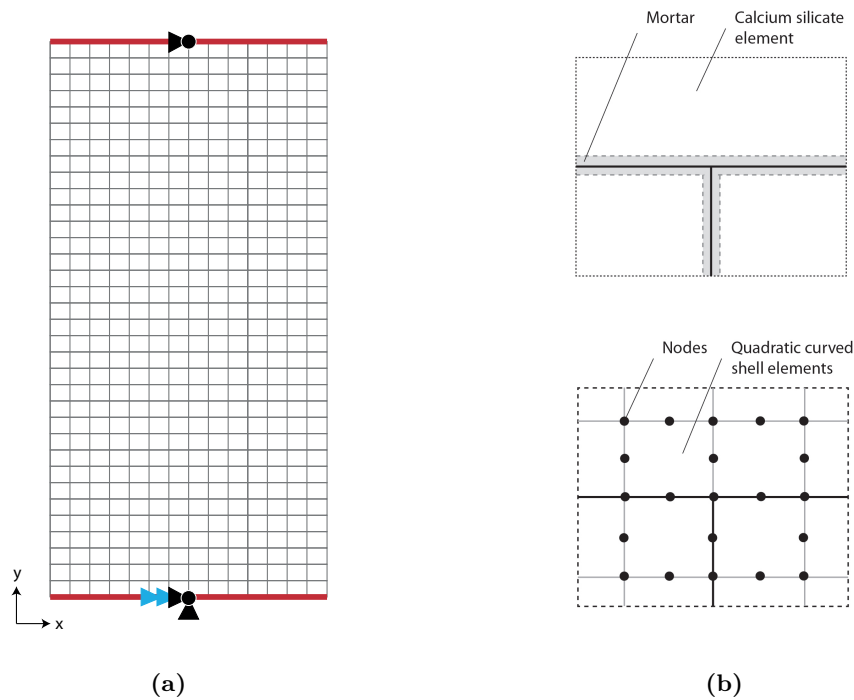


**Figure 7.2:** (a) Numerical model with the smeared crack approach (b) Top: detail of the actual wall. Bottom: detail of the numerical model.

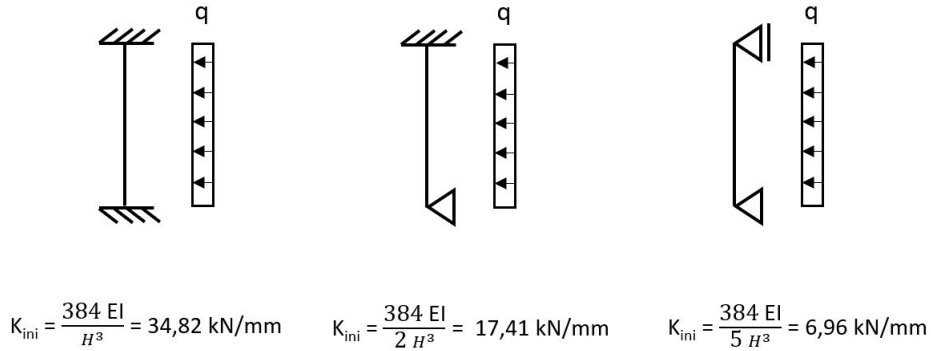


**Figure 7.3:** Influence of the boundary conditions on the initial stiffness of the wall.

### 7.1.2 Loading of the wall

In the experiment the load is applied in a displacement-controlled manner, by controlling the out-of-plane displacement at mid-height of the wall. In the numerical models, the load will be applied in a force-controlled manner, because of the following reasons:

- SLA has no concept of a "displacement-controlled" way loading. The external load will be applied in the form of a force, which will be scaled in every step of the analysis. It depends on the damage status of the whole wall, what the magnitude of the force will be.
- Running a displacement-controlled NLFEA, means that a prescribed deformation has to be applied. Applying a prescribed deformation distributed over the whole height will be an incorrect way of modelling the out-of-plane wall, because in that way the wall is forced in a certain shape already, instead of letting the boundary conditions determine how the final shape of the wall will be. Another option would be to run a NLFEA with a displacement-controlled load at mid-height of the wall. However, this will be incorrect too, because it will result in a completely different initial stiffness of the wall (see figure 7.4). Thus, even though with a displacement-controlled load it is easier to trace the post-peak behaviour of the wall, a force-controlled load will be applied using arc-length control.

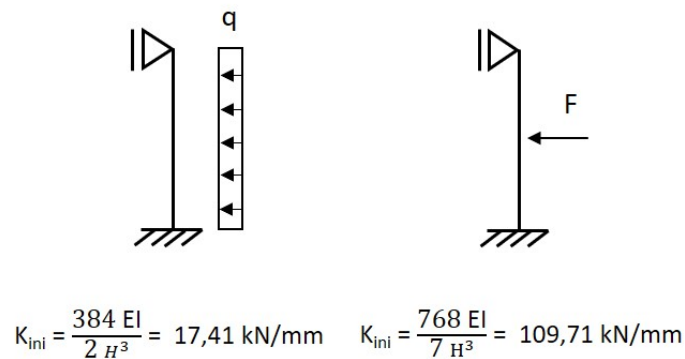


**Figure 7.4:** Influence of the type of force on the initial stiffness of the wall.

### 7.1.3 Stop criteria SLA

The stop criteria assumed for this model are as follows:

A step of an analysis is the last one as soon as:

1. The number of damage increments exceeds the number of sawteeth for any integration point in the model. This means either:
  - (a) 21 x tension + 21 x tension = 42 damage increments in tension, or
  - (b) 21 x tension + 22 x compression, or
  - (c) 22 x compression + 22 x compression = 44 damage increments in compression
2. A step of an analysis is the last one as soon as  $\lambda_{ini}$  is not able to return back to 1.0.
3. The displacement gets bigger than 120 mm (based on the analytical calculations in section 4.2)

## 7.2 Shell elements

As plane stress elements don't allow out-of-plane behaviour, this wall can only be modelled with shell elements. The force-displacement graph is plotted in figure 7.5a, together with the analytical expectation and the experimental results. It's important to note that, in contrary to the previous chapters, the NLFEA analyses for the out-of-plane wall are allowed to continue, even though the tolerance criteria weren't met, because this model had many difficulties converging. It's also important to mention that the out-of-plane model is very sensitive with respect to the material characteristics. It is not the aim of this thesis to reproduce the experimental graph as perfect as possible, because there are numerous modelling options that influence the results, think of the type of the iteration scheme, mesh size, material properties, tolerance, load control, integration scheme and number of integration points in thickness direction.

The numerical curve doesn't correspond with both the experimental and analytical results and therefore we took a closer look to be able to understand the reasons for this. Figure 7.5b zooms-in on the left part of the FU-graph. Besides, the moments of cracking are highlighted in this figure as well. The aim in the experiment was to have clamped-clamped boundary conditions (see figure 7.6b). The bending moments at the top and bottom are the highest, therefore cracks are expected to occur at these locations first. However, as the test set-up was not able to fully constrain the out-of-plane

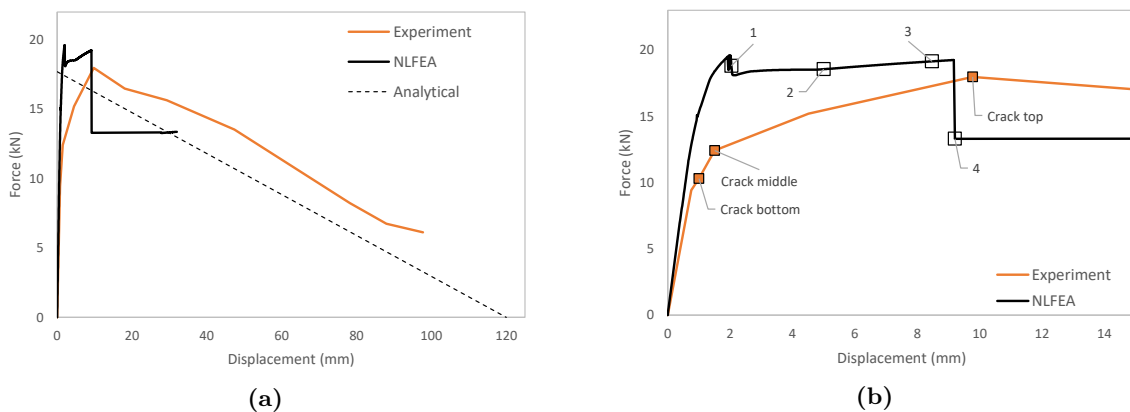


**Figure 7.5:** (a) Complete force displacement graph (b) Zoom-in close to the peak load

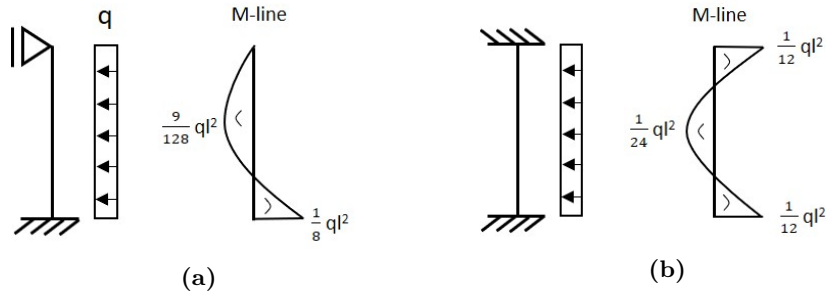


**Figure 7.6:** Bending moment diagrams (a) Numerical model, with clamped-hinged boundary conditions (b) Experiment, with the intended clamped-clamped boundary conditions.

rotation at the top, the bending moment at the top is less. Therefore, cracks are formed in the bottom first, followed by cracks in the middle of the wall and finally cracks in the top occur. It can be observed that, even though the initial stiffness of both the numerical model and the experiment are equal, cracks occur at an earlier stage in the experiment and the slope of the curve becomes less steep after cracking. A possible explanation is that in the experiment, mortar got crushed, which resulted in this reduction in stiffness.

Also the moments when the first cracks appeared and when hinges were formed in the model are indicated and numbered from 1 till 4. The top of the wall is modelled as a hinge and therefore the bending-moment-diagram will look like the one in figure 7.6a. The bending moment in the bottom is the highest, thus the first crack appeared in the bottom and this indicated with number 1. Number 2 indicates the moment that four out of five layers in the bottom are fully cracked and a hinge is formed. This moment is also illustrated in figure 7.7a, where the principal strains are plotted. The colours correspond with figure 7.1 where red indicates the fully cracked elements. A crack in the bottom can be observed. At moment 3 also elements in the middle of the wall start to crack, where after a sudden drop in the FU-graph is observed (moment 4). A hinge in the middle is formed, which results in a release of crack energy. During this drop the wall turns into a mechanism (see figure 7.7b), the bottom and top half of the wall relax and the out-of-plane rotation is fully localized in the hinges. After this moment, the rocking-mechanism is "activated" and the FU-curve should follow the dashed line. However, as geometrical non-linearity is not possible in combination with SLA yet, the curve will not follow the dashed line, but will stay horizontal. The analysis is only able to simulate the experimental curve up to the moment where the wall turns into a mechanism.

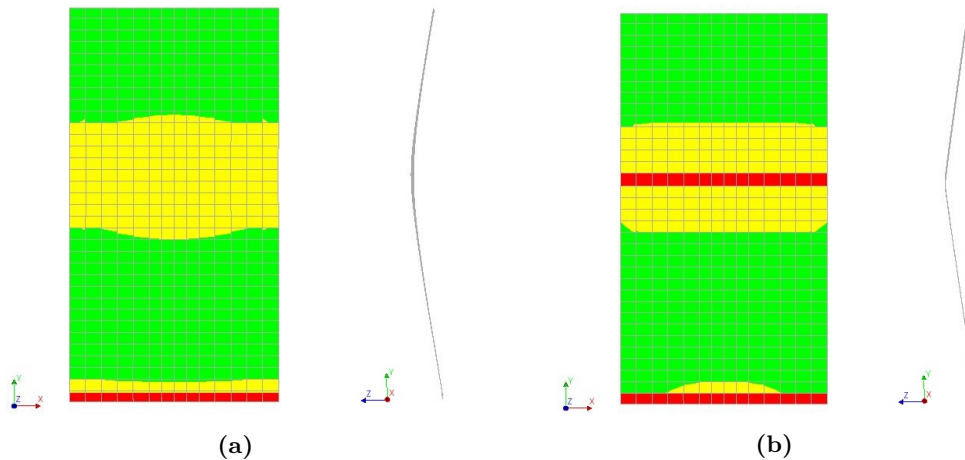


**Figure 7.7:** First principal strain ( $\epsilon_1$ ) (a) at moment 2, where a hinge in the bottom is formed (b) at moment 4, where a hinge in the middle is formed.

Figure 7.8a shows again the force-displacement graph, but this time all the steps are marked where the analysis wasn't able to converge within the predefined number of iterations. Figure 7.8 shows the relative out-of-balance forces of these steps and two peaks are highlighted. The two peaks correspond with moment 1 and moment 4. Apparently the numerical model has difficulties to find equilibrium between the internal and external forces when the first cracks are formed (moment 1) and when the wall has turned into a mechanism (moment 4).

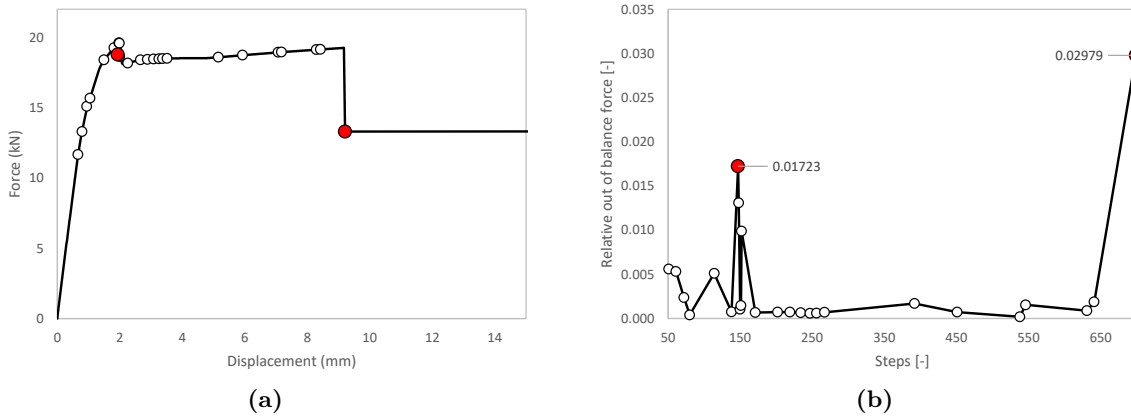


**Figure 7.8:** (a) Force displacement graph, where moment 1 and moment 4 are highlighted (b) Relative out-of-balance forces, where moment 1 and moment 4 are highlighted.

The results of SLA are plotted together with the results of NLFEA in the pictures below. One difference is the calculation time. In case of SLA, the maximum calculation time is proportional to the number of elements times the number of integration points per element times the number of sawteeth. In case of NLFEA, the maximum calculation time is proportional to the number of load steps times the number of iterations per load step. With respect to this model, the SLA analysis took about three times longer, however with SLA, we saved time in the preparation stage as we didn't need to search for the correct iteration scheme, load-control, convergence criteria and number of load steps.

Another difference between NLFEA and SLA is related to the moment at which a mechanism is formed. The SLA-curve follows the NLFEA very well until the wall turns into a mechanism. Whereas a sudden drop is observed in case of NLFEA, a snap-back is visible for SLA. Both analyses end with a horizontal plateau as for both analyses geometrical non-linearity is not activated. For SLA this horizontal part of the curve continues up to a displacement of 579 mm. However, at that point, two

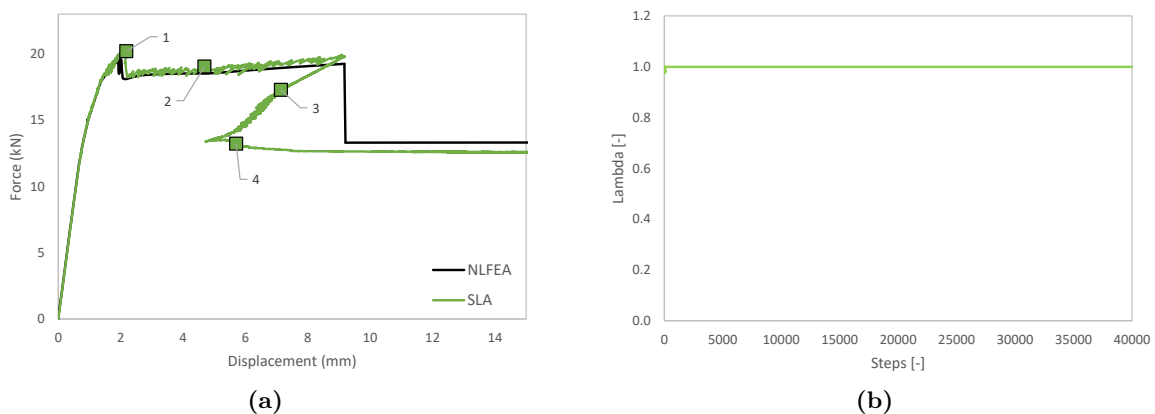


**Figure 7.9:** (a) Force displacement graph (b) Initial load multiplier ( $\lambda_{ini}$ ).

stop criteria are met already. The first stop criterion (exceedance of number of sawteeth) is met at step 38207 and the third one (displacement bigger than 120 mm) is met between step 37101 and step 37201. As criterion 3 is met first, this one is governing and the analysis is stopped when a displacement of 120 mm is reached.

## 7.3 Conclusions

The following conclusions can be drawn from this chapter:

### Numerical models versus experiment

- Geometrical non-linearity is not a possible feature in SLA yet and the slowly decreasing base shear force, caused by the rocking motion as soon as a mechanism is formed, is therefore not possible to reproduce. If one is interested in the post-peak behaviour, this should be included and the lack of this feature is a disadvantage of SLA for now. For the shear wall, the rocking motion couldn't be simulated as well, however as the decrease of base shear force capacity is more severe for the transversal wall, the limitation of not including geometrical non-linearity is most pronounced for the transversal wall.
- The numerical models are able to simulate the crack pattern in the experiment. Even though the use of the smeared crack approach leads to a diffuse crack pattern, the locations of the hinges are correct. Also the order of the hinge formation is correct, however, the moments when these hinges occur, differ from the experiment.

### NLFEA versus SLA

- The advantage of using an inherently stable numerical analysis becomes clear while modelling the out-of-plane wall as NLFEA had many difficulties converging, whereas SLA overcomes this problem.
- In case of NLFEA, a well considered decision has to be made between the force-controlled or displacement-controlled way of loading, in order to find a stable solution. In case of SLA this decision is not required, which makes that method easier in use.



# 8. Out-of-plane wall: discrete crack approach

Whereas previous chapter discussed the out-of-plane wall using a smeared crack approach, this chapter will elaborate on the discrete crack approach. In the first section the model is briefly explained. In section 2 shell elements are used in combination with interface elements. Also in this chapter the use of plane stress elements is not possible. Even though interface elements are used, which could allow for out-of-plane rotation, still plane stress elements are not possible as they assume a Cauchy stress state, meaning that the out-of-plane stress should be zero.

## 8.1 Finite element model

### 8.1.1 FEM model and material properties

The numerical model is depicted in figure 8.1. A distinction is made between the mortar and the bricks and the material properties are listed in table 8.2 and 8.1.

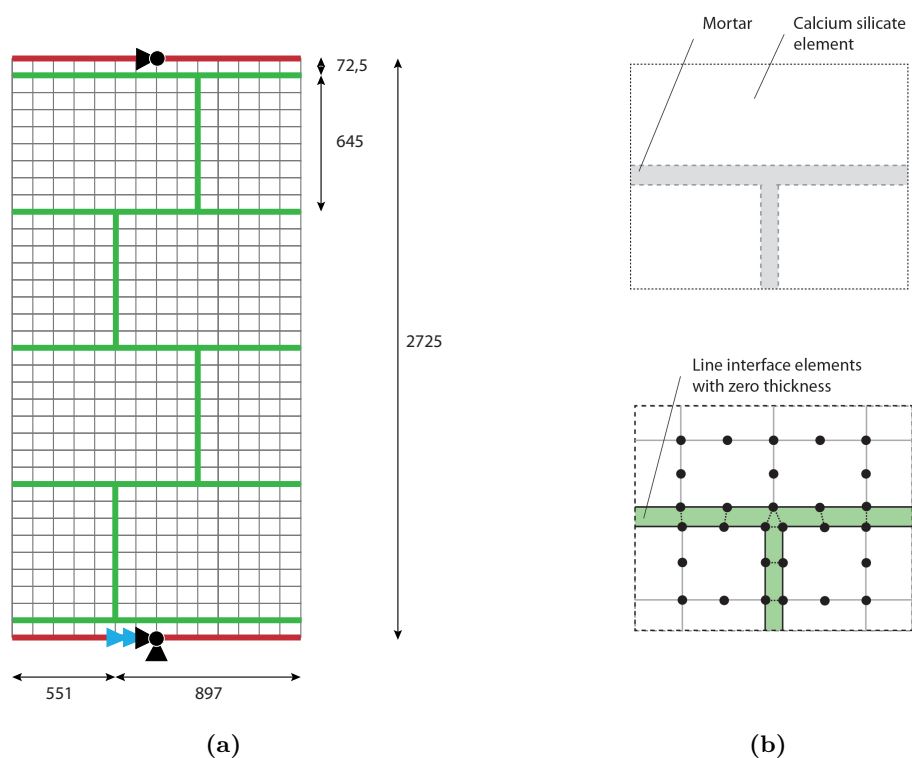


**Figure 8.1:** (a) Model with meso-modelling approach (b) Top: detail of wall. Bottom: detail of the numerical model.

As stated before, the Coulomb Friction model is not available for SLA yet. Shear failure is incorporated by a constant shear retention factor of 1% ( $\beta = 0.01$ ) and like the numerical model in chapter 6, this model is also a combination of the discrete crack and smeared crack approach. As the current SLA code only contains tensile failure for the interface elements, the continuum elements should account for compressive failure. Furthermore, a 5-point Simpson integration scheme is used for both interface elements and continuum elements.

**Table 8.1:** Properties CaSi-bricks for meso-modelling approach

	CaSi-bricks (unit)		
Elasticity	$\rho = 1824 \text{ kg/m}^3$	$E_0 = 8800 \text{ MPa}$	$\nu = 0.21$
Tensile failure	$f_t = 4.0 \text{ MPa}$	$G_{ft} = 4000 \text{ J/m}^2$	
Compressive failure	$f_c = 10 \text{ MPa}$	$G_{fc} = 20000 \text{ J/m}^2$	
Sawtooth parameters	$\beta = 0.01$	$p_{fac} = 0.1$	

**Table 8.2:** Properties interface elements for meso-modelling approach

	Mortar (interface element)	
Elasticity	$k_n = 867 \text{ N/mm}^3$	$k_t = 361 \text{ N/mm}^3$
Tensile failure	$f_t = 0.2 \text{ MPa}$	$\varepsilon_{ult} = 0.00010692$
Compressive failure	Linear elastic	
Sawtooth parameters	$\beta = 0.01$	$p_{fac} = 0.1$

### 8.1.2 Stop criteria SLA

Using the material properties listed on the previous page, the number of sawtooth for compression and tension are defined, leading to the stop criteria below.

A step of an analysis is the last one as soon as:

1. The number of damage increments exceeds the number of sawteeth for any integration point in the model. For the interface elements this means an exceedance of 35 damage increments in tension. For the continuum elements this means either:
  - (a) 20 x tension + 20 x tension = 40 damage increments in tension, or
  - (b) 20 x tension + 22 x compression, or
  - (c) 22 x compression + 22 x compression = 44 damage increments in compression
2. A step of an analysis is the last one as soon as  $\lambda_{ini}$  is not able to return back to 1.0.
3. The displacement gets bigger than 120 mm.

## 8.2 Shell elements

Comparing the numerical results with the analytical and experimental results, it can be observed that, similar to the model in chapter 7, also this model is not as ductile as the experiment and that the geometrical non-linearity, caused by the rocking motion, is not taken into account.

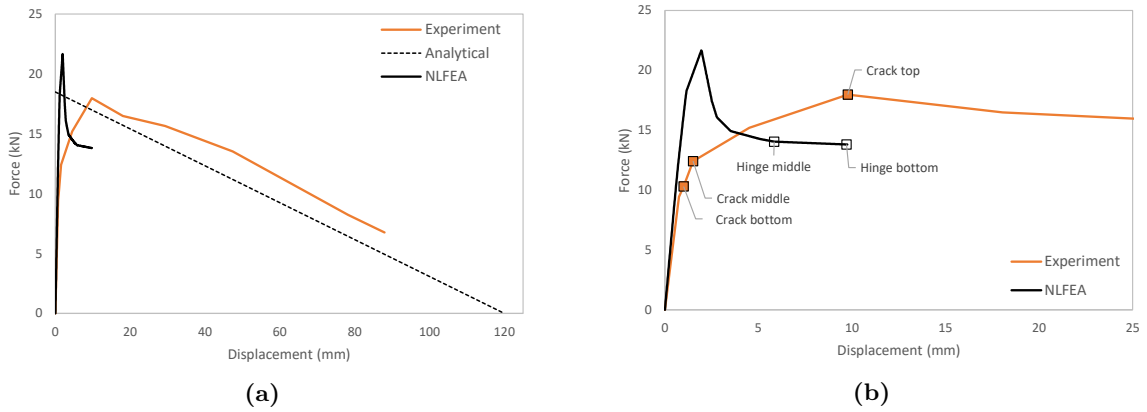


**Figure 8.2:** (a) Complete force displacement graph (b) Zoom-in close to the peak load.

When we take a closer look at the curve (figure 8.2b), the different moments of cracking can be distinguished. In the previous chapter, where the wall was modelled with a smeared crack approach, the order in which the hinges were formed was as expected: first a bottom hinge is formed as the bending moment is highest at that location, followed by a hinge in the middle. In the model here, the order is the other way around. First a hinge in the middle is formed, where after a hinge in the bottom is observed. The reason can be found in figure 8.3a. In the model using the smeared crack approach the strains due to bending were spread over the whole height of the wall. However, in this model, the strains are lumped in the interface elements as that are the weakest points in the model. The figure shows that the strains in the middle are the highest, therefore a crack is formed at that location first.

A second difference with the smeared crack model is that the capacity curve has a clear peak. In this model the damage is lumped in the interface elements and the crack energy is released from these

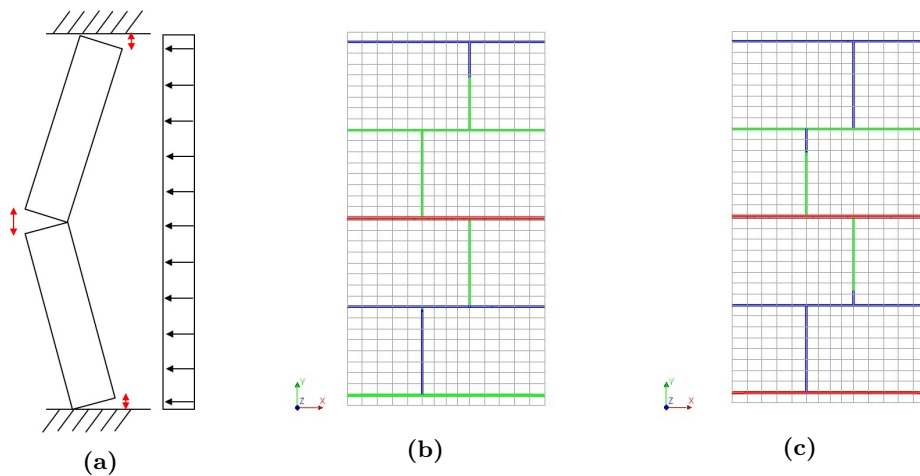


**Figure 8.3:** (a) Crack openings (b) Interface traction, when a hinge in the middle is formed (c) Interface tractions when a hinge at the bottom is formed.

elements only. In the smeared crack model the damage was spread over the whole height of the wall. All these small cracks contribute to the total crack energy release and the area under the capacity curve is therefore bigger than the area under the capacity curve in figure 8.2b.

The last main difference between the discrete crack model and the smeared crack model regarding NLFEA, is the fact that the discrete crack model had no difficulties converging. The model was able to find equilibrium between the external and internal forces within the predefined maximum number of iterations. Only when the wall turned into a mechanism, the model couldn't converge and highly unrealistic displacements were found.

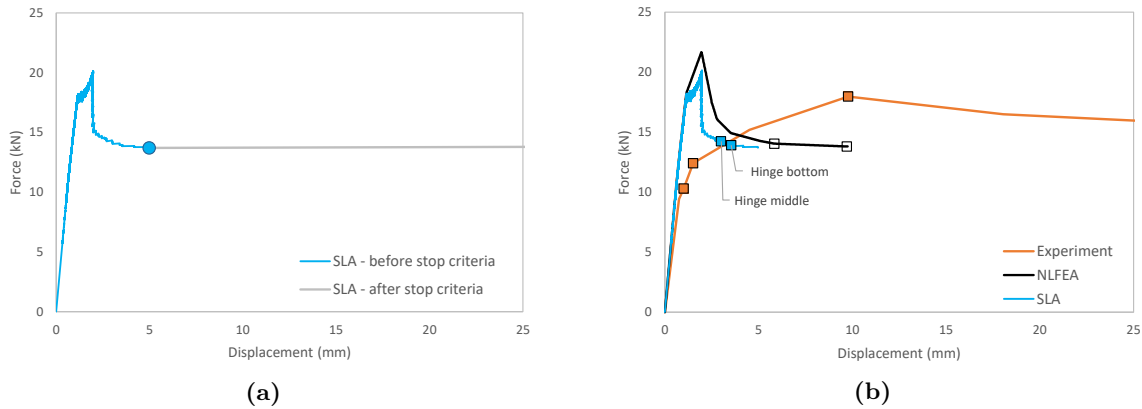


**Figure 8.4:** (a) Force displacement graph of SLA, with the stop criterion marked (b) Force displacement graph of both NLFEA and SLA

Figure 8.4 shows the results of the model using SLA. To decide on the last step, again the results are analysed based on the three stop criteria. Stop criterion 1 (exceedance of number of sawteeth) is met in step 12918. The analysis wants to run infinitely, because one integration point in one of the interface elements is taken as the critical one and gets a damage increment infinite times. Step 12918 is the step before  $n_t$  is exceeded. Stop criterion 2 is not met, since lambda equals 1 throughout the whole analysis. It turns out that stop criterion 3 is the governing one, because in step 12914 the displacement jumps from 4.97 mm to 174.50 mm and thus the maximum displacement of 120 mm is exceeded.

The steps at which hinges are formed are marked in figure 8.4b. Also here the middle hinge is developed first and the bottom hinge second. Even though the shape of the curve is quite similar compared to the NLFEA, there are some differences. The peak load using SLA is 20.0 kN, compared to the peak load of 21.6 kN when a NLFEA is performed. Also the post peak behaviour is slightly different. The exact explanation will be difficult to find, but it is probably a result of the fundamental difference between SLA and NLFEA: applying damage increments versus load increments.

Also regarding SLA a difference is observed between the smeared crack approach and the discrete crack approach. The calculation time reduces by a factor of 3 when the wall is modelled with the discrete crack approach instead of the smeared crack approach. In case of the smeared crack model, the damage was scattered across the wall, but with the discrete crack model the damage is lumped in the interface elements, which means that less integration points will be damaged and this reduces the calculation time and therefore the costs.

## 8.3 Conclusions

The following conclusions can be drawn from this chapter:

### **Numerical models versus experiment**

- Similar to the model in chapter 7, this model is not able to exactly reproduce the capacity curve of the experiment due to the lack of geometrical non-linearity in the SLA code.
- This model is also able to simulate the crack pattern, even though the order in which the hinges are formed, differ. The reason for this is the use of interface elements, which are the weakest points in the model and the stress distribution will therefore become different, compared the the stress distribution in the smeared crack model.

### **Discrete crack approach versus smeared crack approach**

- In case of NLFEA, the discrete crack model is preferred, as this model didn't have convergence issues, whereas the smeared crack model did.
- Also in case of SLA the discrete crack model is preferred, because it reduces the calculation time. The damage is lumped in the interface elements, resulting in less damage increments.



## 9. Discussion and conclusions

The SLA method is still under development and in this report possibilities and limitations of the current SLA code were investigated, using two experimental benchmarks: one shear wall and one out-of-plane loaded wall, both pre-stressed. For these masonry components, two modelling approaches were applied: the smeared crack model, where the wall exist of one material only, and the discrete crack model, where a distinction is made between mortar and bricks. Within each approach two finite element types were used. The new implementation of the SLA code for shell elements is validated by modelling the shear wall with plane stress elements. The most important comparison, was the one between NLFEA and SLA in order to see how SLA can improve numerical predictions of the brittle behaviour of masonry components.

### Material law in tension

The test models in section 5.3.1. showed that the SLA code still contains certain flaws and the results were analysed in detail to isolate the problems. One of these shortcomings was the fact that a few analyses ran indefinitely. After analysing the damage history of these models, it is found that in case of tension, the SLA algorithm takes one integration point as the critical one for an infinite number of times. Even though no damage increment was applied any more, due to the exceedance of the number of sawteeth in tension, still this integration point was indicated as the critical one. This way no other integration points were allowed to get damaged and the whole failure process of the numerical models was hindered. In this thesis stop criteria are defined to temporarily deal with the shortcomings, until the errors will be found and solved in future work. The first stop criterion stated that the analysis should stop as soon as the number of damage increments exceeds the number of sawteeth.

It can be concluded that this stop criterion was effective as this was the governing criterion in several models, meaning that if the stop criterion wasn't used, these analyses would run indefinitely, without continuation of the failure process. Now the number of analysis steps could be reduced to the number of "effective" damage increments and unnecessary calculation time is prevented.

### Shear retention factor and shear locking

In this thesis a constant shear retention factor is applied. The results showed an over-stiff response in case of a NLFEA and the analysis terminated quickly. After evaluating the results of the NLFEA, it is found that the constant shear retention factor caused extra shear stresses at the bottom of the wall. The summation of all these shear stresses is equal to the reaction force, which should be equal to the applied external force to ensure equilibrium of forces. SLA, however, was able to trace the equilibrium path of the wall without this 'shear locking' problem. The reason for this is that the last branch in the sawtooth law has a shear retention factor of approximately zero, whereby no shear stresses remain after completely cracking of the material. In case of NLFEA, using a rotating crack approach did solve the problem. This resulted in a capacity curve similar to the one of SLA.

It can be concluded that the prevention of shear locking in a shear wall is an important advantage of SLA. This way, the capacity of the shear wall will not be overestimated. The numerical model can predict the peak load accurately, which is important when, in future research, no experimental results are available to validate numerical models.

### Non-proportional loading

The algorithm for non-proportional loading is more complex than the algorithm for proportional loading, as a distinction has to be made between the loads, where the variable load has to be scaled according to the SLA procedure. In this thesis the non-proportional loading case is used as well as a similar well known NLFEA procedure (the phases analysis) to verify the non-proportional loading algorithm. The results showed that the SLA algorithm works in a sense that the peak load corresponds with the peak load of the non-linear phased analyses. However, in a few shear wall models, a negative displacements is observed, even though the load was applied in positive direction and this is physically not possible. The moment this happened, the initial load multiplier dropped from 1 to approximately zero and therefore a second stop criterion is defined to deal with this problem. This criterion stated that the analysis should stop as soon as the initial load multiplier wouldn't be able to return back to 1.

Regarding these results, we can conclude that modelling a structure, which is pre-stressed, is possible with the non-proportional algorithm. Nonetheless, an imperfection is found: the algorithm could cause spurious results for the shear wall with respect to the capacity curve, because displacements in the wrong direction are found. The use of the second stop criteria was effective to temporarily overcome this problem as no negative displacements were observed after applying the stop criterion.

### Damage strategy and bifurcation

The fundamental difference between NLFEA and SLA became clear when the shear wall was modelled with shell elements. The SLA algorithm can only pick one critical integration point per analysis step and reduces the stiffness of one integration point at the time. The outcome was an asymmetric wall with respect to the thickness and out-of-plane deformations were observed even though the wall was loaded in-plane. This led to a reduction of the ductility of at least 50 %. For the discrete crack model with shell element the reduction of the deformation capacity was similar, however the out-of-plane deformation was less severe.

Furthermore the calculation time drastically increased (and therefore also the calculation costs), when shell elements were used for the in-plane loaded shear wall, as shell elements have more integration points in thickness direction than plane stress elements. Each analysis step takes more time, since the algorithm has to calculate the load multiplier for more integration points, and the total required analysis steps increased, since more integration points get damaged. In total the calculation time increased up to 19 times for both the discrete crack model and the smeared crack model, when the number of integration points in thickness direction was increased from 1 (for plane stress elements) to 3 (for shell elements). For the NLFEA no difference was observed between the use of shell elements or plane stress elements.

Also between different crack approaches the difference in calculation time was observed using SLA, especially for the out-of-plane loaded transversal wall. When this wall was modelled with the smeared crack approach, the damage was scattered across the whole wall, but with the discrete crack approach, the damage was lumped in the interface elements. This reduced the calculation time (and therefore the calculation costs) by a factor of three.

The influence of initial value of Poisson's ratio on the shear wall was investigated in this research as well, because it was expected that it would influence the directions of the principal stresses at the bottom of the wall. As cracks occurred at this location, it would influence the capacity of the wall. The results showed that the initial value of Poisson's ratio only influences the ductility of the wall, not the peak load. However, in the SLA code it is found that SLA and NLFEA apply a different damage strategy for Poisson's ratio. For a NLFEA one can choose between a damage-based Poisson's ratio or a constant Poisson's ratio. In the current code for SLA, Poisson's ratio drops to zero as soon as the integration point is critical for the first time. As these damage strategies differ, a comparison between NLFEA and SLA is invalid. Therefore also analyses were conducted with a zero Poisson's ratio to elude this difference in damage strategy. The capacity curve showed the fundamental advantage of

SLA, namely that this analysis is numerically stable, whereas NLFEA didn't converge in an early stage of the analysis. The peak loads of both analyses were equal.

From all these results we can conclude that Poisson's ratio doesn't influence the peak load, only the deformation capacity. However, a damage-based Poisson's ratio should be implemented in the SLA code in order to compare the influence of a non-zero Poisson's ratio on the capacity of the wall correctly. Moreover, the research showed that the type of finite element being used doesn't make a difference, when a regular non-linear analysis is conducted. For SLA the use of shell elements in the shear wall model did influence the results. The deformation capacity of the shear wall cannot be predicted with shell elements accurately yet and the actual wall in the experiment was able to deform at least twice as much compared to the numerical model. Besides, unexpected out-of-plane deformations of the shear wall can occur in the shear wall, modelled according to the smeared crack approach with 3 integration points in thickness direction. This latter observation could make future analyses of a complete building more complex, because the algorithm causes unexpected out-of-plane deformations, which could be misleading in the interpretation phase. Nonetheless, performing a SLA is a solution to overcome bifurcations (which is a problem for regular non-linear analyses), as the method is always able to pick a critical integration point.

### Lack of geometrical non-linearity

For both masonry components a rocking curve is derived analytically. It showed that the wall can bear less load as soon as the deformation increases. However, it is not possible to simulate this with SLA, as geometrical non-linearity is not included in the code yet. For the transversal wall, the decrease of base shear force is more severe, therefore the limitation (lack of geometrical non-linearity) is most pronounced for the out-of-plane loaded transversal wall and the post-peak behaviour cannot be simulated correctly. Then, the numerical model will give an overestimation of the force capacity, as the base shear force actually decreases as soon as the peak load is reached.

The rocking curve also provided a maximum displacement that the walls can reach. This is used in the third stop criterion, which stated that the analyses should stop as soon as that displacement is reached. For the shear wall however, this stop criterion was never governing. Besides, the maximum displacement was related to shear force equal to 0 kN. As it is not possible to simulate this degradation, it can be concluded that the third stop criterion was redundant.

### Answering the research question

With these conclusions the main research question can be answered. The question was:

*To what extent is the Sequentially Linear Analysis method able to predict the behaviour of the two unreinforced masonry components of the TUD-2 Building, namely the shear wall and the out-of-plane wall, during a monotonic pushover test?*

This question can be answered as follows:

*SLA is able to predict the behaviour of the masonry components non-proportionally except for the post-peak behaviour of the transversal wall and it outperforms NLFEA in the sense that it is inherently stable and no over-stiff response is observed, while modelling the shear wall with a constant shear retention factor. In addition, there are less modelling options, which, we think, makes SLA easier in use and 'bifurcation' is never a problem, as the algorithm is always able to pick a critical integration point. However, it also has limitations: the use of shell elements leads to a decrease in deformation capacity and unintended out-of-plane deformations are observed for the shear wall even though the wall is only loaded in-plane. Furthermore, a flaw in the current code could result in an analysis that runs indefinitely. Stop criterion, defined in this thesis, can be used to temporarily deal with these problems. Lastly, geometrical non-linearity cannot be included in the models yet. This latter limitation is most pronounced while modelling the out-of-plane wall.*



# 10. Recommendations

In this chapter we will reflect upon the findings and recommendations are provided for future research.

- In this thesis current problems of the SLA code are identified and stop criteria were defined to deal with the problems temporarily. Nonetheless, the exact cause of the problems should still be found and solved
- The results in chapter 5 showed that shear locking doesn't occur in case of SLA, due to the last branch of the sawtooth law, which has a zero stiffness. It is recommended to implement a similar drop of the stiffness in regular NLFEA as soon as an integration point is completely damaged. It is expected that this will help the NLFEA to overcome the shear locking problem.
- Also some recommendations are provided which are related to a future extension of SLA. First, a damaged based Poisson's ratio should be implemented. While modelling the out-of-plane wall, the influence of difference damage strategies between NLFEA and SLA is ignored, as it is assumed that it will only slightly influence the results. However, to confirm this statement an extra validation is recommended as soon as the damaged-based Poisson's ratio is available in the SLA code. Second, it is recommended to investigate the possibility of allowing multiple integration points to be critical at the same time. This will speed up the analysis, which is desired especially when the number of elements and integration points increase.
- This report provided an overview of opportunities and limitations of the SLA method, while modelling the two main components of the TUD-2 building. The next step would be to model the complete structure. It is advised to use the discrete crack approach in case of SLA. The main damage will be lumped in the interface elements, which reduces the calculation time. Besides, no severe out-of-plane deformation are expected for the components loaded in-plane.

If the decrease in base shear force capacity of the complete building is quite severe, the post-peak behaviour cannot be predicted. As soon as geometrical non-linearity is included in the SLA algorithm, only then the complete behaviour can be simulated.

Also attention should be paid when shell elements are applied in combination with SLA. It causes a decrease in deformation capacity and out-of-plane deformation can occur which might be misleading in the interpretation stage, as it will not be clear whether the deformations are part of the structures behaviour or if the deformations are a result of the SLA damage procedure.

- The behaviour of the transversal wall is very sensitive with respect to the material properties. In this thesis no parameter study is conducted for the out-of-plane wall, as it was not the objective to find the exact parameters. Still it is recommended to perform such a variation study to improve the results.



# Bibliography

- Angelillo, M. (2014). *Mechanics of Masonry Structures*, volume 551 of *CISM International Centre for Mechanical Sciences*. Vienna: Springer.
- Bruneau, M. (1994). State-of-the-art report on seismic performance of unreinforced masonry buildings. *Journal of Structural Engineering*, 120(1):230–251.
- Damiola, M., Esposito, R., and Ravenshorst, G. (2017). Quasi-static cyclic out-of-plane tests on masonry components 2016/2017. Delft University of Technology. Report number C31B67WP3-5, version 1, 05 December 2017.
- DeJong, M. J., Belletti, B., Hendriks, M. A. N., and Rots, J. G. (2009). Shell elements for sequentially linear analysis: lateral failure of masonry structures. *Engineering Structures*, 31(7):1382–1392.
- DeJong, M. J., Hendriks, M. A. N., and Rots, J. G. (2008). Sequentially linear analysis of fracture under non-proportional loading. *Engineering Fracture Mechanics*, 75(18):5042–5056.
- DIANA FEA BV (2010). DIANA User’s Manual, release 10.2. Delft.
- ElGawady, M. A., Lestuzzi, P., and Badoux, M. (2007). Static cyclic response of masonry walls retrofitted with fiber-reinforced polymers. *Journal of Composites for Construction*, 11(1):50–61.
- Eliáš, J. (2015). Generalization of load–unload and force-release sequentially linear methods. *International Journal of Damage Mechanics*, 24(2):279–293.
- Eliáš, J., Frantík, P., and Vořechovský, M. (2010). Improved sequentially linear solution procedure. *Engineering fracture mechanics*, 77(12):2263–2276.
- Esposito, R. and Ravenshorst, G. J. P. (2017). Quasi-static cyclic in-plane tests on masonry components 2016/2017. Delft University of Technology. Report number C31B67WP3-4, version 1, 10 August 2017.
- Esposito, R., Ravenshorst, G. J. P., Schippers, R., and Rots, J. G. (2016). Cyclic pushover test on an calcium silicate element masonry structure [Powerpoint].
- Esposito, R., Terwel, K., Ravenshorst, G., Schipper, H., Messali, F., and Rots, J. (2017). Cyclic pushover test on an unreinforced masonry structure reseambling a typical dutch terraced house. In *16th World Conference on Earthquake, WCEE*, pages 9–13.
- Hendriks, M. A. N. (2015). CIE5148 Computational Modeling [Powerpoint].
- Kraus, J. (2014). Sequentially linear modelling of combined tension/compression failure in masonry structures. MSc thesis report, TU Delft.
- Lourenço, P. B. (1996). Computational strategies for masonry structures. Ph.D. thesis, Delft University of Technology, the Netherlands.
- Lourenço, P. B., Rots, J. G., and Blaauwendraad, J. (1995). Two approaches for the analysis of masonry structures: micro and macro-modeling. *HERON*, 40(4):313–340.

- Nederlands Normalisatie Instituut (2017). *Masonry NPR9998:2017*, The Netherlands.
- Ng'andu, B. M. (2006). Bracing steel frames with calcium silicate element walls Eindhoven: Technische Universiteit Eindhoven DOI: 10.6100/IR607328.
- Pari, M., Jafari, S., Messali, F., Esposito, R., and Rots, J. G. (2017). Computational modeling of the cyclic pushover test on a calcium silicate element masonry assemblage.
- Rots, J. G. (2001). Sequentially linear continuum model for concrete fracture. In R. de Borst, J. Mazars, G. Pijaudiet-Cabot and J.G.M. van Mier (eds.). *Fracture Mechanics of Concrete Structures*, 13:831–839. Lisse, The Netherlands: Balkema.
- Rots, J. G., Belletti, B., and Invernizzi, S. (2006). On the shape of saw-tooth softening curves for sequentially linear analysis. EURO-C 2006 Computational Modelling of Concrete Structures, 27-30 March, Mayrhofen, Tyrol, Austria, 431-442.
- Rots, J. G. and Blaauwendraad, J. (1989). Crack models for concrete: discrete or smeared? Fixed, multi-directional or rotating? *Heron*, 34(1):1–59.
- Rots, J. G. and Civieltechnisch Centrum Uitvoering Research en Regelgeving (Netherlands). (1997). *Structural Masonry: An Experimental/Numerical basis for practical design rules (CUR Report 171)*. Rotterdam: A.A.Balkema.
- Rots, J. G., Messali, F., Esposito, R., Jafari, S., and Mariani, V. (2016). Thematic keynote computational modelling of masonry with a view to groningen induced seismicity. In *Structural Analysis of Historical Constructions: Anamnesis, Diagnosis, Therapy, Controls: Proceedings of the 10th International Conference on Structural Analysis of Historical Constructions (SAHC, Leuven, Belgium, 13-15 September 2016)*, page 227. CRC Press.
- Schippers, R. (2017). Push-over test on full-scale house ready for start! [Image]. Retrieved from <https://www.linkedin.com/pulse/push-over-test-full-scale-house-ready-start-roel-schipper/>.
- Van Dam, J. (2015). Validation of efficient numerical model for out-of-plane bending of unreinforced masonry walls. MSc thesis report, TU Delft, the Netherlands.
- Van de Graaf, A. (2017). Sequentially linear analysis for simulating brittle failure. Ph.D. thesis, Delft University of Technology, the Netherlands.
- Wells, G. (2011). The finite element method: An introduction.

# Appendices

## A Shell elements fixed in out-of-plane direction

To check whether the out-of-plane behaviour of shell elements really does influence the results, a new model is built. This model is also composed of shell elements, but all elements are fixed in z-direction, meaning that no out-of-plane behaviour can take place (see figure 1). Whereas the plane stress elements only have 1 integration point, the shell elements have 3 integration points in thickness direction.

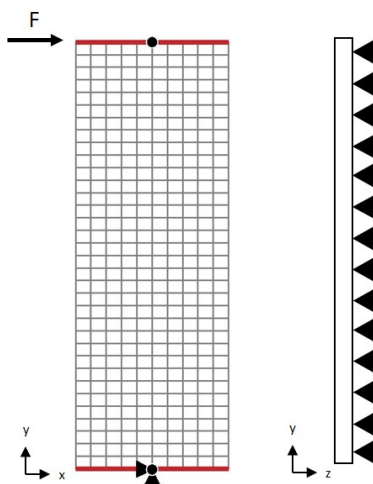
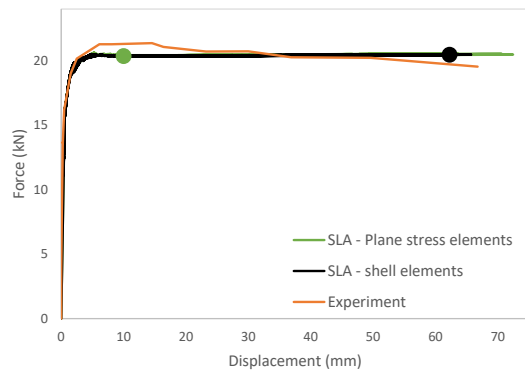


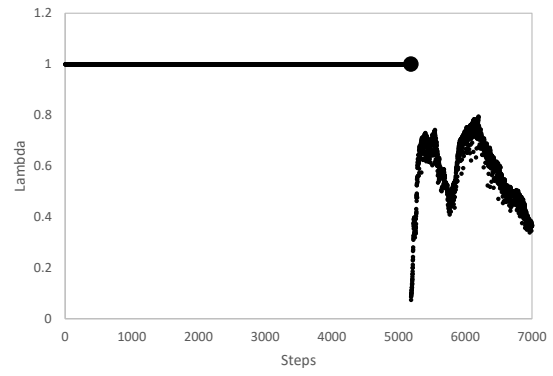
**Figure 1:** Smeared crack model, fixed in the z-direction

As the capacity curve in figure 2a shows, the difference between the analysis with plane stress elements and shell elements is almost negligible. For both analyses, the second stop criterion is governing: the last step is the one where  $\lambda_{ini}$  isn't able to return back to 1. The peak load is identical and also the maximum displacement is very similar, but the model with plane stress elements is still able to displace a little bit further. The small difference in the capacity curve is expected. After assigning a damage increment to an integration point, the algorithm has to pick a next critical integration point. It might be the case that an integration point somewhere else in the model is critical instead of an integration point at the same place but in another thickness layer. This could cause the small difference with respect to the ductility. A possible solution to this, and to the out-of-plane behaviour of shell elements in case of in-plane loading, might be to allow multiple integration points to be critical at the same time. In that case, all integration points in thickness direction will be critical at the same time and no out-of-plane behaviour is expected. To see whether this is a correct solution, further research needs to be done and the SLA algorithms need to be modified.

This model proves that the SLA implementation for shell elements works adequately and that the out-of-plane behaviour of the model with shell elements from section 5.4 causes the low ductility of the wall.



(a)



(b)

**Figure 2:** Results for shear wall with shell elements, fixed in out-of-plane direction (a) Force-displacement graph (b) Initial load multiplier  $\lambda_{ini}$



